

4-2014

## 3D Simulation of the Velodyne HDL-32E Lidar Integrated with an Autonomous Marine Vehicle

Alecia A. Hurst

*Embry-Riddle Aeronautical University - Daytona Beach*

Follow this and additional works at: <https://commons.erau.edu/edt>



Part of the [Mechanical Engineering Commons](#)

---

### Scholarly Commons Citation

Hurst, Alecia A., "3D Simulation of the Velodyne HDL-32E Lidar Integrated with an Autonomous Marine Vehicle" (2014). *Dissertations and Theses*. 161.

<https://commons.erau.edu/edt/161>

This Thesis - Open Access is brought to you for free and open access by Scholarly Commons. It has been accepted for inclusion in Dissertations and Theses by an authorized administrator of Scholarly Commons. For more information, please contact [commons@erau.edu](mailto:commons@erau.edu).

3D Simulation of the Velodyne HDL-32E Lidar Integrated with an Autonomous Marine  
Vehicle

by

Alecia A. Hurst

A Thesis Submitted to the College of Engineering Department of Mechanical  
Engineering in Partial Fulfillment of the Requirements for the Degree of  
Master of Science in Mechanical Engineering

Embry-Riddle Aeronautical University  
Daytona Beach, Florida  
April 2014

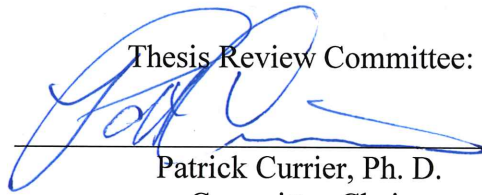
3D Simulation of the Velodyne HDL-32E Lidar Integrated with an Autonomous Marine Vehicle

by


Alecia A. Hurst

This thesis was prepared under the direction of the candidate's Thesis Committee Chair, Dr. Patrick Currier, Professor, Daytona Beach Campus, and Thesis Committee Members Dr. Charles F. Reinholtz, Professor, Daytona Beach Campus, and Dr. Eric Coyle Professor, Daytona Beach Campus, and has been approved by the Thesis Committee. It was submitted to the Department of Mechanical Engineering in partial fulfillment of the requirements for the degree of Master of Science in Mechanical Engineering

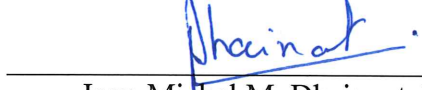
Thesis Review Committee:



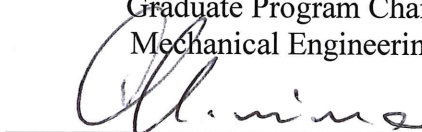
Patrick Currier, Ph. D.  
Committee Chair




Eric Coyle, Ph. D.  
Committee Member




Jean-Michel M. Dhainaut, Ph.D.  
Graduate Program Chair,  
Mechanical Engineering



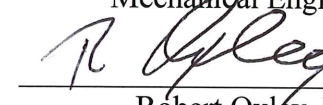
Maj Mirmirani, Ph.D.  
Dean, College of Engineering



Charles F. Reinholtz, Ph.D.  
Committee Member



Charles F. Reinholtz, Ph.D.  
Department Chair,  
Mechanical Engineering



Robert Oxley, Ph.D.  
Associate Vice President of Academics

11-3-14  
Date

## Acknowledgements

I would like to express the sincerest appreciation to my committee chair Dr. Patrick Currier, for his patience, time, advice, help, mentoring and clarity. His supervision, wisdom and aid in direction greatly contributed to making this thesis possible, and for that I am deeply grateful.

I would also like to thank my committee members, Dr. Charles Reinholtz and Dr. Eric Coyle, who directed me to further consider the physical capabilities of obstacle detection with the Velodyne HDL-32E Lidar used in this thesis. Both instructors have also served as thoughtful, helpful, and intelligent mentors throughout my graduate studies. I am also thankful for the time they have taken to contribute to my thesis and be on my committee.

In addition, I would like to thank to Dr. Yan Tang, who provided aid in testing and error considerations, provided graduate study advice, and moral support with the transitioning of the thesis subject.

Last, but not least, I would like thank my family for their support, love, and inspiration throughout my life and academic career.

## Abstract

Researcher: Alecia A. Hurst

Title: 3D Simulation of the Velodyne HDL-32E Lidar Integrated with an Autonomous Marine Vehicle

Institution: Embry-Riddle Aeronautical University

Degree: Master of Science in Mechanical Engineering

Year: 2014

A 3D simulator is programmed for modeling the Velodyne HDL-32E lidar used on the WAM-V vehicle in the marine environment for obstacle detection. The model takes into account sensor integration, sensor error, and error correction. Theoretical analysis includes consideration of atmospheric refraction, time of flight error, UDP packet and timing, calibration parameter errors, depth spread error, field of view, accuracy, angular resolution, and points per second in the environment. The average distance error shows a variance of a 0.0127 m to 0.8128 m depending on the laser and the distance. Test results produce distance correction equations for each laser beam. For presented example Laser 1, the error between the corrected values and the actual distance values ranges from .02%-1.14%, which is reduced from the uncorrected error ranging from 1.32% to 3.42%. For all 32 Lasers, the real-world uncorrected distance readings have a deviation of  $-1.02\text{E-}05\sigma$  to  $.171\sigma$ , where  $\sigma = 0.0221$  m when the Red Taylor Buoy is at .518 m. The corrected distance readings deviate from  $1.43\text{E-}07\sigma$  to  $0.0931\sigma$ . The simulated uncorrected distance readings deviate from  $-0.411\sigma$  to  $2.77\sigma$ , with  $\sigma = 0.0208$  m. The corrected distance readings in simulation deviate from the standard by  $-.218\sigma$  to  $2.24\sigma$ . The field of view is measured to be 41 degrees. Reflectivity and intensity profiles are presented. Physical textures are also generated based on these profiles from buoy obstacles used in the marine competition tasks. By color, the increasing order of intensity for obstacles is black, green, red, and then white. The final product consists of data used for simulation of the Velodyne HDL-32E and reporting the accuracy of simulated physical values relative to the real world testing.

## Table of Contents

Acknowledgements.....	2
Abstract.....	3
Chapter 1: Introduction.....	12
Competition Obstacles:.....	12
Tasks:.....	12
Buoys:.....	14
Vehicle Model:.....	17
Vehicle Format:.....	17
General Sensor Suite Inputs:.....	17
Specific Sensor Setup.....	17
Initial Software Architecture (Centered on Ground Vehicle):.....	19
Updated Software Architecture (Centered on Marine Vehicle):.....	20
Program.....	20
Environment:.....	21
Chapter 2: Background Literature.....	23
Velodyne HDL-32E Lidar:.....	23
Background:.....	23
Sources of Error.....	27
Calibration Techniques:.....	29
Chapter 3: Theoretical Modeling.....	31
Mechanical Setup.....	31
Sensor Specifications.....	31
Firing Sequence and IR Laser Angle Orientation:.....	31
CAD & Simulated Model.....	32
Error Model.....	33
Depth Spread Error Model.....	35
Error Correction.....	36
Chapter 4: Test Data Results & Analysis.....	37
Detection Range Results.....	37
Trial 1:.....	37
Trial 1 Analysis:.....	40
Trial 2:.....	41

Field of View Results: .....	47
Analysis: .....	49
Buoy Analysis:.....	50
Buoy Geometrical Features: .....	50
Material Analysis:.....	50
Reflectivity Profile Results:.....	52
Profile Graph for Retroreflector Base: .....	58
Intensity Range Results: .....	62
Discerning Between Black and White.....	65
Discerning Between Black, Red and Green .....	65
Point Return Results .....	66
Total Error Correction Equations.....	67
Based on using Lidar Parameters, Adjusted Variables, and Provided Resources: .....	67
Real-World Data Comparison.....	69
Marine Environment Data Analysis: .....	70
Simulation:.....	70
Simulation Models:.....	71
WAM-V in Marine Environment Simulation: .....	82
Chapter 5: Conclusion.....	85
References.....	88
Appendix.....	95
Velodyne Test Plan for Calibration Errors .....	95
Primary Items Under Test: .....	95
Primary Supporting Items .....	95
Test Description: .....	96
Anemometer.....	121
Background.....	121
Anemometer Overview.....	121
Sources of Error.....	122
Error Correction.....	123
Current Meter.....	128
Acoustic Vs. Electromagnetic Current Meter.....	129
Sources of Error.....	129

Error Model .....	129
Reasoning for Not Using Current Meter .....	133



## List of Tables

Table	Page
1 Trial 1 Data Table .....	38
2 Trial 1 Sample Standard Deviation Table.....	39
3 Trial 1 Data Deviation from Sample Standard Deviation Table.....	40
4 Comparison of Minimum and Maximum Average with Multi- Average and Multi-Point Deviation for Laser 1 .....	41
5 Comparison of Minimum and Maximum Average with Multi-Point Average and Multi- Point Deviation for Laser 3.....	42
6 Comparison of Minimum and Maximum Average with Multi-Point Average and Multi- Point Deviation for Laser 5.....	43
7 Trial 2 Section of Data Table for Laser 1 .....	44
8 Laser 1 Example from Average Distance for 32 Lasers Data Table .....	44
9 Laser 1 Example from Error for 32 Lasers Data Table .....	45
10 Corrected Laser Table Sample.....	45
11 Single Data Measurement for Field of View .....	48
12 Example of Data Coordinates Used for Each Laser to Calculate Laser Angle .....	48
13 Field of View Data Table.....	49
14 Material Illumination Data Table.....	52

15	Retroreflector Data for Normalizing.....	52
16	Intensity Range Retroreflectors Data Table.....	53
17	Comparison of Measured Illumination and Measured Intensity for Different Reflectors .....	58
18	Profile for Materials .....	60
19	Percent Difference Table Between the Materials' Normalized Illumination Values .....	61
20	Materials Data Table .....	63
21	Buoy Range Data Table .....	64
22	Black and White Data Table .....	65
23	Color Buoys Data Table.....	65
24	Point Return Data Table.....	66
25	Marine Environment Data Sample Table .....	69
26	Intensity Distribution for Green Taylor Buoy Sections .....	80
27	Intensity Distribution for Red Taylor Buoy Sections .....	81
28	UDP Packet and Timing: Packet Offset Data Table .....	100
29	Detection Range Trial 2 Table .....	101
30	Average Distance for Each Laser Data Table.....	103
31	Error for Each Laser Data Table .....	104

## List of Figures

Figure .....	Page
Figure 1 Task 5 Obstacle Course .....	14
Figure 2 Simulation Setup of Task 5 Obstacle Course with WAM-V vehicle .....	14
Figure 3 Test Buoys (Seattle Marine 2014) .....	15
Figure 4 Light Buoy Details .....	16
Figure 5 Channel Markers Used for Channel Navigation and Obstacle Detection Testing.....	16
Figure 6 The Wave Adaptive Modular Vessel (WAM-V) is used as a base platform for building an autonomous marine vehicle in the RobotX Competition (Left). The final marine vehicle (Right), Minion, used by the Robotics Association builds on the WAM-V (Robotics 2014).....	17
Figure 7 Ground Vehicle Architecture.....	20
Figure 8 Basic Marina Environment with 3 Layer Child Script and without Obstacles.....	21
Figure 9 Velodyne HDL-32E Lidar and Setup Accessories .....	31
Figure 10 Velodyne HDL-32E Lidar's Six-Axis Motion.....	31
Figure 11 Firing Order Sequence and Vertical Angle Position of Each Laser .....	31
Figure 12 Basic Setup Before Calibration Coding.....	32
Figure 13 Model of Velodyne HDL-32E Lidar with 32 Lasers.....	32
Figure 14 Main Proximity Sensor Definitions.....	32
Figure 15 Velodyne Lidar's vertical elevation angle correction (Diagram made in CATIA) .....	34
Figure 16 V-REP Model of LMS 111 Lidar with Vision Sensor Feature and without Texture (Left) and with Texture (Right) on Ground Terrain. Lidar used for comparison in Lidar Alignment Method. ....	37
Figure 17 Range Testing of Velodyne's Individual Lasers .....	37
Figure 18 Laser 1 Comparison of Average Detected Distance and Measured Distance to generate Correction Equation for Laser 1.....	45
Figure 19 Comparison of Actual Distance to Error Distances Read for Each of 32 Lasers .....	46
Figure 20 Comparison of Actual Distance to Corrected Distances Read for Each of 32 Lasers .....	47
Figure 21 Field of View Detection with Laser ID Scale.....	48
Figure 22 Field of View Detection Wall Covering Entire Velodyne Angular Range .....	48
Figure 23 Typical Features of a Green Channel Marker.....	50
Figure 24 Typical Features of a Red Channel Marker.....	50
Figure 25 3 3/16" Red Reflector (Circled).....	53
Figure 26 1.25" Green Reflector (Circled) .....	53
Figure 27 1.25" Green Reflector (Circled) at .4622 m, which is closer than Velodyne HDL-32E's .5 m detection threshold. ....	53
Figure 28 Measured Number of Occurrences Distribution for 180 Intensity Points on a scale of 0-255 returned from the Velodyne HDL-32E Lidar, which detects the Large Red Retroreflector at a distance of .75 m. ....	54
Figure 29 Surface of an Orange Retroreflector that shows small cubes used to return Parallel Light(Greenwald 2014).....	55
Figure 30 Deviation of Each Measured Intensity Value from the Calculated Standard Deviation from the Average Intensity for the 3 3/16" Red Retroreflector, where $\sigma=74$ .....	55
Figure 31 Measured Intensity Distribution over a series of points returned from the 1.25" Green Retroreflector that is detected by the Velodyne HDL-32E Lidar at a range of distances (.62 m – 1.43 m).56	56

Figure 32 Comparison of Intensity Distributions for the 1.25" Blue Retroreflector read by the Velodyne HDL-32E Lidar when positioned at different distances ranging from .63 m to 1.12 m. ....	56
Figure 33 Comparison of Intensity Distributions for the 1.25" Clear/White Retroreflector read by the Velodyne HDL-32E Lidar when placed at different distances ranging from .62 m to 1.12 m. ....	57
Figure 34 Comparison of Intensity Distributions for the 1.25" Red Retroreflector read by the Velodyne HDL-32E Lidar when placed at different distances ranging from .63 m to 1.12 m. ....	57
Figure 35 Comparison of Intensity Distributions for the 1.25" Orange Retroreflector read by the Velodyne HDL-32E Lidar when placed at different distances ranging from .62 m to 1.12 m. ....	58
Figure 36 The Minimum Measured Intensity in relation to the Minimum Measured Illumination.....	59
Figure 37 The Maximum Measured Intensity compared with the Maximum Measured Illumination.....	59
Figure 38 Yellow Buoy Intensity Distribution .....	62
Figure 39 Yellow Buoy Approaching Closer than Lidar Range.....	62
Figure 40 Buoy Placed Before Minimum Detection Threshold .....	62
Figure 41 Aluminum Plate Intensity Profile .....	63
Figure 42 Kiln Dried Plank Intensity Profile .....	63
Figure 43 Black Plate Profile .....	63
Figure 44 Steel Panel Intensity Profile .....	63
Figure 45 Red Buoy Intensity Analyzed at Varying Ranges .....	64
Figure 46 Comparison between Red Buoy Profile (Left) and Green Buoy Profile (Right).....	64
Figure 47 White Board with Black Pattern (Left) and Outlined Pattern on Board (Right) .....	65
Figure 48 Point Return in Ground Lab .....	66
Figure 51 Velodyne HDL-32E mounted on WAM-V vehicle in Halifax River.....	69
Figure 49 ERAU WAM-V operating on the Halifax River .....	69
Figure 50 The Dock on the Halifax River.....	69
Figure 52 New Default Scene in V-REP PRO EDU.....	70
Figure 53 Buoys in 3DS Max developed with light sources and surface meshes integrated. Note: The light tower design is prior to Updated Maritime Rules 03/21/14. The buoys are generic.....	71
Figure 54 Taylor Buoys (White, Red, and Green) .....	71
Figure 56 Setup of Velodyne HDL-32E Lidar detecting Red Taylor Buoy .....	72
Figure 55 Script Editor for Simulation Environment.....	72
Figure 57 Velodyne HDL-32E Lidar Detects (Yellow Highlight) Red Taylor Buoy.....	73
Figure 58 Velodyne HDL-32E generating 3D point cloud (with segment option off) .....	73
Figure 59 Lidar Detection of Buoy with Console Display of Actual Distance, Error Distance, and Corrected Distance in Meters.....	74
Figure 60 Output of Actual Measured Distance, Simulated Distance with Error, and Corrected Distance.....	74
Figure 61 Comparing the Simulated and Real-World Values read from each laser of the Velodyne HDL-32E, which is .518 m from the Red Taylor Buoy .....	74
Figure 62 Comparison of the Percent Error for the Corrected Simulated and Corrected Real-World Distance values read from each of the 32 lasers in the Velodyne HDL-32E, which is .518 m from a Red Taylor Buoy .....	75
Figure 63 Comparison of the Deviation from Standard Deviation of the Simulated Distances and Corrected Simulated Distances for the Red Taylor Buoy placed 0.518 m from the Velodyne HDL-32E Lidar. The standard deviation for this graph is 0.0193 m. ....	76
Figure 64 Comparison of the Deviation from Standard Deviation of the Real-World Distances and Corrected Real-World Distances for the Red Taylor Buoy placed 0.518 m from the Velodyne HDL-32E Lidar. The standard deviation for this graph is 0.0221 m. ....	77

Figure 65 Scene Object Shape Properties User Interface associated with Green Taylor Buoy .....	77
Figure 66 Scene Object Common Properties User Interface associated with Green Taylor Buoy .....	78
Figure 67 Image filtering layers to set scales and interpret reflective properties of objects so Velodyne HDL-32E Lidar can output intensity values .....	78
Figure 68 Detection of Red Taylor Buoy's Intensity Values with Console displaying Minimum, Maximum, and Average Intensity Values.....	79
Figure 69 Intensity Value Setup Applied to Green Taylor Buoy in Scene including White Taylor Buoy, Red Taylor Buoy, and Green Taylor Buoy .....	79
Figure 70 Intensity Values for Green Taylor Buoy Body and Reflector against Base Minimum Intensity of Zero.....	80
Figure 71 Intensity Data of the Green Taylor Buoy read from Velodyne HDL-32E Lidar, accompanied by the intensity spectrum scale using VeloView (Left). In comparison, the simulated Green Taylor Buoy (Right) shows the simulated intensity values accompanied by its intensity spectrum scale.....	80
Figure 72 Intensity Data of the Red Taylor Buoy read from Velodyne HDL-32E Lidar, accompanied by the intensity spectrum scale using VeloView (Left). In comparison, the simulated Red Taylor Buoy (Right) shows the simulated intensity values accompanied by its intensity spectrum scale.....	81
Figure 73 WAM-V vehicle integrated into V-REP environment with generated marine scene .....	82
Figure 74 WAM-V marine vehicle in marine environment with obstacles .....	82
Figure 75 Velodyne HDL-32E Lidar mounted on WAM-V in Marine Environment detecting Obstacles and returning parameters, including Distance and Intensity (as demonstrated in Floating View) .....	83
Figure 76 Velodyne HDL-32E Lidar mounted on WAM-V in Marine Environment while detecting obstacles but receiving minimal detection return from water because of Water Texture Properties.....	83
Figure 77 Simulation of WAM-V in Marine Environment with 3-D Point Cloud Generation Running....	84
Figure 78 "Schematic of two different sonic path designs" .....	121
Figure 79 Wind flow with Rotating Eddies Measured by Anemometer.....	125
Figure 80 Diagram of the Eddy Covariance Method, with movement for parcel of air (c) and associated speed (w).....	125
Figure 81 Eddy Flux Equation Application .....	125
Figure 82 Flow, Pitch, and Roll Convention for a Current Meter .....	129
Figure 83 Diagram of Current Meter's Coordinate System based on the Horizontal and Vertical Cosine Response Functions and the corresponding angles A and B.....	130

## Chapter 1: Introduction

The development of autonomous vehicles is becoming more prevalent in today's society with the increase in demand for safety and effectively accomplishing tasks without human error or risk. Vehicle development entails bench and field testing systems and subsystems. Physical testing depends on available resources, labor, and time, and as a result can be costly. Simulations aid in minimizing the required amount of field testing and wear on equipment to ensure the system works by solving algorithm, programming, communication, and setup errors. These simulations also help narrow down what needs to be field tested within the runtime limited by the vehicle's power source.

The purpose of this research is to develop a simulation environment modeling the Velodyne HDL-32E Lidar sensor along with its sensor error during operation and sensor error correction to allow for reliable obstacle avoidance and navigation of a boat in a marine environment. The Robotics Association at Embry-Riddle Aeronautical University selected the Velodyne HDL-32E Lidar as the main vision sensor to effectively provide a three dimensional point cloud map of the boat's surroundings and aid in navigation through the marine environment. The simulated environment used for the sensor and marine vehicle is three dimensional and customizable. Building a customizable simulation environment enables virtual testing of how the Velodyne HDL-32E Lidar on a marine vessel will detect the surroundings, which can include obstacles in a course. After understanding how the vision sensor detects obstacles, the user can test and optimize the marine vehicle's vision processing, controls, and navigation. The boat used in conjunction with the Velodyne HDL-32E Lidar's analysis for the simulation is the Wave Adaptive Modular Vessel (WAM-V) vehicle provided by the Maritime RobotX competition that the Robotics Association at Embry-Riddle Aeronautical University is competing in as one of three teams representing the United States of America. The purpose of the RobotX competition is for teams of students worldwide to build on a standard maritime platform by using sensors, hardware, and software. These maritime vehicles are then required to navigate a course consisting of various maritime surface vehicle missions with a set a qualification requirements and points. The WAM-V vehicle includes a propulsion system, a navigational sensor suite, an environment sensor suite, a power system, and a computer system.

### Competition Obstacles:

#### Tasks:

The Maritime RobotX course consists of a series of tasks that the WAM-V boat must successfully navigate through.

#### *Task 1: Navigation and Control*

The first task is to pass through the first gate and then through the second gate which indicates the end of the course.

A pair of buoys spaced at 10 meters represents each gate and consists of a green buoy to starboard and a red buoy to port. The length of the course is a maximum of 100 meters (RobotX 2014).

#### ***Task 2: Underwater Acoustic Signal Identification***

The second task requires the marine vehicle to autonomously identify and locate the source of an acoustic signal emitted underwater. The search area for this signal will be a minimum of 40m wide and a maximum of 100m long. The acoustic transmitters attached to anchored buoys will be placed randomly in the search area. The buoys will not necessarily be visible via the surface. One of the devices will emit the signal and the rest will remain silent. Points will be awarded to the team passed on accuracy of position reporting (RobotX 2014).

#### ***Task 3: Symbol Identification and WAM-V Docking***

The third task requires the marine vehicle to identify one of three marked docking bays, locate it, maneuver to that identified docking bay, stop, and exit the bay. Then the marine vehicle will move to the next task or terminate run (RobotX 2014).

#### ***Task 4: Light Tower Buoy Observation and Reporting***

The WAM-V is required to execute “light buoy” observation to determine the flashing sequential light pattern. The marine vehicle will then autonomously report the light buoy’s determined color sequence. The “light buoy” is a white buoy with a vertical light bar located within a 40x60 m area. The light bar of the buoy will be no more than 3 m above the water surface and will display the three colors (red, green, or blue), black, and white. Each color appears for a 500 millisecond interval and then remains off for 2 seconds before the pattern repeats again (RobotX 2014).

#### ***Task 5: Detect and Avoid Obstacles***

The fifth task’s purpose is for the marine vehicle to complete a course in the shortest time while avoiding contact with all obstacles and gates. The marine vehicle must navigate through an Entry Gate (1, 2, or 3), autonomously navigate through the field of various stationary, floating obstacles, and complete the course by passing through the designated Exit Gate (X, Y, or Z) (RobotX 2014).

For this example, the assigned Entry Gate is **3** and the assigned Exit Gate is **X**.

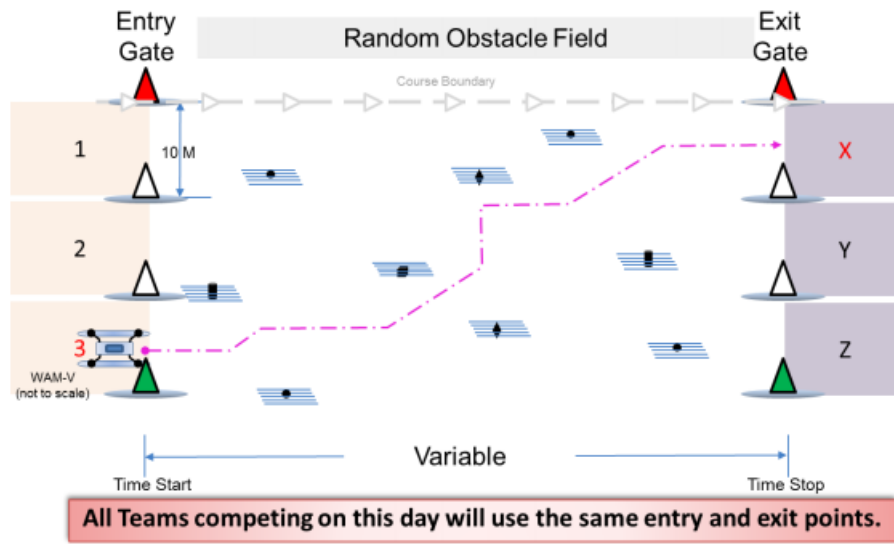


Figure 1 Task 5 Obstacle Course

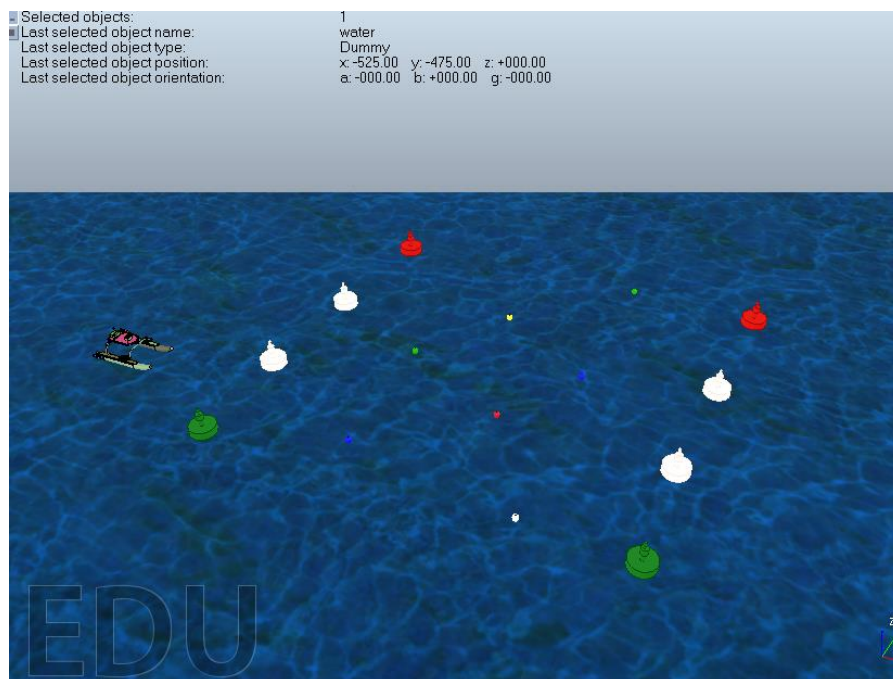


Figure 2 Simulation Setup of Task 5 Obstacle Course with WAM-V vehicle

## Buoys:

Buoys are flotation devices either anchored or drifting in a body of water. Three common types of buoys are Sea mark Buoys, DAN buoys, and Fairway Buoys. Sea mark buoys, which include lateral and cardinal buoys, mark maritime channels, hazards, and administrative areas (Sealite 2010). DAN buoys, among other safety functions, can serve as platforms for light or radio beacons, temporary markers, or lifebuoys with flags (Dan 2013). Fairway Buoys can be used to indicate the end of a channel, safe waters, a safe route through shallow waters, or the start and



end of a buoyed section of a continuous narrow channel (Canadian 2011). For the purpose of this competition, buoys serve as boundary markers, obstacle markers for course navigation, mounts for underwater ultrasonic detection, and a tower for visual detection of a light pattern. Buoys can be made from a variety of durable materials such as Polyethylene, Acrylonitrile Butadiene Styrene (ABS), LLDPE, and HDPE.

For marine environments based on Michigan Boating Navigational Aids, there are three types of buoys for port and another set for starboard. The green port buoys are a green lighted buoy, a can buoy, and a green square Daymarker. On the starboard side, there are lighted red buoys, a red nun buoy, or a red triangular Daymarker. Channel Daymarkers consist of a triangular retroreflective panel connected to a wooden pole (Nautical 2012).

The first set of buoys used for the research is the A-series buoys. These buoys come in a range of sizes and colors. For the study, the yellow, blue, red, and green buoys are considered in the lab and marine environment. The A-series buoys made by Polyform U.S. are made of a proprietary formulation of polyethylene that is adjusted per buoy (Polyform 2003).

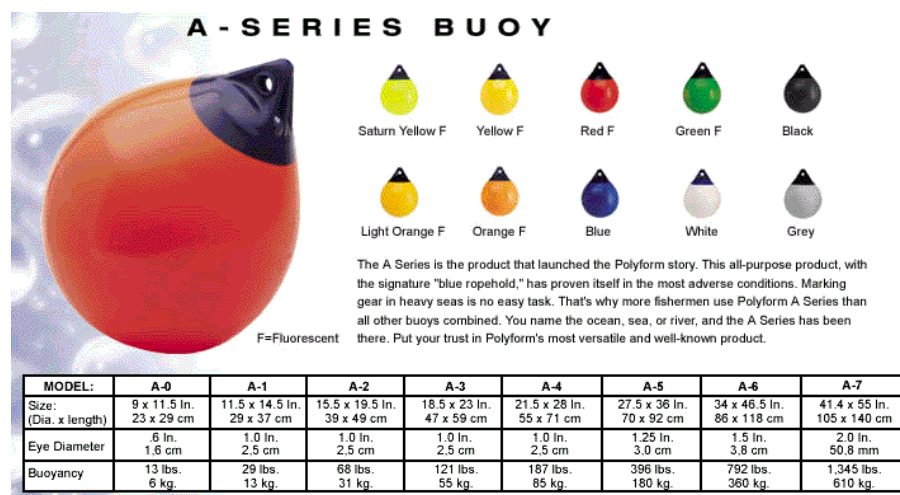


Figure 3 Test Buoys (Seattle Marine 2014)

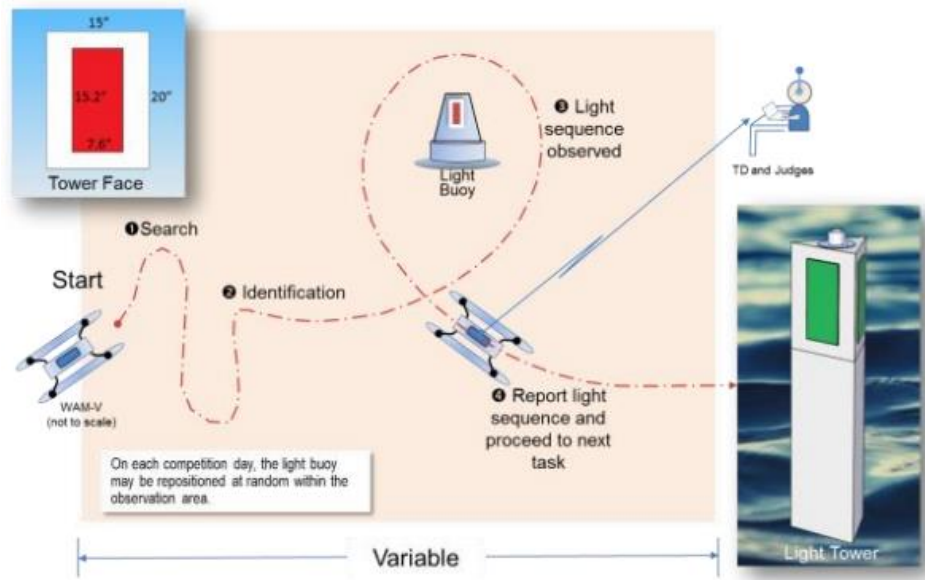


Figure 4 Light Buoy Details

Another pair of buoys used for obstacle analysis in this thesis and potentially used in the RobotX competition is the Surmark Marker Buoys manufactured by Taylor Made in green and red. The red buoy in Figure 5 has the consistency of a red, triangular daymarker buoy with red reflector tape near the top. The red buoy is designated for the marine vehicle's starboard. The green buoy, however, is a port buoy with the structure of a daymarker. The green buoy has a rectangular, can shaped body with green reflector tape as well. These 49" tall and 10" diameter buoys with a buoyancy of 40 lbs. are molded from impact resistant and U.V. stabilized polyethylene. The ring base at the bottom of each of buoys has a diameter of 18" (Boat Depot 2014).



Figure 5 Channel Markers Used for Channel Navigation and Obstacle Detection Testing

## Vehicle Model:

### Vehicle Format:

The marine vehicle used within the RobotX competition is known as the Wave Adaptive Modular Vessel (WAM-V). The WAM-V platform was developed by Marine Advanced Research, Inc. as a “new class of watercraft based on patented technology that delivers a radically new seagoing experience” (Marine 2014). The WAM-V’s structure is ultralight, flexible, modular, and applicable for manned or unmanned operations. The vessel used for the RobotX competition is 13 ft. long and 8 ft. wide. The WAM-V consists of a payload platform connected to a suspension system, articulating joints, and two pontoons. The payload tray weighs about 54.5 pounds and has a 300 lbs. maximum capacity. The ball joint, shock absorbers and springs help reduce the amount of stress on the structure when the vehicle is static or in dynamic motion. The pontoons are designed to absorb high frequency waves, allowing for flexibility and conformation to the water’s surface (RobotX 2014). The overall statics and dynamics of the vehicle in the real-world marine environment impact the Velodyne HDL-32E’s sensor error in detecting points and generating points for the 3D point cloud, but the wave disturbance absorption helps reduce the effect.



Figure 6 The Wave Adaptive Modular Vessel (WAM-V) is used as a base platform for building an autonomous marine vehicle in the RobotX Competition (Left). The final marine vehicle (Right), Minion, used by the Robotics Association builds on the WAM-V (Robotics 2014).

### General Sensor Suite Inputs:

The Robotics Association’s navigational suite integrated with the WAM-V consists of a TORC Pinpoint GPS system, a Velodyne HDL- 32E 3D Lidar, hydrophones and a webcam. The environment suite initially included a Valeport 803 current meter and either the Gill WindSonic M ultrasonic wind sensor, the Wind Monitor SE MA 09106, or a 3D Young Model 81000 ultrasonic anemometer. The current meter and anemometer were removed from the suite because of reasons discussed in the Appendix of this paper. The information in the following sensor section is based on the initial research done for the autonomous vehicle.

### Specific Sensor Setup:

The Velodyne HDL-32E Lidar is a "small and ruggedly built" sensor with a 5.9" height and 3.4" diameter for dimensions, and a weight less than 2 kg. The sensor has 32 laser detector pairs that

are Class 1 905nm lasers with a range of 1-80 m. The sensor has a 360 degree horizontal FOV with a +10.67 to -30.67 degree vertical FOV. The operating temperature is -10 - +60 C and the storage temperature is -40-+105 C. The degree of accuracy is <2cm (one sigma at 25 m) along with a vertical angular accuracy of 1.33 degrees. The HDL-32E Lidar withstands a max shock of 500 m/s<sup>2</sup> amplitude for an 11 msec duration, and can handle 5Hz-2000Hz vibration for 3G rms. The sensor outputs a maximum of 700,000 points/sec. The output UDP (User Datagram Protocol) packets contain distances, calibrated reflectivities, and rotation angles. The Lidar uses internal MEMS accelerometers and gyros for six-axis motion correction to output orientation and also uses a GPS Receiver for GPS time-synchronization (Velodyne 2014).

Currently, the vehicle implements Microsoft Lifecam Cinema cameras. The Lifecam cameras are 0.94" wide, 2.19" in height, and 1.81" long. They come with a 120 degree wide angle field of view. The cameras also have features such as autofocus, TrueColor technology for object detecting and tracking by controlling video exposure, 360-degree rotation, 720p HD video with up to 30 frames per second. Included ClearFrame Technology corrects for video in low light conditions (Microsoft 2014).

Sparton PHOD-1 hydrophones have flat broadband frequency response, omnidirectional capability, low power, low noise, and built-in calibration. With a cable 10 m in length, hydrophones have a usable frequency range of 10 Hz to 50 kHz, and a resonance of 46 kHz. The receive sensitivity is Omni +/- 1 dB to 40 kHz and the vertical directivity is Omni +/- 1 dB to 20 KHz and Omni +/- dB to 40 kHz. The maximum operating depth is tested to 300 m. The hydrophone's preamplifier gain is 37 dB (Sparton 2014). For the competition, the hydrophones are sampled at 500 kHz via a National Instruments DAQ.

The Valeport Model 803 current meter provides relative water velocity data in real time. The current meter consists of a Valeport 2-axis 11.5 cm discus electromagnetic flow sensor, which is made from polyurethane with titanium mounting, that measures the water velocity in 2 axes across the sensor service and comes with processors outputting variable formats. The data is updated at 1-second intervals, providing X and Y axis flow information. The X axis is defined as flow across the vehicle while the Y axis represents flow into the vehicle. The titanium housing has a 3000 m depth rating and 76 mm radial by 350 mm length dimension. The total physical weight of the titanium model is 3.5kg in water and uses an 8 way Subconn BH8M connector. The Model 803's range is +/- 10kts (5m/s) with an accuracy of +/-0.02 (0.01 m/s) kts+1% reading and a resolution of 0.01kts (0.001 m/s).

The 3D Young Model 81000 ultrasonic anemometer uses three pairs of transducers and receivers to measure the three dimensional wind velocity and speed of sound based on time of flight through air of ultrasonic acoustic signals at different angles of attack along the azimuth from 0 to 359.9 degrees. The speed of sound corrected for crosswind effects is used to derive the sonic temperature. The mechanical structure is designed for environmental resistance by using UV stabilized thermoplastic, stainless steel, and anodized aluminum components. For specifications,

the wind speed detection range is 0 to 40 m/s with a resolution of 0.01 m/s and a threshold of 0.01 m/s. The accuracy is  $\pm 1\%$  rms  $\pm 0.05$  m/s for 0 to 30 m/s and  $\pm 3\%$  rms for 30 to 40 m/s. The wind direction detection spans an azimuth range of 0.0 to 359.9 degrees with a resolution of 0.1 degree and a maximum elevation/ angle of attack of  $\pm 60.0$  degrees. The accuracy is  $\pm 2$  degrees for 1 to 30 m/s and  $\pm 5$  degrees for 30 to 40 m/s. The overall height is 56 cm and the support arm radius is 17 cm. The sensor weight is 1.7kg.

The Gill WindSonic M ultrasonic wind sensor has impact resistant, corrosion-free aluminum alloy housing with an optional heating system to address harsh environmental conditions. The wind speed measurement range is 0 to 60 m/s (116 kts) with an accuracy of  $\pm 2\%$  at 12 m/s, a resolution of 0.01 m/s (0.02 kts), a response time of 0.25 seconds and a 0.01 m/s threshold. The wind direction detection range is 0 to 359 degrees with no dead band and 1 degree resolution, and has an accuracy of  $\pm 3$  degrees at 12 m/s with 0.25 second response time. The output measurement parameters are wind speed and direction, or U and V vectors. The anemometer has dimensions of 142mm x 160mm and weighs 0.9 kg.

Despite initial research and interest in using these sensors, the team determined that using a current meter and anemometer is not practical. As stated in the Appendix, the current meter is not usable since Marina Bay has fresh water, and the current meter depends on conductive fluid. The anemometer is outside of the budget and not necessary for implementation.

### **Initial Software Architecture (Centered on Ground Vehicle):**

At the beginning of building a simulation, the initial software architecture (Figure 6) is configured to understand the different components of the simulation. The initial software architecture in Figure 6 was initially developed to the ground vehicle built for the AUVSI's Intelligent Ground Vehicle Competition, but can also be applied to the WAM-V boat in the marine environment for the RobotX competition. The platform consists of five different structures, which are the User Inputs, the Visual Interface, the Environment, Playback, and External Input/Outputs. The User Input consists of the Vehicle Model (Dynamics, AI Control, CAD, and Kinematics), the Error Model Generation, Sensor Suite, Obstacle Objects (Add or Remove), the Controller Input Interface (Keyboard/Mouse, Remote Control, Joystick), Gravity, Surface Friction, Range of Detection, Contact Forces, Joint Constraints, Terramechanics, and a Rigid Tire Model. The Visual Interface included Anti-Aliasing, WxWidgets System, Distortion Correction, Ogre3D, VTK, and the Video/Image Display. Playback inputs Position Info, Video, the Image Sequence and Trajectory Planning into the Visual Interface. The User Input structure inputs into the Environment (Weather, Terrain, Size of Field, etc), the Vehicle-Terrain Interaction (VTI), and the physics engines (PhysX, Bullet, Open Dynamics Engine (ODE), Collision Generator). The External Input/ Output structure consists of the Drive Files, External Controller Plug-ins, and External Analysis Plug-ins (i.e. Numerical, Matlab).

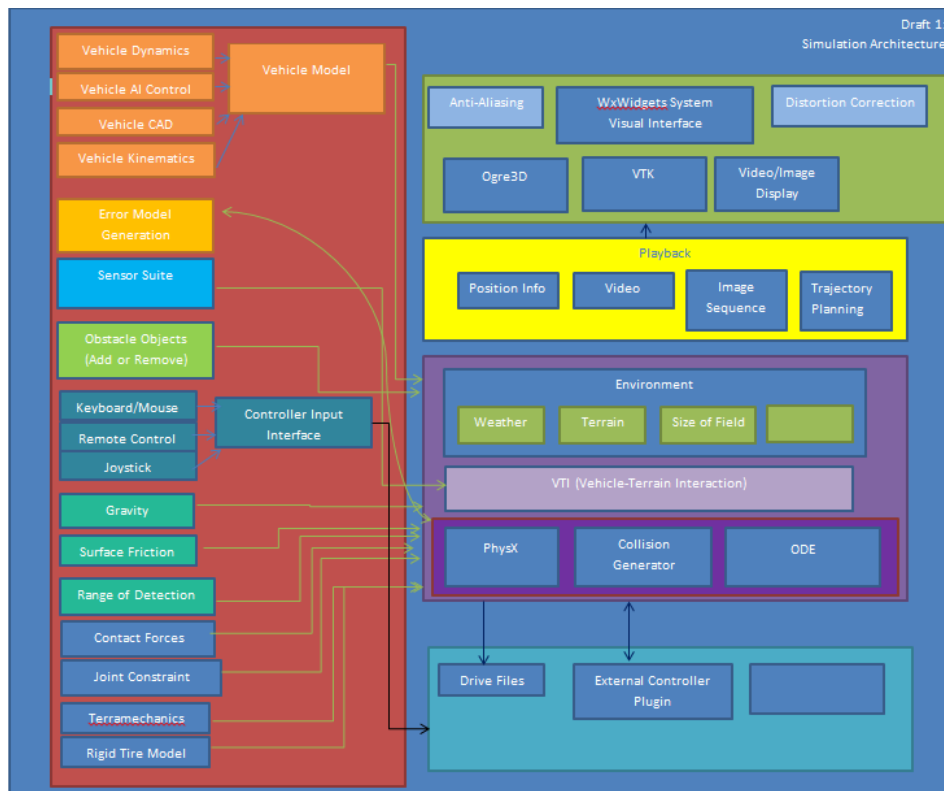


**Figure 7 Ground Vehicle Architecture**

The main factor for deciding whether to use the architecture comes down to development time. The given time frame requires an alternative, but similar, software architecture with a majority of the framework initially included.

## Updated Software Architecture (Centered on Marine Vehicle):

**Program:** V-REP PRO EDU

The current software architecture centers around using the software V-Rep Pro EDU, which provides an interface allowing users to customize a three dimensional environment and develop a simulation centered around a user-defined vehicle model. V-Rep uses the graphical language Lua, which is a light-weight, scripting language descendent of C. The user can define the vehicle dynamics that will adhere to the Open Dynamics Engine (ODE), Bullet (an alternative to PhysX), and Collision Detection physics solution simulation generators.



## Environment:

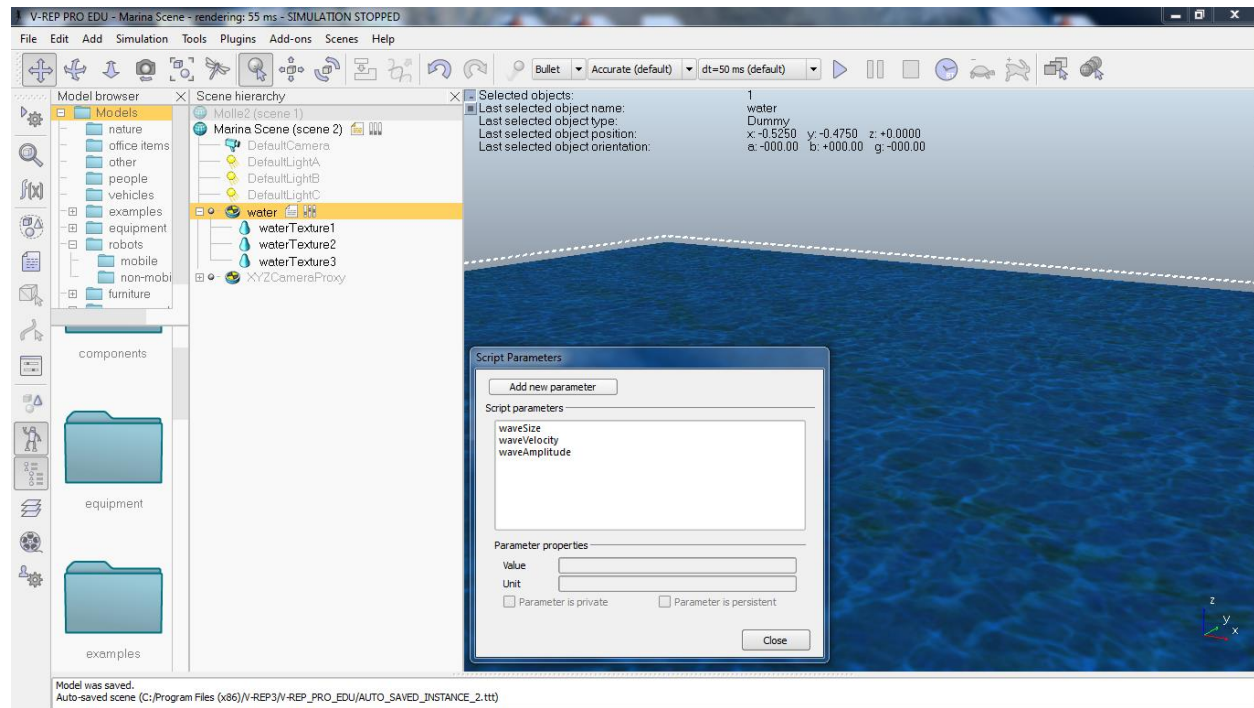


**Figure 8 Basic Marina Environment with 3 Layer Child Script and without Obstacles**

To convert robotic vehicles into the environment (Figure 7), they must be in DXF, OBJ, 3DS, ASCII STL, binary STL, CSV, or heightfield. When a model is converted into V-REP Pro, the entire assembly needs to be scaled and each CAD part within the assembly is considered an individual object. The properties for each individual object must be defined before the assembly can be “merged” together as an entire unit. Joints within the assembly must be created, declared, and defined through threaded or non-threaded child scripts in branches beneath the parent script. Variable user-set parameters can be set with the script parameters box. It is also necessary to align the vehicle’s coordinate system in relation to the world coordinate system, especially for initial position before running the simulation. After initializing the vehicle, the kinematics for the joints and the entire vehicle as a unit can be integrated.

In this thesis, background literature will cover Lidar functions, previously observed Lidar errors, error models, and various methods of calibrating Velodyne Lidars. Then a list of errors that will be theoretically considered and supporting evidence of those errors in the Velodyne HDL-32E Lidar are presented. With the list of errors, a series of tests will be conducted on the Velodyne HDL-32E Lidar to quantitatively measure and analyze non-negligible, practical extrinsic and intrinsic errors. Corrective equations and offset values will be used to simulate the behavior of the Lidar in the V-Rep Simulation scenes. To understand the Velodyne HDL-32E Lidar’s perception of its environment, the buoy obstacles and other materials are evaluated. Data range tables from testing material properties such as intensity will be used to create the surface and texture properties of the obstacles in the simulation environment. The Velodyne HDL-32E Lidar will then be mounted on the WAM-V vehicle in the Task 5 obstacle course and tested for outputs

including obstacle detection, error distance, corrected distance, and obstacle intensities. The simulated environment will then be compared with real-world experimentation to check for simulator validity.



## Chapter 2: Background Literature

### Velodyne HDL-32E Lidar:

#### Background:

The remote sensing technology called Lidar, which is also referred to as LiDAR, LADAR (Laser Detection and Ranging), LRF (Laser Range Finder) or laser altimetry, stands for light detection and ranging. As an active sensor, Lidar works by emitting one or more intense, focused beams of light and measuring the time of flight (TOF) for the light to reflect off a surface and be detected again by the sensor (Schmid, Keil, et al. 2008). For pulsed modulated ranging systems known as time of flight (TOF), a laser emits single light pulses rapid succession called Pulse Repetition Frequency (PRF). The travel time between pulse emission and receiver return is measured. The TOF and speed of light are then used to determine the range from the Lidar to the surrounding environment:

$$Range = R = \frac{1}{2} ct$$

Where  $c$  represents speed of light and  $t$  is the round trip travel time (NGA 2011).

Lidars produce three-dimension coordinates (i.e. X, Y, Z or latitude, longitude, and azimuth) using the TOF, the pulse's firing angle, and the sensor's absolute location relative to the Earth's surface.

These systems typically operate in the electromagnetic spectrum's near-infrared region, but can also operate in the green band. Lidars operating in the green band region are used to detect surface features beneath water and are referred to as bathymetric. The optimal scenario for bathymetric Lidar systems is relatively clear water to allow for measuring seafloor elevations, and absolutely accuracies of 4 to 8 inches (Schmid, Keil, et al. 2008).

Lidar's originally consisted of a single laser that when put in motion could record 3D data of the environment. More recent Lidars are becoming multi-laser scanning systems used for autonomous mobile robotics systems that need to move through an environment and observe surroundings. These multi-laser scanners provide real-time 3D information of the environment and enable accomplishing tasks such as navigation, obstacle detection, SLAM, and modeling (Muhammad 2010).

The calibration of the Lidar is key to generating an accurate 3D reconstruction that presents the best approximation of the features and environment. A method based on ARMA models is one of the first proposals for using a self-calibrating algorithm on a Lidar system (Chen 1993). The Jorgensen investigators reduce the photo detector errors by proposing a model producing the best values for electronic parameters (Jorgensen 1997).

Antone uses an automatic calibration approach involving predefined targets with a pose reliably recognized from a single observation. The geometric calibration factors are calculated using developed numeric algorithms. The Lidar, however, has a limited vision angle and consisted of only one laser. A complete vision angle consisting of 360 degrees and more than one laser are required to generate a 3D environment (Antone 2007).

Stone and his colleagues use the Velodyne HDL-64E and develop a calibration method using several sets of indoor data to calibration only certain detectors. Unique obstacles are placed at known distances and discerned using the data sets. The study determines offsets could be subtracted from the near horizontal lasers to produce correct distance information. Distance errors range between 0.3 and 0.5 meters (Stone 2007).

Bohren focuses on the Velodyne's nominal horizontal and vertical correction factors and introduces an additional distance offset determined by using a reading comparison with the SICK LMS-291. The paper finds laser range uncertainties around 30 cm (Bohren 2008).

Muhammad uses a 4.40 m wide planar wall on a flat surface as a calibration pattern in an optimization technique for the Velodyne HDL-64E. They align the Lidar's fixed frame x-axis to the wall and scan while moving the Lidar from a distance range of 10 to 14m. Then the y-axis is aligned with the wall and the Lidar is again moved at various distances, but with a range from 4 to 8 m (Muhammad 2010).

The paper "LIDAR Velodyne HDL-64E Calibration Using Pattern Planes" describes the calibration method for a Velodyne HDL-64E scanning LIDAR system by using a pattern calibration signature, a mathematical model, and the numerical algorithm for computing Lidar's calibration parameters. The purpose is to minimize systematic errors resulting from geometric calibration factor and provide an algorithm solution for intrinsic and extrinsic parameters. The paper also calculates standard deviation of calibration result errors. Atanacio-Jimenez begins by discussing the difference in the concepts of accuracy and precision in regards to Lidar error analysis. Whereas accuracy relates to bias related to systematic errors, the precision centers on uncertainty from random errors (Atanacio-Jimenez 2011).

Gerardo Atanacio-Jimenez lists sources of systematic errors as imprecise information regarding atomic absorption cross-section, laser absolute frequency calibration, laser lineshape, receiver filter function, photo detector calibration, and geometric factor (Atanacio-Jimenez 2011).

The Lidar system in Atanacio-Jimenez's paper uses a Veldoyne HDL-64E Lidar, which has a 360 degree azimuth field of view (FOV) defined as  $\theta$  and a 26.5 degree elevation FOV ( $\phi$ ). The Lidar has a 15 Hz frame refresh rate and populates up to one million points per second in its point cloud. The instrument consists of 64 lasers split evenly into upper and lower blocks that spin about its z-axis (Atanacio-Jimenez 2011).

By using the five correction factors (Vertical Correction, Rotational Correction, Distance Correction, Horizontal Offset Correction, and Vertical Offset Correction), the paper develops a

calibration mathematical model. A spherical global coordinate system with the origin located at the Lidar sensor is defined. The point cloud is modeled as:

- AllPointCloud =  $f(r, \theta, \varphi)$

where  $r$  is the surface radius,  $\theta$  represents the zenith angle, and  $\varphi$  is the unit sphere's azimuthal angle. Each position on the unit sphere is converted to Cartesian coordinates, while considering the perturbations for extrinsic and intrinsic parameters. These points are implemented into the 3D point cloud approximate mathematical model's heuristic. Each perturbed coordinate for a specific laser  $i$  becomes:

$$\begin{aligned} x'_i &= d'_x \sin(\theta + \Delta\theta_i) - (h_{osc})_i \cos(\theta + \Delta\theta_i) \\ y'_i &= d'_x \cos(\theta + \Delta\theta_i) + (h_{osc})_i \sin(\theta + \Delta\theta_i) \\ z'_i &= (ds_i + \Delta ds_i) \sin(\varphi_i + \Delta\varphi_i) + (v_{osc})_i \sin(\varphi_i + \Delta\varphi_i) \end{aligned}$$

Where  $d'_x = (ds_i + \Delta ds_i) \cos(\varphi_i + \Delta\varphi_i) - (v_{osc})_i \sin(\varphi_i + \Delta\varphi_i)$ ,  $i=1, 2, \dots, 64$ . With 64 lasers, the mathematical model computes 320 intrinsic parameters based on the five intrinsic parameters per laser  $i$ :  $\Delta\theta_i$ ,  $(h_{osc})_i$ ,  $(v_{osc})_i$ ,  $\Delta\varphi_i$ , and  $\Delta ds_i$ . (Atanacio-Jimenez 2011)

The calibration method consists of setting the initial intrinsic parameters, the extrinsic parameters, and the 3D data of the pattern. The algorithm uses steps to minimize incremental specific parameters from converging on a local minimum. The setup consists of a target made up of five planes, which are four walls and the floor. The first estimation derives from measuring the angle shift between the planes, with four being used as a target. The Lidar's z-axis is aligned parallel to the target frame's z-axis and  $ds_i$  becomes:

$$ds_i = \frac{A}{\cos(\varphi_i) \cos(\theta)}$$

Where  $A$  represents the distance from the Lidar to the plane, and laser number  $i=1, 2, \dots, 64$ .

By considering a single laser to be a reference and the other lasers displaced by an angle  $\Delta\theta_i$ , the displacement model equation would be:

$$ds_i = \frac{A}{\cos(\varphi_i) \cos(\theta + \Delta\theta_i)}$$

The study uses laser 1 as a reference and compares the aligned lasers with lasers in a 15 degree misalignment. The displacement between the local minimum values indicates the laser orientation displacement. (Atanacio-Jimenez 2011)

When considering the extrinsic parameters, the planes are referenced in respect to the Lidar frame, and the Lidar frame position and orientation are the same as the pattern frame. The distance of the plane is determined with respect to the Lidar, with the plane equation being:

$$n_j[r - r_j]^T = 0,$$

Where  $j = 1, 2, 3, 4, 5$ . The term  $r_j$  represents the position vector for point  $p_j$  that exists in the plane, while  $n_j$  is the nonzero vector normal to the plane  $j$ . These vectors for the five planes are defined as:

$$\{n_j\} = \left\{ \begin{bmatrix} 1 \\ 0 \\ 0 \end{bmatrix}, \begin{bmatrix} 0 \\ 1 \\ 0 \end{bmatrix}, \begin{bmatrix} -1 \\ 0 \\ 0 \end{bmatrix}, \begin{bmatrix} 0 \\ -1 \\ 0 \end{bmatrix}, \begin{bmatrix} 0 \\ 0 \\ -1 \end{bmatrix} \right\}$$

$$\{r_j\} = \left\{ \begin{bmatrix} \frac{A_1}{2} & 0 & 0 \end{bmatrix}^T, \begin{bmatrix} 0 & \frac{A_2}{2} & 0 \end{bmatrix}^T, \begin{bmatrix} \frac{A_1}{2} & 0 & 0 \end{bmatrix}^T, \begin{bmatrix} -\frac{A_1}{2} & 0 & 0 \end{bmatrix}^T, \begin{bmatrix} 0 & 0 & -A_2 \end{bmatrix}^T \right\}.$$

In actuality, the study considers the pattern calibration frame to be rotated and translated relative to the Lidar frame. Thus the extrinsic parameters are rewritten as:

$$(\mathbf{R} \circ \mathbf{T}) \{n_j[r - r_j]^T\} = 0,$$

Where  $\mathbf{R}$  is the rotation and  $\mathbf{T}$  is the translation in the rigid transformation from the lidar frame to the pattern frame, which is in the center of the four walls (Atanacio-Jimenez 2011).

In generating the 3D points, the values produced by the Lidar must be considered. These values are pan rotation ( $\theta$ ), the laser's tilt orientation ( $\varphi_i$ ), measured distance by angled laser ( $ds_i$ ) and the signal intensity. The first three parameters are corrected with the previously mentioned equations, but each laser's signal must be computed using the intersection of the planes using the three parameters along with the intrinsic parameters  $\{\Delta\theta_i, (h_{osc})_i, (v_{osc})_i, \Delta\varphi_i, \Delta ds_i\}$ . The laser  $i$  signal is:

$$S_i = [x_i^S \quad y_i^S \quad z_i^S]^T = f_i(\theta, \varphi_i, ds_i, \Delta\theta_i, \Delta\varphi_i, (v_{osc})_i, \Delta ds_i, (h_{osc})_i, \mathbf{R}, \mathbf{T}).$$

From the Lidar values and parameters, the 3D points:

$$p'_i = g_i(\theta, \varphi_i, ds_i, \Delta\theta_i, \Delta\varphi_i, (v_{osc})_i, \Delta ds_i, (h_{osc})_i),$$

can be computed. The initialization of the extrinsic parameters involves measuring the pattern calibration and locating the center of each parameter's frame. The total calibration leads to a refinement stage with total minimization (Atanacio-Jimenez 2011):

$$F = f(\theta, \varphi_i, ds_i, \Delta\theta_i, \Delta\varphi_i, (v_{osc})_i, \Delta ds_i, (h_{osc})_i, \mathbf{R}, \mathbf{T}) \\ - g(f(\theta, \varphi_i, ds_i, \Delta\theta_i, \Delta\varphi_i, (v_{osc})_i, \Delta ds_i, (h_{osc})_i),$$

Which can also be represented in compact form as:

$$F = \begin{bmatrix} F_1 \\ F_2 \\ F_3 \end{bmatrix} = \begin{bmatrix} x_i^S \\ y_i^S \\ z_i^S \end{bmatrix} - \begin{bmatrix} x'_i \\ y'_i \\ z'_i \end{bmatrix}.$$

Atanacio-Jimenez 2011 uses Matlab's Levenberg-Marquardt's method in the minimization, which requires solving the system of equations:

$$\frac{\partial F_1}{\partial \Gamma} = 0, \frac{\partial F_2}{\partial \Gamma} = 0, \frac{\partial F_3}{\partial \Gamma} = 0,$$

Where,  $\Gamma = \{ \Delta\theta_i, \Delta\phi_i, (v_{osc}), \Delta ds_i, (h_{osc}), \mathbf{R}, \mathbf{T} \}$ .

The extrinsic parameters computed with minimization to match the Lidar frame and calibration pattern show via a histogram to have a mean error of 22.4cm with a 9.72 cm<sup>2</sup> variance. This mean error is greater than the Lidar technical guide's reported 5cm and less than Bohren's another 30 cm initial error (Bohren 2008). The difference between the nominal parameters and computed parameters were between 2.3 cm and 5.2 cm. The mathematical model and numerical algorithm used to determine the Lidar's calibration parameters demonstrated a simulated level of precision of approximately 1.56 cm. As a result, the Atanacio-Jimenez's method demonstrates the ability to minimize reconstruction error, which is useful for developing simulation, dynamic testing, and reconstruction models (Atanacio-Jimenez 2011).

### Sources of Error

The following sources of error summarize those suggested by literature review and from consideration, supported by references, of the sensor in the lab or marine environment:

The Velodyne HDL-32E Lidar can output data with error resulting from sources including two-way electromagnetic interference, UDP broadcast flooding, calibration errors, and thermal errors. Before correcting, these errors must be identified, tested, and understood in-depth using theoretical and real-world data (Halterman 2010).

The first of these possible errors is a physical occurrence known as two-way electromagnetic interference. Suggested by Halterman, Lidar interference affects GPS receivers just as the Lidar is affected by marine RADAR pulses. In particular, RADAR induced noise arises in Lidar data as horizontal and vertical spreads. The periodic occurrence of the noise is dependent on the RADAR antenna's spin rate. This noise also has a random height profile (Halterman 2010).

Another source of error is UDP broadcast flooding. The output UDP (User Datagram Protocol) packets contain distances, calibrated reflectivities, and rotation angles. UDP broadcast flooding occurs when sensor data is sent via the Ethernet interface. This data is packaged in UDP broadcast packets, allowing for simple data retrieval. These packets, however, can flood the interface, resulting in retrieval errors (Halterman 2010).

Other errors with the Velodyne HDL-32E Lidar can arise from difficulties in obtaining accurate calibration. The scanner has thirty-two different lasers at different oriented angles in two groups

of firing. Each laser is calibrated according to five parameters. These five parameters are vertical correction, rotation correction, distance correction, vertical offset correction, and horizontal offset correction. The manufacturer provided calibration parameters are not necessarily sufficient. Errors from these five parameters lead to drifted data points. Errors in vision processing and object isolation algorithms can arise from dependency on accuracy and consistency between lasers (Muhammad 2010) (Halterman 2010) (Antone 2007).

Some of these calibration errors are range dependent. An instance of range dependent errors is depth spreading. Depth spreading, or beam divergence, occurs when a Gaussian Beam focused to a spot begins at a certain distance to rapidly spread out or diverge into a cone-shape inversely proportional the spot size (Svelto 2010).

Laser timing can also present errors within the data. The Velodyne Lidar uses GPS time stamps to determine the exact firing time for each laser. These time stamps also allow for properly time-aligning HDL-32E point cloud with other data sources. The GPS time stamps work as follows (Velodyne 2014):

1. Ethernet packet assembled in real time
2. Encoder angle associated with first laser shot in each 32 laser shot collection
3. Time stamp reported in last 6 bytes relates to last shot of last group in entire sequence (of 12 records)
4. Time stamp synchronized to leading edge of GPS's PPS signal (for Garmin GPS-18LV GPS receiver)
5. Lasers fired on clock running at 1.152 microsec cycle time
6. 40 time periods per 32 firings with dead time being used to recharge lasers
7. Thus, total time to fire all 32 lasers is 46.08 microsec.
8. Each packet has twelve of the 32-laser firing groups
9. Total packet time is 552.96 microsec.
10. 1808 packets per second, or 694, 292 laser shots per second

Atmospheric refraction can also serve as a source of error for Lidar systems based on point-scanning. Calculations to determine distance are based on time of flight at the speed of light which refracts through physical mediums depending on atmospheric conditions. As a result, the path of the light will vary and affect the time of flight and resultant distance accordingly (NGA 2011).

Intensity is the power per unit solid angle from a point source to a particular direction. Effective calibration is not usually implemented for Lidar when calculating absolute intensity. As a result, relative intensity is usually reported. For example, the return value is usually an integer for linear mode systems as a result of mapping the return's signal power to an integer value based on a reference table (NGA 2011).

### Calibration Techniques:

Sensor performance relies on initial calibration to give precise observations of the environment. Successful calibration minimizes the difficulty in isolating features includes lines and planes. Techniques range from using laser scanning systems to calibrate a Lidar on a mobile robot to calibrating additive and proportional distance correction factors. Another proposed method, supported by Muhammad's research (Muhammad 2010), compares a Lidar with a SICK's distance readings (Figure 15).

Muhammad proposed a calibration method for the Velodyne HDL-64E S2 implementing an optimization process comparing scanned data with the ground truth environment. The Lidar consisted of a spinning head of 64 lasers grouped into two upper blocks and two lower blocks. Five parameters characterize each laser to convert the distance value into 3D points. These parameters are rotational correction angle, vertical correction angle, distance correction factor, vertical offset, and horizontal offset. Each laser is oriented at a different angle and the distance returned value is converted to 3D point P ( $P_x$ ,  $P_y$ , and  $P_z$ ) in Cartesian expressed in the Lidar's frame:

$$D = D_{ret} + D_{corr}$$

$$D_{xy} = D * \cos(\theta) - V_{offset} * \sin(\theta)$$

$$P_x = D_{xy} * \sin(\beta) - H_{offset} * \cos(\beta)$$

$$P_y = D_{xy} * \cos(\beta) + H_{offset} * \sin(\beta)$$

$$P_z = D * \sin(\theta) + V_{offset} * \cos(\theta)$$

$D_{corr}$  represents the correction value to be added to the Lidar's returned distance value  $D_{ret}$ , which results in a total corrected distance value  $D$ . The  $\alpha$  term refers to the rotational correction angle of the laser with the y-x plane. If  $\varphi$  is the current rotational angle, then  $\beta = \varphi - \alpha$ . Also, the vertical correction angle  $\theta$  is made between the laser beam and the x-y plane. The values  $D_{corr}$ ,  $\alpha$ , and  $\theta$  must be calibrated correctly because improper calibration induces error in the precision of 3D coordinates that varies with distance of a scanned object. Imprecise calibration induced errors for  $V_{offset}$  and  $H_{offset}$  will not vary with an object's distance.

The method requires an environment that allows for the determination of a cost function to quantitatively compare point cloud data with the real environment. The cost function will provide lower costs for more accurate matches and optimize the calibration parameters by being dependent on each. For the study, a 4.40m wide planar wall on a flat surface serves as the environment and the wall was scanned at various distances and orientations from the wall, which included x-axis alignment and then y-axis alignment. Since the environment consists of a plane/wall, the chosen cost function was the variance of distance data in relation to the wall's thickness, where the front is zero thickness. With the wall aligned to the y-axis of the Lidar's

fixed frame, the current scan's cost equals the average squared perpendicular distance between the  $P_x$  for each point and the mean  $P_x$  for all current points:

$$C_y = \sum (P_{x,i} - P_{x,mean})^2 / n$$

Where the scan cost is  $C_y$  and  $n$  is the total number of current scan points. When the wall is aligned to the x-axis of the Lidar's fixed frame, the cost function is terms of the y-coordinate  $P_y$ :

$$C_x = \sum (P_{y,i} - P_{y,mean})^2 / n$$

Since the cost function depends on the 3D data's x and y coordinate variations, the suitability is determined by solving for the partial derivatives of  $P_x$  and  $P_y$  with respect to  $D_{corr}$ ,  $\alpha$ , and  $\theta$ , which are desired to be optimized. Non-zero partial derivatives indicate the dependence of the cost function on the three calibration parameters. These partial derivatives with respect to  $D_{corr}$  are:

$$\frac{\partial P_x}{\partial D_{corr}} = \cos\theta \sin\beta$$

$$\frac{\partial P_y}{\partial D_{corr}} = \cos\theta \cos\beta$$

The partial derivative for  $\partial P_x / \partial D_{corr}$  is zero when  $\theta=90^\circ$  and  $\beta=0^\circ$ , which says a laser beam cannot scan a wall parallel to the laser. For the Lidar, the values for the laser beams are smaller than  $90^\circ$  and the scan does not necessarily take a value when  $\beta=0^\circ$  since the sensor is rotating and  $\beta$  changes. The same logic applies for the partial derivative for  $\partial P_y / \partial D_{corr}$ , which is zero when  $\theta=90^\circ$  and  $\beta=90^\circ$ . The resulting cost function using optimization for estimating  $D_{corr}$  can then be deemed suitable.

The partial derivative equations with respect to  $\theta$  are:

$$\frac{\partial P_x}{\partial \theta} = -D \sin\beta \sin\theta - V_{offset} \sin\beta \cos\theta$$

$$\frac{\partial P_y}{\partial \theta} = -D \cos\beta \sin\theta - V_{offset} \cos\beta \cos\theta$$

Where  $\beta=0^\circ$  for  $\partial P_x / \partial \theta$  and  $\beta=90^\circ$  for  $\partial P_y / \partial \theta$  make the partial derivatives equal to zero. These partial derivatives are non-zero since the Lidar constantly rotates. As a result, the cost function is suitable for using optimization in estimating  $\theta$ . The study did not, however, discuss the calibration of the third parameter,  $\alpha$ .



## Chapter 3: Theoretical Modeling



Figure 9 Velodyne HDL-32E Lidar and Setup Accessories



Figure 10:

Note: Each gyro incorporates a 2-axis accelerometer which results in redundancy in some axial directions.

Figure 10 Velodyne HDL-32E Lidar's Six-Axis Motion

Firing order	DSR #	Vertical angle
1	0	-30.67
2	1	-9.33
3	2	-29.33
4	3	-8.00
5	4	-28.00
6	5	-6.66
7	6	-26.66
8	7	-5.33
9	8	-25.33
10	9	-4.00
11	10	-24.00
12	11	-2.67
13	12	-22.67
14	13	-1.33
15	14	-21.33
16	15	0.00
17	16	-20.00
18	17	1.33
19	18	-18.67
20	19	2.67
21	20	-17.33
22	21	4.00
23	22	-16.00
24	23	5.33
25	24	-14.67
26	25	6.67
27	26	-13.33
28	27	8.00
29	28	-12.00
30	29	9.33
31	30	-10.67
32	31	10.67

Figure 11 Firing Order Sequence and Vertical Angle Position of Each Laser

### Mechanical Setup

The Velodyne HDL-32E 3D Lidar mechanical setup (Figure 9) consists of the Lidar, which has the dimensions of 5.68" x 3.36" dimensions and weighs 2.9 lbs, connected to an interface box. This interface box is powered by an AC Adapter with 12V at 2 Amps. The operating voltage range for the lidar is 9 to 32 VDC. The interface connects to a laptop with a 100 Mbps via an Ethernet cable. A Garmin GPS receiver allows for GPS time-synchronization. The Lidar's orientation is determined by internal MEMS accelerometers and gyros for six-axis motion (Figure 10) correction-external correction (Velodyne 2014).

### Sensor Specifications

#### Firing Sequence and IR Laser Angle Orientation:

The Velodyne HDL-32E Lidar has 32 lasers each positioned at a different angle to cover the 40 degree Field of View. Each laser is fired in an order sequence (Figure 11), which is the same for the Ethernet packet. The sequence operates by first firing the most downward laser, followed by an interwoven pattern of lasers between the downward and upper "banks" that contain 16 lasers each. Interleaving the laser firing avoids potential ghosting, which mainly originates from retro-reflectors (Velodyne 2014).

## CAD & Simulated Model

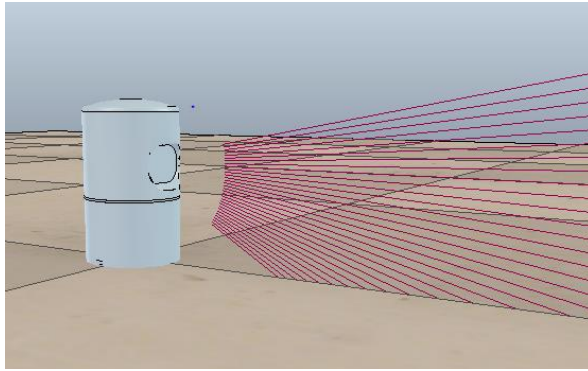


Figure 13 Model of Velodyne HDL-32E Lidar with 32 Lasers

mesh characteristics were adjusted, including absorption and emission. As shown in Figure 11, thirty-two lasers were individually created, aligned, and programmed as proximity sensors. In Figure 14, the wavelength of the “ray” light was set to infrared and the range of detection was set to a max of 70 m and internally programmed for a minimum detection of .5 m as determined from testing. The firing of the lasers originates from a point 3.575 inches from the base along the z-axis. The angular rotation of the Lidar is set as a user input variable, but has an optional hard-coded 900 RPM. To rotate the top part of the model, an internal revolution joint aligned along the Lidar’s z-axis was integrated.

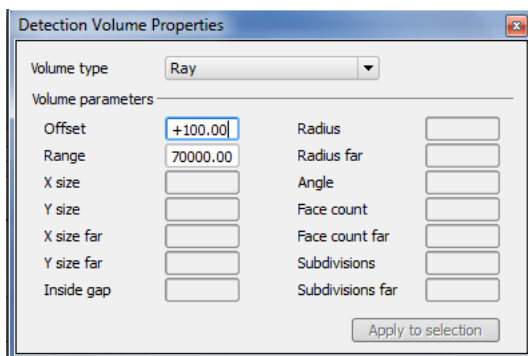


Figure 14 Main Proximity Sensor Definitions

Using CATIA, a CAD model (Figure 12) of the Velodyne HDL-32E was matched to the dimensions of the actual Lidar. After generating the CAD model, the file was converted into .stp format and transferred to 3DS max. Within 3DS max, the file was saved as .3DS, which is one of the formats readable by V-REP Pro to convert models into the simulation environment. Once converted into the simulation environment, the object properties can be accessed via a window (Figure 13) or manually coded. The surface

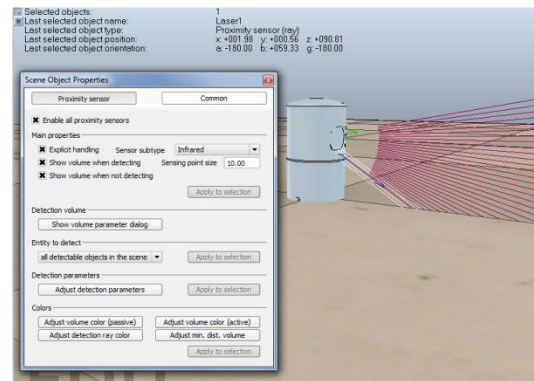


Figure 12 Basic Setup Before Calibration Coding

The Lidar visually reports the number of objects detected by all of its laser beams on the user display screen and records the distance, position, intensity, and time data via communication tubes within the code that can be read for navigational and obstacle detection use. The simulation model also has the option of visually displaying the point cloud generated by the laser beams as points, segments, or both.

## Error Model

### UDP Packet and Timing

Using the Packet offset table (in Appendix) relating the offset time in microseconds to each of the lasers 0-31, a formula for the actual laser firing timing can be developed. The timing can be determined by combining the packet timestamp, but it should be noted that the rotary encoder value is read at the beginning of packet creation which coincides with actual laser firing time and the timestamp is recorded and written at the end.

$$(1) \quad Timing = -542.592 + \left( \frac{Packet\ Offset}{100} * 46.08 \right) + (Dsr\# * 1.152)$$

Where Dsr# represents the Digital Sensor Recorder number, which is the number (0-31) for the laser fired (1-32) as it would be in the packet read in from the HDL-32E over the Ethernet (Velodyne 2014).

### Atmospheric Refraction

When traveling to an object and reflecting back to the sensor, a Lidar's laser beam moves through a media with variable refractive indices based on Snell's Law. The result of passing through the media is angular displacement of the beam.

#### Angular Displacement of Laser Beam

$$(2) \quad \Delta d = K \tan(\alpha)$$

Where  $\Delta d$  is the laser beam's angular displacement from theoretical path and  $\alpha$  is the laser beam's vertical angular placement. In defining K, a commonly used model provided by the Air Force is:

#### Air Research and Development Command (ARDC) Model

$$(3) \quad K = \left( \frac{2410H}{H^2 - 6H + 250} - \frac{2410h}{h^2 - 6h + 250} \left( \frac{h}{H} \right) \right)$$

Where H is the height of the sensor relative to the ground in kilometers, and h is the laser detected object's height in kilometers (NGA 2011).

The distance equation with atmospheric correction becomes:

#### Time of Flight Error Model

$$(4) \quad d_x = d_{x,i} + \Delta d$$

### Calibration Parameter Error Models

The Lidar's distance values are correctable using five calibration parameters that can be input into a calibration table. These five parameters are (Atanacio 2011):

Parameter 1:

- vertCorrection ( $\Phi$ )—elevation angle for each laser beam (positive rotates laser beam towards scanner's top)

Parameter 2:

- rotCorrection( $\theta$ )-Azimuth angle offset for each laser beam (offset from current rotation angle, positive rotates laser beam counter-clockwise)

Parameter 3:

- distCorection-Distance correction offset in centimeters, applied to time of flight distance by individual laser beam

Parameter 4:

- horixOffsetCorrection ( $h_{osc}$ )- A horizontal parallax correction orthogonal to laser beam

Parameter 5:

- vertOffsetCorrection ( $v_{osc}$ ) A vertical parallax correction orthogonal to laser beam

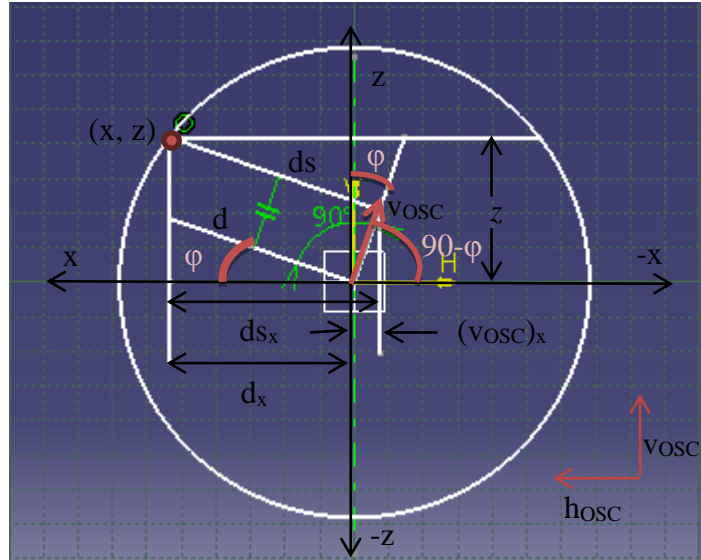


Figure 15 Velodyne Lidar's vertical elevation angle correction (Diagram made in CATIA)

Using the five parameter equations in relation to the original measured distance as shown in Figure 15 from the Velodyne HDL-32E Lidar, the 3-D coordinates can be derived. To begin, the vector equation for position analysis is:

$$(5) \quad d = ds - (v_{osc})$$

The magnitudes are then:

$$(6) \quad d_x = ds_x - (v_{osc})_x$$

$$(7) \quad d_x = d \cos(\phi) - v_{osc} \cos(90 - \phi)$$

Based on the parallel relationship:

$$(8) \quad ds||d \rightarrow v_{OSC} \cos(90 - \varphi) - v_{OSC} \sin(\varphi)$$

The plane's computed distance without considering rotation is:

$$(9) \quad d_x = d_s \cos(\varphi) - v_{OSC} \sin(\varphi)$$

Each point from the Velodyne scanner holds a 3D position defined as  $p=(x, y, z)$ . The rotation angle and horizontal offset can then be factored in as:

$$(10) \quad x = d_x \sin(\theta) - h_{OSC} \cos(\theta)$$

$$(11) \quad y = d_x \cos(\theta) + h_{OSC} \sin(\theta)$$

$$(12) \quad z = d_s \sin(\varphi) + v_{OSC} \cos(\varphi)$$

It can be said here that the mathematical model for each laser  $i$  therefore is a function of five intrinsic parameters (Atanacio 2011):

$$\{\Delta\theta_i, (h_{OSC}), (v_{OSC}), \Delta\varphi_i, \Delta d_{s_i}\}$$

Where  $\Delta\theta_i$  is the change in azimuth angle for each laser beam,  $h_{OSC}$  is the horizontal parallax correction orthogonal to the laser beam, and  $v_{OSC}$  is the vertical parallax correction orthogonal to the laser beam. The  $\Delta\varphi_i$  represents the change in elevation angle and  $\Delta d_{s_i}$  stands for the distance correction, which is the amount of distance offset.

### Depth Spread Error Model

Treating each laser as emitting an approximation of the Gaussian profile, each Gaussian Beam, or electromagnetic radiation beam with a Gaussian approximated transverse electric field and intensity, can be defined as:

$$(13) \quad E(r, z) = E_0 \left( \frac{w_0}{w(z)} \right) \exp \left( -\frac{r^2}{w(z)^2} - ikz - \frac{ikr^2}{2R(z)} + i\xi(z) \right)$$

Where  $r$  is the radial distance from the beam's center axis,  $z$  is the axial distance from the beam's narrowest point,  $i$  is the imaginary unit,  $k$  is the wave number ( $k=2\pi/\lambda$ ),  $E=|E(0,0)|$ ,  $w(z)$  is the radius at which field amplitude and intensity drop to  $1/e$  and  $1/e^2$  of axial values,  $w_0=w(0)$  waist size,  $R(z)$  is the radius of curvature of beam's wavefronts, and  $\xi$  is the Gouy phase shift based on Gaussian beams.

Time Averaged Intensity Distribution:

$$(14) \quad I(r, z) = \frac{|E(R, z)|^2}{2\eta} = I_0 \left( \frac{w_0}{w(z)} \right)^2 \exp \left( -\frac{2r^2}{w^2(z)} \right)$$

Beam Width:

For a beam of wavelength  $\lambda=905$  nm at a distance  $z=$  along the beam from beam waist, the variation of spot size is:

$$(15) \quad w(z) = w_0 \sqrt{1 + \left(\frac{z}{z_R}\right)^2}$$

Where  $z_R$  is the Rayleigh range. The Rayleigh range is the distance between the beam waist and the cross section area that is doubled, and can be represented by:

$$(16) \quad z_R = \pi * \frac{w_0^2}{\lambda}$$

The  $z$ -axis origin for  $w(z)$  coincides with the beam waist (Svelto 2010). The beam width criteria provided by Velodyne Lidar, however, states that the spot shape is a rectangular shaped spot 4" wide by 2" tall at 100' and 1/2" wide by 1/4" tall, causing angular divergence to be 2.79 milliradians. This indicates that the beam is not radially symmetric. Hermite-Gaussian modes would then be used for horizontal and vertical defined beams:

$$(17) \quad E_{nm}(x, y, z) = \frac{E_0 w_0}{w(z)} * H_n \left( \sqrt{2} * \frac{x}{w(z)} \right) \exp \left( -\frac{x^2}{w(z)^2} \right) * H_m \left( \frac{\sqrt{2}y}{w(z)} \right) \exp \left( -\frac{y^2}{w(z)^2} \right) \exp(-i[kz - (1 + n + m) \arctan \left( \frac{z}{z_R} \right) + \frac{k(x^2 + y^2)}{2R(z)}] \quad (\text{Paschotta 2014})$$

Where  $H_n(x)$  represent the Hermite polynomial for index  $n$ , which is a non-negative integer. Each of the indices  $n$  and  $m$  respectively define the profile's shape in the  $x$  and  $y$  direction. The terms  $w$  and  $R$  are along the  $z$ -axis. The value  $R$  represents the wavefront's radius of curvature evolved about  $z$  and is defined as:

$$(18) \quad R(z) = z \left[ 1 + \left( \frac{z_R}{z} \right)^2 \right] \quad (\text{Paschotta 2014})$$

## Error Correction

After culminating the error models for the Velodyne Lidar together, the methodology for correcting the errors begins. The following corrections presented consist of both physical and mathematical solutions.

For two-way electromagnetic interference, Halterman suggests that the effects on the GPS receivers can be physically mitigated by placing the antenna above the Lidar height. A filter can be used to negate RADAR interference in the Lidar data (Halterman 2010).

Correction of calibration errors for the Velodyne requires a series of individual tests covered in a general test plan located in the Appendix. After using horizontal and vertical correction factors, additional distance offset parameters can be obtained through comparison with SICK LMS-291 or LMS111 LIDAR (Figure 16) readings, which rely on a single rotating laser calibrated to zero angular elevation.

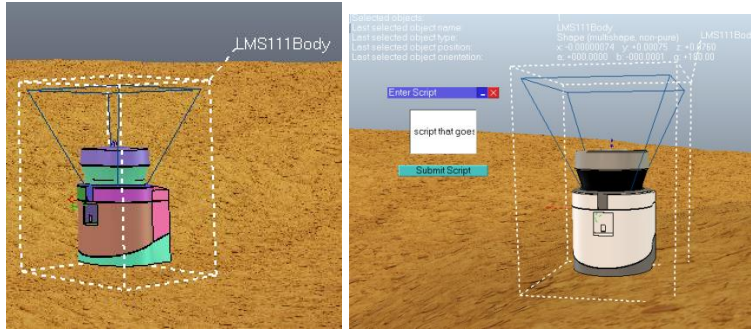


**Figure 16 V-REP Model of LMS 111 Lidar with Vision Sensor Feature and without Texture (Left) and with Texture (Right) on Ground Terrain. Lidar used for comparison in Lidar Alignment Method.**

An optional method is an optimization-based technique for multi-beam LIDAR calibration.

## Chapter 4: Test Data Results & Analysis

### Detection Range Results

#### Trial 1:

The first aspect to calibrating the Velodyne HDL-32E Lidar is to discern the distance correction parameter for each one of the lasers. To determine the accuracy and precision of the measurements for each laser, the distance measured by the Lidar is compared to the physically measured distance between a flat plane and the Lidar.

*Example Image for Trial 1 and Trial 2:*

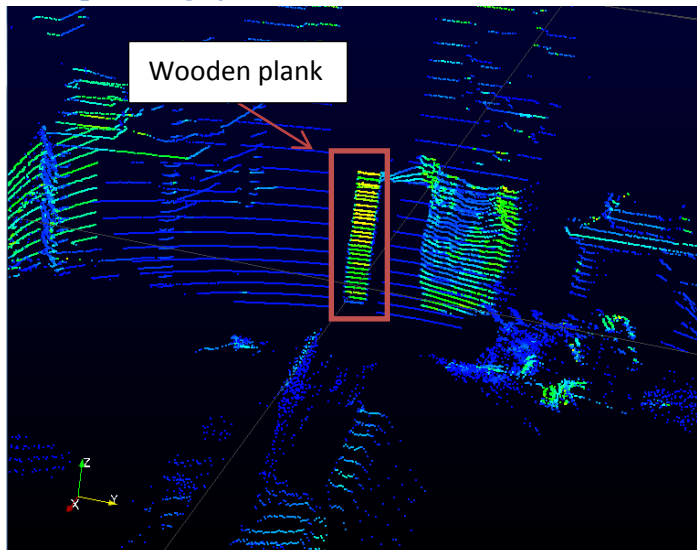


**Figure 17 Range Testing of Velodyne's Individual Lasers**



The purpose for the first trial test is to discern the measured distance variation of points along a returned scan line for a test object used for distance correction testing. The test object for this trial test is a pinewood panel with properties such as non-primed, untreated, straight grain, uniform textured, and a smooth surfaced. Based on comparing these properties to other types of wood and man-made material such as the tested aluminum plating (Figure 42), the selected pinewood returns the most consistent response in surface intensity and distance return values from the Velodyne Lidar. The setup (Figure 17) for the first test consisted of placing the Velodyne Lidar on a flat, elevated table in the lab. The horizontal, vertical, and height of the Lidar were recorded and marked. The beginning of the measuring tape was secured to the ground directly beneath the edge of the table and extended to the wall on the other side of the lab. The measuring tape designated by inches and feet was marked with tape on the floor to indicate a series of positions to be measured as incremental distances from the Lidar. The wooden panel stood vertically with one end flush with the floor and the front edge aligned with the marked point next to the first increment. After a period of time, the wooden panel is moved back to the next increment. The testing with the wooden panel finishes when it reaches the last increment, which was at the 23 ft. mark. A sample of points along the returned scan line is analyzed. The Velodyne's degree of accuracy is claimed to be <2cm (one sigma at 25 m) along with a vertical angular accuracy of 1.33 degrees. In contrast, the measuring tape is accurate to a degree of 1/32 inches, or 0.079375 cm. with setup time and series of measurement checks to ensure measurement reliability and repeatability, accounting for human error within the suggested measurement method would introduce a maximum of ¼ inch, or 0.635 cm, of error to the measured values, which is still less than 2 cm.

The Trial 1 Data Table consists of a sample of these measured data points along scanned lines at incremental distances. These points were selected along the vertical length of the plank from scanned lines assigned to different laser beam. The scanned lines used varied depending on the sample at a given distance, and represent the maximum, minimum, and in-between values of the range for distance values. Each sample of points was taken as a single measurement at a certain frame in time, which is indicated in the table, and each point can be referred to by using the Point Identification number as shown in Table 1. Each frame of data shows the cloud points in terms of their position and their intensity, which is represented by the color of the point. The color scale for intensities can be rescaled based on the maximum intensity measured among all the points. For Trial 1, the max intensity measured for a data point was 167 and the color range was rescaled accordingly.

Table 1- Trial 1 Data Table: Max Intensity-167

Dist. (ft)	Distance s (m)	Ti me	Measured Distances										Poin t 6	Point ID 6
			Poin t 1	Point ID 1	Poin t 2	Point ID 2	Poin t 3	Point ID 3	Poin t 4	Point ID 4	Poin t 5	Point ID 5		
1	0.518	284	0.5	24425	0.518	24233	0.518	24256	0.52	24280	0.518	24302	0.52	24322
2	0.822	782	0.848	24034	0.85	24063	0.848	24092	0.834	24088	0.828	24241	0.828	24270
3	1.127	1361	1.23	24419	1.232	24447	1.216	24171	1.232	24251	1.2	24203	1.218	24255
4	1.432	1522	1.436	24525	1.434	24253	1.434	24337	1.444	24220	1.436	24365	1.43	24333



5	1.737	1673	1.756	24340	1.76	24368	1.75	24280	1.748	24308	1.746	24297	1.76	24338
6	2.042	1928	2.038	24309	2.04	24369	2.048	24228	2.042	24224	2.042	24253	2.04	24282
7	2.346	2074	2.356	24227	2.356	24255	2.354	24339	2.45	24318	2.454	24232	2.456	24402
8	2.651	2155	2.65	24248	2.65	24271	2.648	24299	2.652	24383	2.654	24411	2.656	24327
9	2.956	2400	2.958	24314	2.962	24342	2.96	24482	2.954	24558	2.968	245660	2.974	24450
10	3.261	2530	3.28	24429	3.272	24457	3.76	24485	3.278	24569	3.266	24487	3.268	24543
11	3.566	2754	3.562	24501	3.59	24473	3.592	24445	3.578	24335	3.594	24339	3.586	24387
12	3.870	2908	3.862	24377	3.86	24489	3.862	24517	3.874	24348	3.876	24375	3.872	24327
13	4.175	3322	4.174	24432	4.176	24457	4.18	24485	4.182	24541	4.19	24597	4.18	24513
14	4.480	3477	4.488	24297	4.486	24352	4.484	24408	4.512	24293	4.51	24404	4.504	24458
15	4.785	3689	4.788	24328	4.78	24353	4.782	24381	4.784	24465	4.774	24493	4.796	24463
16	5.090	3908	5.102	24318	5.096	24344	5.084	24374	5.086	24430	5.088	24320	5.094	24400
17	5.394	4049	5.4	24289	5.392	24315	5.39	24343	5.38	24429	5.374	24317	5.408	24285
18	5.699	4179	5.688	24334	5.702	24332	5.7	24358	5.698	24414	5.71	24412	5.718	24356
19	6.004	4335	6.008	24438	6.022	24436	6.02	24464	6.012	24492	6.004	24520	6.006	24412
20	6.309	4482	6.286	24418	6.304	24416	6.306	24471	6.31	24414	6.308	24469	6.306	24471
21	6.614	4613	6.614	24404	6.618	24432	6.06	24346	6.62	24430	6.614	24404	6.61	24327
22	6.918	4786	6.91	24388	6.912	24416	6.924	24386	6.916	24414	6.918	24446	6.922	24470
23	7.223	5005	7.242	24471	7.224	24555	7.262	24443	7.25	24469	7.254	24525	7.23	24475

Once the samples of points are taken, the mean average for each set of data points can be calculated. The square of the difference between each point and the mean average is then determined. The sample standard deviation for each sample is calculated from these acquired squared differences, as shown in Table 2.

Table 2- Trial 1 Sample Standard Deviation Table Part 1:

Distances (ft)	Distances (m)	Time	Mean Average	Diff. 1	Diff. 2	Diff. 3	Diff. 4	Diff. 5	Diff. 6	Sample Standard Deviation (m)
1	0.518	284	0.52	2.45E-04	5.44E-06	5.44E-06	1.88E-05	5.44E-06	1.88E-05	0.008
2	0.822	782	0.84	7.51E-05	1.14E-04	7.51E-05	2.84E-05	1.28E-04	1.28E-04	0.010
3	1.127	1361	1.22	7.51E-05	1.14E-04	2.84E-05	1.14E-04	4.55E-04	1.11E-05	0.013
4	1.432	1522	1.44	1.11E-07	2.78E-06	2.78E-06	6.94E-05	1.11E-07	3.21E-05	0.005
5	1.737	1673	1.75	7.11E-06	4.44E-05	1.11E-05	2.84E-05	5.38E-05	4.44E-05	0.006
6	2.042	1928	2.04	1.34E-05	2.78E-06	4.01E-05	1.11E-07	1.11E-07	2.78E-06	0.003
7	2.346	2074	2.40	2.34E-03	2.34E-03	2.53E-03	2.09E-03	2.47E-03	2.67E-03	0.054
8	2.651	2155	2.65	2.78E-06	2.78E-06	1.34E-05	1.11E-07	5.44E-06	1.88E-05	0.003
9	2.956	2400	2.96	2.18E-05	4.44E-07	7.11E-06	7.51E-05	2.84E-05	1.28E-04	0.007
10	3.261	2530	3.35	5.48E-03	6.72E-03	1.65E-01	5.78E-03	7.74E-03	7.40E-03	0.199
11	3.566	2754	3.58	4.69E-04	4.01E-05	6.94E-05	3.21E-05	1.07E-04	5.44E-06	0.012
12	3.870	2908	3.87	3.21E-05	5.88E-05	3.21E-05	4.01E-05	6.94E-05	1.88E-05	0.007
13	4.175	3322	4.18	4.01E-05	1.88E-05	1.11E-07	2.78E-06	9.34E-05	1.11E-07	0.006
14	4.480	3477	4.16	1.05E-01	1.04E-01	1.02E-01	1.21E-01	1.20E-01	2.76E+00	0.813
15	4.785	3689	4.78	1.60E-05	1.60E-05	4.00E-06	0.00E+00	1.00E-04	1.44E-04	0.007
16	5.090	3908	5.09	1.07E-04	1.88E-05	5.88E-05	3.21E-05	1.34E-05	5.44E-06	0.007
17	5.394	4049	5.39	8.71E-05	1.78E-06	4.44E-07	1.14E-04	2.78E-04	3.00E-04	0.013
18	5.699	4179	5.70	2.15E-04	4.44E-07	7.11E-06	2.18E-05	5.38E-05	2.35E-04	0.010
19	6.004	4335	6.01	1.60E-05	1.00E-04	6.40E-05	7.89E-31	6.40E-05	3.60E-05	0.007
20	6.309	4482	5.30	9.66E-01	1.00E+00	1.01E+00	1.01E+00	3.98E+00	3.99E+00	1.546
21	6.614	4613	6.52	8.34E-03	9.09E-03	2.14E-01	9.47E-03	8.34E-03	7.63E-03	0.227
22	6.918	4786	6.92	4.90E-05	2.50E-05	4.90E-05	1.00E-06	1.00E-06	2.50E-05	0.005
23	7.223	5005	7.24	2.78E-06	3.87E-04	3.36E-04	4.01E-05	1.07E-04	1.87E-04	0.015

Then the number of deviations, or the distance factor, of each sample point from the sample standard deviation can be evaluated using the Table 3: Trial 1 Data Deviation from Sample Standard Deviation Table.

Table 3- Trial 1 Data Deviation from Sample Standard Deviation Table:

Sample Standard Deviation (m)	S1	S2	S3	S4	S5	S6
0.008	2.025	-0.302	-0.302	-0.560	-0.302	-0.560
0.010	-0.827	-1.018	-0.827	0.509	1.081	1.081
0.013	-0.686	-0.845	0.422	-0.845	1.689	0.264
0.005	-0.072	0.360	0.360	-1.799	-0.072	1.223
0.006	-0.433	-1.083	0.542	0.867	1.192	-1.083
0.003	1.064	0.484	-1.839	-0.097	-0.097	0.484
0.054	0.900	0.900	0.937	-0.850	-0.925	-0.962
0.003	0.566	0.566	1.246	-0.113	-0.793	-1.472
0.007	0.645	0.092	0.369	1.199	-0.738	-1.568
0.199	0.372	0.412	-2.040	0.382	0.442	0.432
0.012	1.801	-0.527	-0.693	0.471	-0.859	-0.194
0.007	0.799	1.081	0.799	-0.893	-1.175	-0.611
0.006	1.136	0.777	0.060	-0.299	-1.734	0.060
0.013	0.732	0.889	1.045	-1.150	-0.993	-0.523
0.007	-0.535	0.535	0.267	0.000	1.336	-1.604
0.007	-1.506	-0.632	1.118	0.826	0.534	-0.340
0.013	-0.747	-0.107	0.053	0.853	1.333	-1.387
0.010	1.420	0.065	0.258	0.452	-0.710	-1.485
0.007	0.535	-1.336	-1.069	0.000	1.069	0.802
0.009	1.985	-0.076	-0.305	-0.763	-0.534	-0.305
0.227	-0.403	-0.421	2.041	-0.429	-0.403	-0.385
0.005	1.278	0.913	-1.278	0.183	-0.183	-0.913
0.015	0.115	1.351	-1.260	-0.435	-0.710	0.939

### Trial 1 Analysis:

Based on the points gathered along the scan line, the distances measured by the Velodyne HDL-32E Lidar have a sample standard deviation ranging from  $\sigma=.003\text{m}$  to  $\sigma=.227\text{m}$ , demonstrating that the standard deviations increase and decrease as a function of distance. The data point deviations from the sample standard deviations range from  $-2.04\sigma$  to  $+2.041\sigma$ , depending on the sigma for the set of points at a measured distance. Another way to view these deviations is that the maximum deviation from a sample standard deviation is .463 m and the minimum deviation from a sample standard deviation is 0m. This range of sample standard deviations is fairly significant considering the points were taken from a flat surface positioned perpendicular to the Lidar's laser beams. The range of error most likely derives from offset parameters for one of the lasers needing adjustment. To analyze and minimize this fairly large range of sample standard

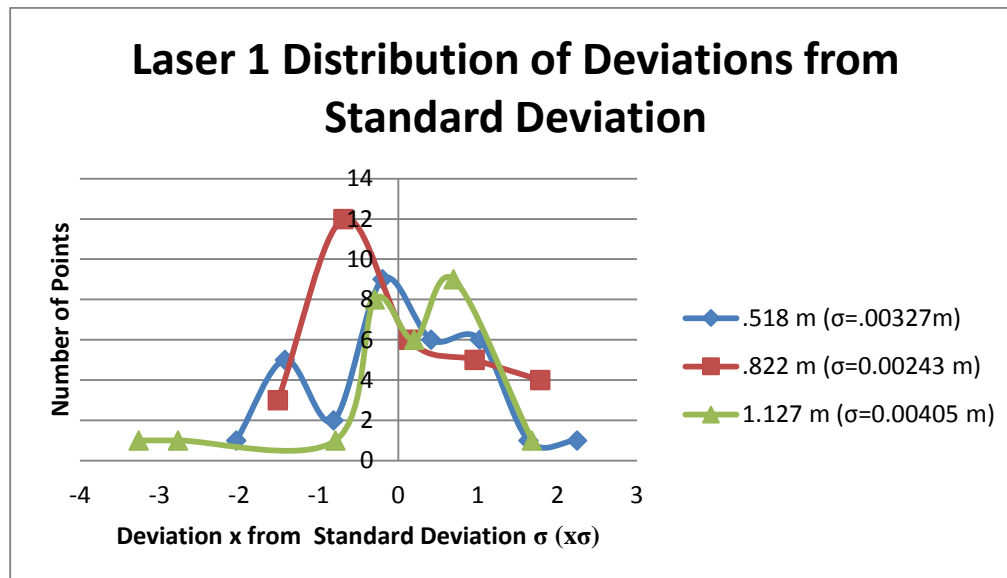
deviations and isolate why some points have a higher amount of deviation from these sample standard deviations, each of the lasers must be tested and corrected.

## Trial 2:

The purpose for the Trial 2 is to determine the maximum and minimum distance measured by each laser in the Velodyne HDL-32E of the wooden plank from the Lidar (Figure 17). From there the average, error, and deviation can be determined so as to generate a third-degree polynomial that takes a distance value from the Lidar and corrects it to the actual value. The setup of this test consisted of using the same wooden plank from the Trial 1 test and moving it back in increments from the laser. The points were then grouped based on laser ID. The minimum and maximum distance values of the wooden plank for each laser were recorded for each increment and the time frame was recorded as well for initial reference. To justify using the minimum and maximum values, the standard deviation and distribution of points from the standard deviation were analyzed for a few of the lasers, ensuring the minimum and maximum were not outlier points.

Table 4: Comparison of Minimum and Maximum Average with Multi-Point Average and Multi-Point Deviation for Laser 1

Position (#)	Distances (m)	Time (s)	Laser 1 min	Laser 1 max	Average	Points Used	Multi-Point Average	Standard Deviation $\sigma$ for Group Points (m)
1	0.518	1546	0.528	0.5424	0.535	31	0.535	0.00327
2	0.822	1730	0.836	0.842	0.839	30	0.838	0.00243
3	1.127	2159	1.132	1.152	1.142	27	1.145	0.00405

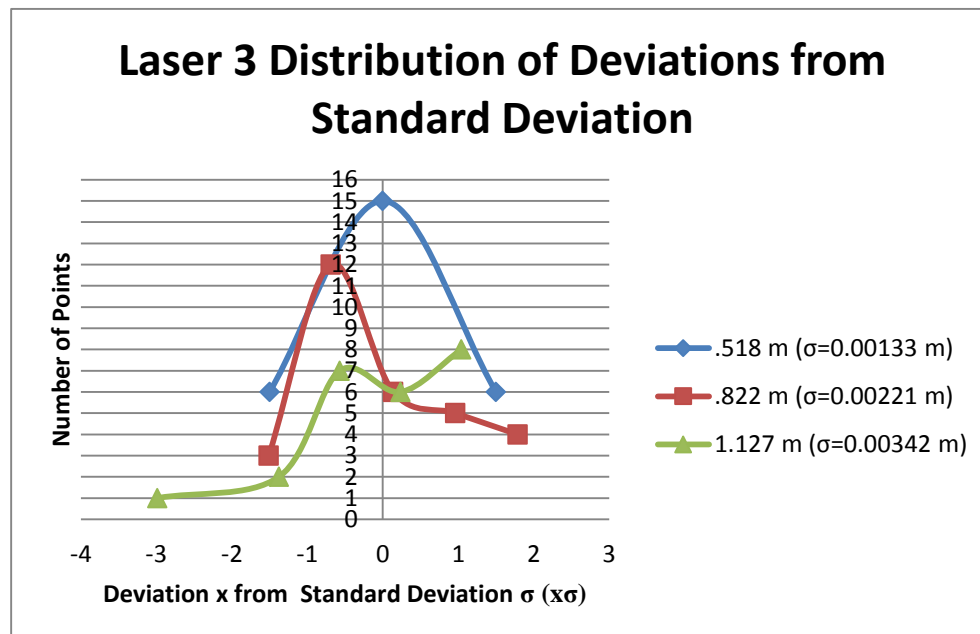


At incremental distances, the minimum and maximum value points are read from the wooden panel's Laser 1 line of points and compared to the entire group of points read from Laser 1's line on the wooden panel. The purpose is to determine whether the minimum and maximum read distances are outlier points compared to the group of Laser 1 points on the wooden panel at a

given distance. At time frame 1546 in the Velodyne data file, the average produce from the minimum and maximum value is .535 m, which is the same as the average .535 m produced from a group of 31 points along the laser line. The standard deviation for the points is  $\sigma=0.00327$  m. At frame 1730, the minimum and maximum distance values have an average distance of .839 m, which is .159 % more than the group average. The standard deviation for the group of points is  $\sigma=0.00243$ . For time frame 2159, the average from the minimum and maximum is 1.142 m, which is .278 % different from the group point average 1.145 m. The group standard deviation is  $\sigma=0.00405$  m. When observing the Laser 1's normal distribution of deviations from the standard deviation, the majority of points, including the maximum and minimum, are within  $2\sigma$ . For example,  $2\sigma$  for the .518 m deviation curve would be .00654 m.

Table 5: Comparison of Minimum and Maximum Average with Multi-Point Average and Multi-Point Deviation for Laser 3

Position (#)	Distances (m)	Time	Laser 3 min	Laser 3 max	Average (m)	Points Used	Multi-Point Average (m)	Standard Deviation $\sigma$ for Group Points (m)
1	0.517525	1546	0.538	0.546	0.542	27	0.538	0.00133
2	0.822325	1730	0.838	0.846	0.842	31	0.842	0.00221
3	1.127125	2159	1.146	1.15	1.148	26	1.147	0.00342

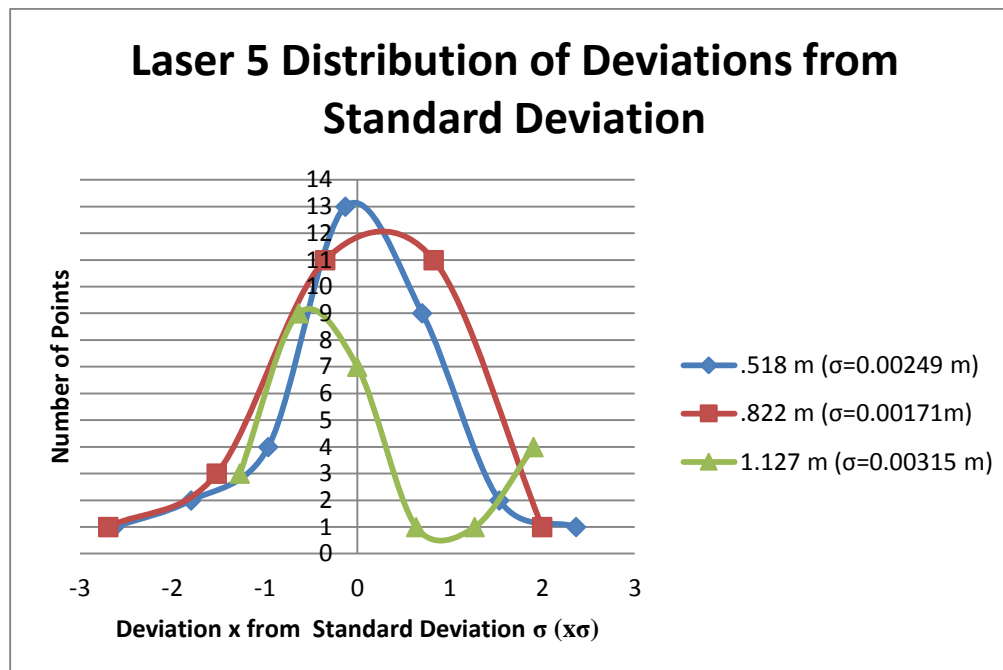


Points from Laser 3 are read and analyzed for the purpose of determining whether the minimum and maximum read distances are outlier points compared to the group of Laser 3 points on the wooden panel at a given distance. For frame 1546 in the Velodyne data file, the average produced from the minimum and maximum value is .542 m, which .743% different from the group average .538 m produced. The standard deviation for the points is  $\sigma=0.00133$  m. At time

frame 1730, the minimum and maximum distance values have an average distance of .842 m, which is .015 % more than the group average. The standard deviation for the group of points is  $\sigma=0.00221$ . At time frame 2159, the average from the minimum and maximum is 1.148 m, which is .051 % different from the group point average 1.147 m. The group standard deviation is  $\sigma=0.00342$  m. When observing the Laser 3 distribution of deviations from the standard deviation, the majority of points, including the maximum and minimum, are within  $2\sigma=0.00266$  m.

Table 6: Comparison of Minimum and Maximum Average with Multi-Point Average and Multi-Point Deviation for Laser 5

Position (#)	Distances (m)	Time	Laser 5 min	Laser 5 max	Average	Points Used	Multi-Point Average	Standard Deviation $\sigma$ for Group Points (m)
1	0.517525	1546	0.518	0.528	0.523	32	0.522	0.00240
2	0.822325	1730	0.822	0.934	0.878	27	0.827	0.00171
3	1.127125	2159	1.13	1.138	1.134	25	1.134	0.00315



Laser 5's minimum and maximum distance value points are sampled from the line of points associated with Laser 5 on the wooden panel. These minimum and maximum read distances are compared with the group of Laser 5 points to discern if the minimum distance and maximum distance are outlier points or if the average distance is close enough to the group average distance. In the Velodyne Laser 5 data at time frame 1546, the average of the minimum and maximum value is .523 m, which is .132% from .522 m produced from a group of 32 points along the laser line. The standard deviation for the points is  $\sigma=0.00240$  m. For the time frame 1730, the minimum and maximum distance values have an average distance of .878 m, which is

6.22 % more than the group average. The standard deviation for the group of points is  $\sigma=0.00243$ . For time frame 2159, the average from the minimum and maximum is 1.142 m, which is .278 % different from the group point average 1.145 m. The group standard deviation is  $\sigma=0.00171$  m. In the Laser 5 distribution of deviations from the standard deviation, the majority of points, including the maximum and minimum, are within  $3\sigma$ . For example,  $3\sigma$  for the .518 m deviation curve would be .0072 m.

Overall, the point deviations that include the maximum and minimum values are fairly close, with a majority of them within  $\pm 2\sigma$  or  $\pm 2.7\sigma$ . While  $2.7\sigma$  is outside the usually desired  $2\sigma$ , the actual value represents a maximum of .01 m variation, which is considered for this study to be a relatively small enough distance from the mean. Therefore, the maximum and minimum values are not outliers and can be used to determine the averages used for creating correction equations. The Trial 2 Data Sample table serves as an example of the entire table located in the Appendix.

Table 7-Trial 2 Section of Data Table for Laser 1 (Table for Lasers 1-32 in Appendix):

Distances (ft)	Distances (m)	Time	Laser 1 min	Laser 1 max
1	0.518	1546	0.528	0.542
2	0.822	1730	0.836	0.842
3	1.127	2159	1.132	1.152
4	1.432	2265	1.466	1.472

The data in the Trial 2 Data Table Sample shows that at time frame 1546 the wooden plank is at a distance of .52 meters. The minimum distance measurement read by Laser 1 is 0.5280 meters and the maximum data point value returned .5424 m. The next step is to take the average of the maximum and minimum distance values for each laser as shown in Table 8.

Table 8- Laser 1 Example from Average Distance for 32 Lasers Data Table (See Appendix):

Distances (ft)	Distances (m)	L1 (m)
1	0.518	0.535
2	0.822	0.839
3	1.127	1.142
4	1.432	1.469

With the wooden panel's average distance measured by laser determined, the difference between the average sensor measured distance and the physical measured distance is calculated in Table 9. From there the error can be determined as well for each laser's output of time of flight calculated data.

Table 9- Laser 1 Example from Error for 32 Lasers Data Table (See Appendix for Entire Table):

Distances (ft)	Distances (m)	L1 (m)
1	0.518	0.0177
2	0.822	0.0167
3	1.127	0.0149
4	1.432	0.0371

The average distance error calculated from the table shows a variance of a 0.0127 m to 0.8128 m depending on the laser and the distance of the wooden panel from the Velodyne HDL-32E laser. Laser 8 in particular had bad error as distance increased, with its maximum error being 0.8128 m.

The distance error correction formula is generated by taking the span of Velodyne distance values as inputs for the function and generating a third-degree polynomial trend line. The resultant values as outputs of the function should closely match the physically measured distance.

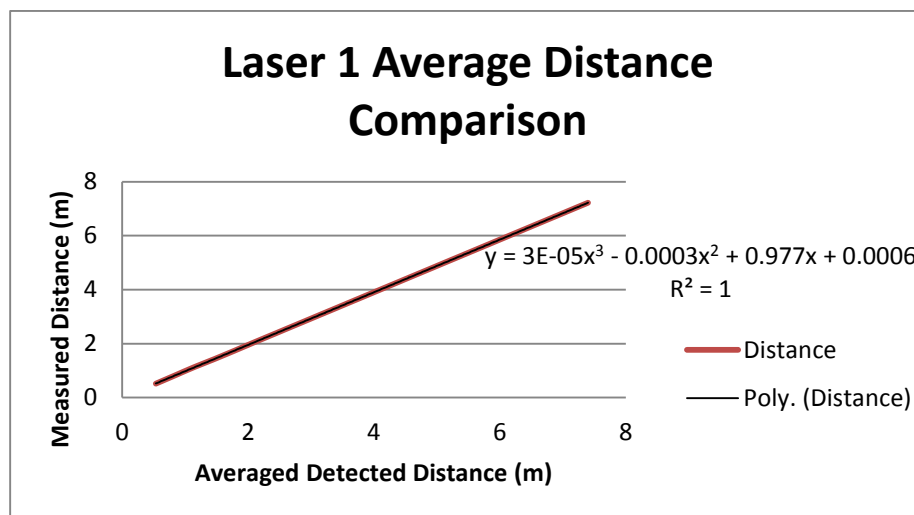


Figure 18 Laser 1 Comparison of Average Detected Distance and Measured Distance to generate Correction Equation for Laser 1

For example, using the corrective equation for Laser 1 of the Velodyne HDL-32E,

$$y = 3E-05x^3 - 0.0003x^2 + 0.977x + 0.0006$$

generates the corrected values listed in the

Table 10- Corrected Laser Table:

Distances (ft)	Distances (m)	L1	Corrected L1	Uncorrected Error (%)	Corrected Error (%)
1	0.518	0.535	0.523	3.42	1.14
2	0.822	0.839	0.820	2.03	0.27
3	1.127	1.142	1.116	1.32	0.99

Distances (ft)	Distances (m)	L1	Corrected L1	Uncorrected Error (%)	Corrected Error (%)
4	1.432	1.469	1.435	2.59	0.23
5	1.737	1.782	1.741	2.61	0.24
6	2.042	2.091	2.042	2.40	0.02
7	2.346	2.403	2.347	2.41	0.02
8	2.651	2.715	2.652	2.42	0.02
9	2.956	3.028	2.957	2.42	0.02
10	3.261	3.340	3.262	2.43	0.02
11	3.566	3.652	3.566	2.43	0.02
12	3.870	3.965	3.871	2.44	0.02
13	4.175	4.277	4.176	2.44	0.02
14	4.480	4.589	4.481	2.44	0.02
15	4.785	4.902	4.786	2.45	0.03
16	5.090	5.214	5.091	2.45	0.03
17	5.394	5.526	5.396	2.45	0.03
18	5.699	5.839	5.701	2.45	0.03
19	6.004	6.151	6.006	2.45	0.03
20	6.309	6.464	6.311	2.45	0.04
21	6.614	6.776	6.616	2.46	0.04
22	6.918	7.088	6.921	2.46	0.05
23	7.223	7.401	7.227	2.46	0.05

The error between the corrected values and the actual distance values ranges from .02%-1.14%, which is reduced from the uncorrected error ranging from 1.32% to 3.42%. The close range has the largest corrected error because the correction curves used for distance correction do not fit as well to the minimum boundary limit of the Lidar's detection, where there is a greater amount of initial error in measurements.

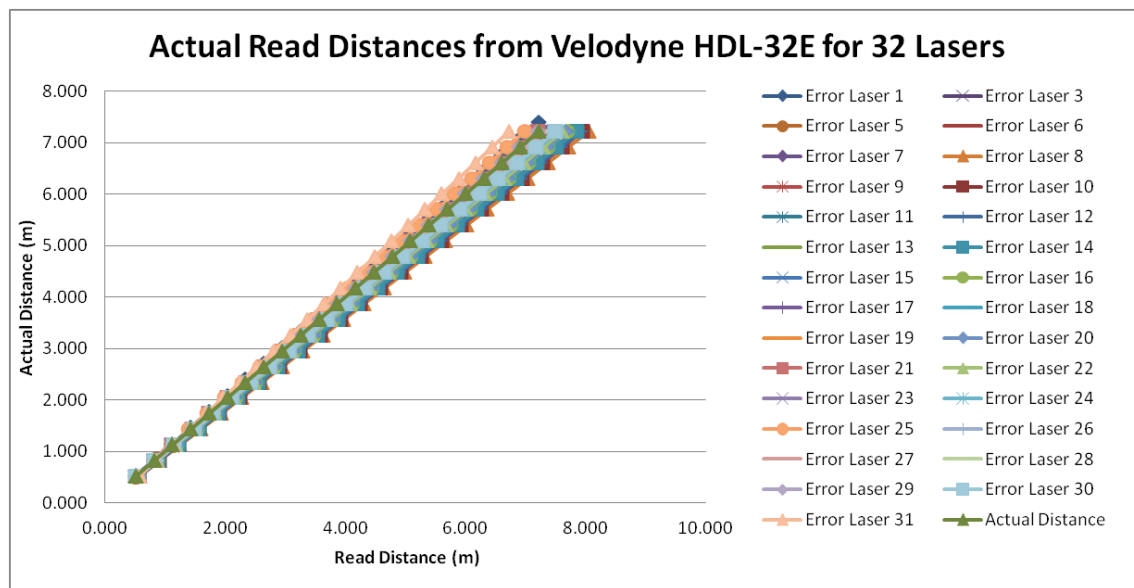


Figure 19 Comparison of Actual Distance to Error Distances Read for Each of 32 Lasers



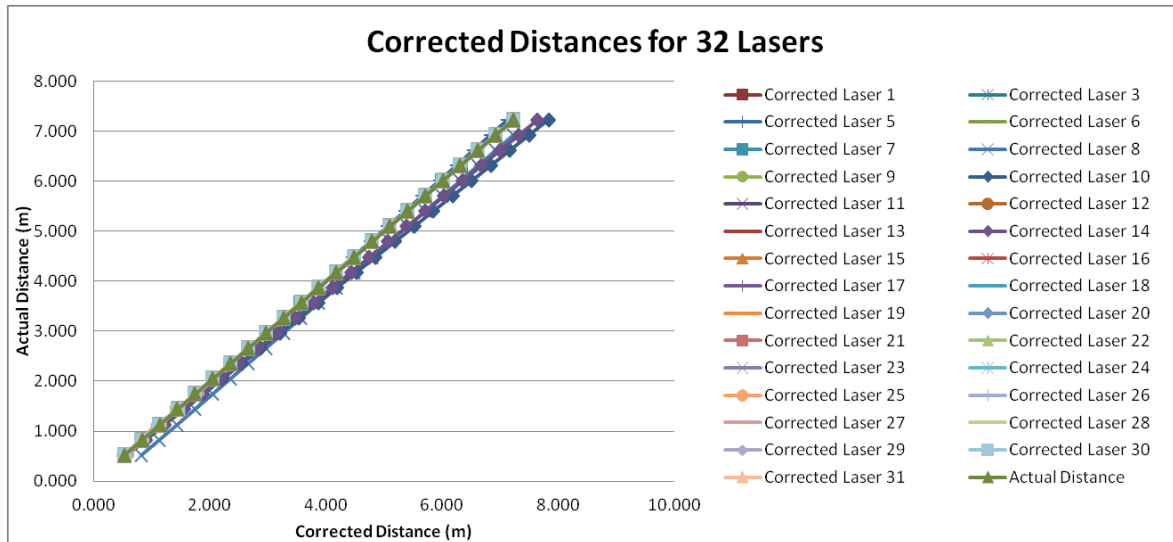


Figure 20 Comparison of Actual Distance to Corrected Distances Read for Each of 32 Lasers

Figure 19 shows the variation of distances recorded for each of the Velodyne's 32 lasers and how much each deviates from the actual distance. Figure 20 displays the reduced error for each laser's corrected distance from the actual distance. While there may appear to be two distinct groups of data in Figure 20, the corrected data pattern is not correlated to any aspect of the sensor, especially not the lasers grouped into upper and lower banks. To check for consistency, the corrective equations were also used on multiple time frames of data.

### Field of View Results:

The purpose of this next test is to discern the Velodyne HDL-32E's vertical field of view. According to the manual, the Velodyne field of view ranges from +10.67 to -30.67 degrees. The Field of View test is setup so that the entire vertical range within an area of the horizontal field of view is covered. A flat white wall for optimal return is used to capture all of the Lidar's lasers, which are each positioned at a different angle along this vertical field of view. The data points of this wall's position are measured by the Lidar and recorded by the program VeloView. Then points from the top and bottom edges of the wall are taken and the distance between them is measured. Using trigonometry of the Lidar's measured position relative to these points, the angular difference between these two edges is determined. This angular difference serves as the field of view for the Velodyne HDL-32E Lidar.

### Example Image:

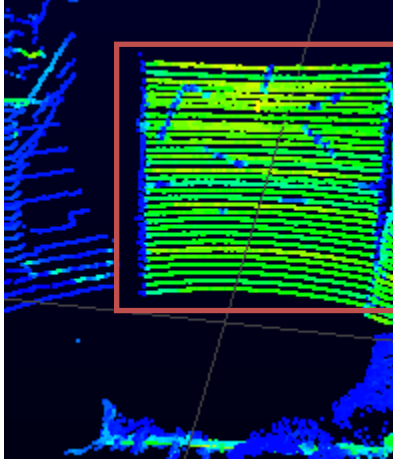


Figure 22 Field of View Detection Wall  
Covering Entire Velodyne Angular Range

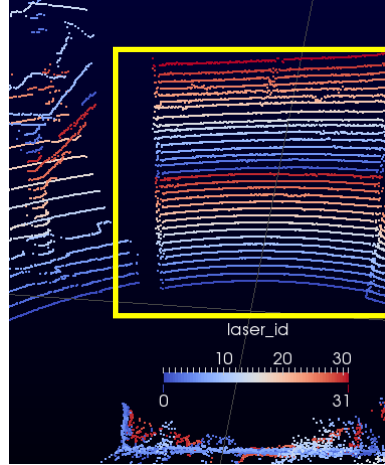


Figure 21 Field of View Detection with Laser ID Scale

Table 11: Single Data Measurement for Field of View

Field of View					
X (m)	Y (m)	Z (m)	Azimuth	ID	Time Frame
-1.25789	-0.0992192	0.237735	26549	31560	2418
-1.25688	-0.137429	-0.749836	26376	31209	2418
	Measured (°)	Theoretical (°)	Difference (°)		
Angle 1 (degrees)	10.70	10.67	.03		
Angle 2 (degrees)	-30.82	-30.67	.15		
Total FOV (degrees)	41.52	41.34	.18		

In Table 11, Angle 1 represents the positive vertical span of the Lidar's field of view beginning from 0 degrees along the z-axis. The theoretical Angle 1 for the Velodyne HDL-32E Lidar is .03 degrees less than the measured Angle 1. Angle 2 represents the negative vertical span below 0 degrees along the z-axis. The theoretical Angle 2 is .15 degrees smaller in range than the measured span of the field of view on the negative part of the vertical axis.

Table 12: Example of Data Coordinates Used for Each Laser to Calculate Laser Angle

Laser #	x <sub>1</sub> (m)	y <sub>1</sub> (m)	z <sub>1</sub> (m)	x <sub>2</sub> (m)	y <sub>2</sub> (m)	z <sub>2</sub> (m)	x <sub>3</sub> (m)	y <sub>3</sub> (m)	z <sub>3</sub> (m)
0	-1.25559	-0.14883	-0.74984	-1.2651	-0.12494	-0.75392	-1.26545	-0.1214	-0.75392
1	-1.29122	-0.17137	-0.214	-1.29172	-0.16754	-0.214	-1.29615	-0.16397	-0.21465
2	-1.26009	-0.12089	-0.71125	-1.25701	-0.11639	-0.70929	-1.26084	-0.11275	-0.71125
3	-1.31294	-0.17822	-0.18621	-1.30364	-0.17302	-0.18482	-1.30219	-0.16889	-0.18454

In Table 12, a sample of points with 3-D coordinates (x, y, and z) is presented for each laser to determine the laser's angular position. The entire table, which Table 12 is extracted from, consists of all 32 lasers, their sample of points, and the calculated angular position. Table 13 shows the theoretical point compared

with each angular position calculated from a trial point (Sample Angle 1, Sample Angle 2, and Sample Angle 3) associated with a 3-D coordinate ( $x_i$ ,  $y_i$ , and  $z_i$ ).

Table 13- Field of View Data Table

Laser #	Theoretical Angular Position	Sample Angle 1	Sample Angle 2	Sample Angle 3	Average Angle
0	-30.67	-30.67	-30.67	-30.67	-30.67
1	-9.33	-9.33	-9.33	-9.33	-9.33
2	-29.33	-29.33	-29.33	-29.33	-29.33
3	-8	-8.00	-8.00	-8.00	-8.00
4	-28	-28.00	-28.00	-28.00	-28.00
5	-6.67	-6.67	-6.67	-6.67	-6.67
6	-26.67	-26.67	-26.67	-26.67	-26.67
7	-5.33	-5.33	-5.33	-5.33	-5.33
8	-25.33	-25.33	-25.33	-25.33	-25.33
9	-4	-4.00	-4.00	-4.00	-4.00
10	-24	-24.00	-24.00	-24.00	-24.00
11	-2.67	-2.67	-2.67	-2.67	-2.67
12	-22.67	-22.67	-22.67	-22.67	-22.67
13	-1.33	-1.33	-1.33	-1.33	-1.33
14	-21.33	-21.33	-21.33	-21.33	-21.33
15	0	0.00	0.00	0.00	0.00
16	-20	-20.00	-20.00	-20.00	-20.00
17	1.33	1.33	1.33	1.33	1.33
18	-18.67	-18.67	-18.67	-18.67	-18.67
19	2.67	2.67	2.67	2.67	2.67
20	-17.33	-17.33	-17.33	-17.33	-17.33
21	4	4.00	4.00	4.00	4.00
22	-16	-16.00	-16.00	-16.00	-16.00
23	5.33	5.33	5.33	5.33	5.33
24	-14.67	-14.67	-14.67	-14.67	-14.67
25	6.67	6.67	6.67	6.67	6.67
26	-13.33	-13.33	-13.33	-13.33	-13.33
27	8	8.00	8.00	8.00	8.00
28	-12	-12.00	-12.00	-12.00	-12.00
29	9.33	9.33	9.33	9.33	9.33
30	-10.67	-10.67	-10.67	-10.67	-10.67
31	10.67	10.67	10.67	10.67	10.67

### Analysis:

The Velodyne HDL-32E Lidar claims to have a 360 degree horizontal FOV with a +10.67 to -30.67 degree (total of 41.34 degree) vertical FOV. When using a wall to cover the Lidar's entire vertical field of view, an initial measured angular distance between the lowest detected point and

the highest detected point was 41.52 degrees in Table 11. The difference between the theoretical value and the measured value is .43% error, which is insignificant. When taking a greater sample of points for each laser, the measured angular distance was 41.34 degrees and the average angular distance was 41.34 degrees. In relation to the simulation setup, the initial field of view error indicates the total vertical range of the lasers is slightly wider than 41.34 degrees. Since the average FOV is the same as the claimed FOV, the error between the theoretical and measured FOV is insignificant, and the Velodyne's rounded claim of 40 degrees for FOV was for significant figures purposes while claiming a 1.33 degree variation in angular accuracy, the simulation lasers do not need to be adjusted.

## Buoy Analysis:

### Buoy Geometrical Features:



Figure 24 Typical Features of a Red Channel Marker



Figure 23 Typical Features of a Green Channel Marker

Typical geometrical features for a red buoy (Figure 23) that will help with profiling and identification are the triangular/cone based shape at the top of the buoy, the thick parabolic shape of a red retroreflector, and the bottom edge at the bottom of the buoy. The green buoy (Figure 24) is identified by a rectangular tube shaped profile, the parabolic shape of a green retroreflector, and the edge. Each one of these aspects will affect the overall intensity profile return for each buoy type. The intensity profile also depends on the material type the buoy consists of and the material's surface properties.

## Material Analysis:

Modeling buoys requires understanding which materials are used and the associated properties. The following list provides background information on the various types of materials and material properties associated with various buoys used in the maritime environment. Specialized buoys such as the A-1 buoys and Taylor Series buoys do not publicly report their chemical formula, but have similar properties to some of these materials. As a result, the buoys are tested in this thesis for further understanding of surface properties such as intensity return.

### *Polyethylene*

Polyethylene is a common thermoplastic consisting usually of  $(C_2H_4)_nH_2$ . PE varies in organic compounds based on the n value. The material typically has excellent chemical resistance. Polyethylene is categorized into different variations based on density and branching, which also affect the mechanical properties.

The refractive index for a green (520-570 nm) polyethylene buoy should be 1.502-1.506. The refractive index for a red (630-655 nm) polyethylene buoy should be 1.499-1.500 (Filmetrics 2014).

### *Acrylonitrile Butadiene Styrene (ABS)*

Acrylonitrile Butadiene Styrene (ABS) is a common, amorphous thermoplastic known as a terpolymer. ABS proportions vary from 15 to 35% acrylonitrile, 5 to 30% butadiene and 40 to 60% styrene. The styrene gives ABS its characteristic shiny, impervious surface. The polybutadiene allows ABS to have resilience at low temperatures while the nitrile makes ABS strong than pure polystyrene. Overall, ABS is considered a superior plastic for its hardness, gloss, impact resistance, toughness, and electrical insulation. ABS is also damaged by sunlight (Dynalab Corp. Inc. 2013).

### *LLDPE*

Linear low-density polyethylene has a density range of 0.915-0.925 g/cm<sup>3</sup>. LLDPE has a higher tensile strength than low-density polyethylene (LDPE), which has a density range of 0.910-0.940 g/cm<sup>3</sup>. LLDPE is also characterized by higher impact and puncture resistance compared with LDPE. The typical refractive index of LDPE is 1.51 with a 4-50% transmittance (San Diego Plastics 2014).

### *HDPE*

High-density polyethylene (HDPE) has a density in the area of 0.941 g/cm<sup>3</sup>. HDPE's low degree of branching indicates low intermolecular forces and tensile strength, which is still four times greater than low density polyethylene. HDPE is resistant to moisture and water, including saltwater. The typical refractive index is 1.53 at 589 nm to 1.54 with a 10-50% transmittance (San Diego Plastics 2014).

### *Retroreflectors*

Retroreflectors are surfaces that reflect light with minimum scattering back to the light's source. This returning light is a parallel but opposite vector of an electromagnetic wave front. As a result, the angle of incidence for this surface reflection is greater than zero. The coefficient of luminous intensity,  $R_I$ , represents a quantitative measurement of reflector performance. This performance is the ratio of the reflected light's strength (luminous intensity) to the amount of light falling on the reflector (normal illuminance). The  $R_I$  value is directly proportional to the reflector's brightness.  $R_I$  depends on color, size, and condition of the reflector. Clear or white

reflectors are the most efficient reflectors and will appear brightest. The  $R_I$  value also depends on spatial geometry relating the observer, the light source, and the retroreflector. The brightness of the reflector is inversely proportional to the distance between the reflector and the light source, meaning the brightness increases as the distance between the light source and reflector decreases since more light is returning to the observer based on the observation angle (U.S. Consumer 1996).

### Reflectivity Profile Results:

The tests for reflectivity were set up in a dark room with a lamp and a VEX light sensor 276-2158 connected to an Arduino Uno. The analog VEX light sensor uses a 0V to 5V range that outputs from 0 to 255, with a low value representing a bright light and a high value indicating a low light. The smaller the illumination value indicates a greater amount of light received by the light sensor (VEX 2014). Each material was positioned directly in front of the light sensor. The light angled normal to the material surface so the entire material surface is illuminated. The range of illumination values were then recorded for comparison and averaged as seen in the Material Reflectivity Table. The PVC Pipe White and PVC Pipe Red ranges are included because of the significantly greater range of values returned compared to the other materials. The PVC range of values results from degree of curved surface on a small area compared to the less curved surface of the yellow buoy and flat surfaces of the other materials that return fairly consistent amounts of light because of the uniform surface. Retroreflectors of two different shapes were used to normalize the data for more accurate comparison of the illumination ranges with each other and the intensity values from the Lidar.

Table 14:- Material Illumination Data Table:

Material	Measured Illumination
Kiln Dried Pine	33
Yellow Buoy	58
PVC Pipe White	9-61 (Range)
PVC Pipe Red	58-119
Aluminum	68
Polycarbonate	103
Light	20
No Light	690
Back light	589

Table 15:- Retroreflector Data for Normalizing:

Reflectors	Measured Illumination
Large Red	35-42
Little Green	63-65
Little Blue	45-48
Little White/Clear	29-36
Little Red	47-57
Little Orange	37-45

The return values of the retroreflectors are dependent on area and color, so a 3 3/16" diameter ("Large"), red retroreflector and a 1.25" diameter ("Little"), red retroreflector were both used to compare that dependency. The Large Red reflector had a measured reflectivity of 35-42 whereas the little red reflector had a measured reflectivity of 47-57. The difference between their highest illumination values, 35 and 47 respectively, is 12, which is about a 35% increase in illumination value, but also a decrease in amount of light received. While this may seem counterintuitive, the

VEX light sensor sets up the relationship between illumination value and amount of measured light inversely, as previously mentioned.

### Retroreflectors Data Table

A test with retroreflectors is required to compare the intensity profile responses of material surfaces to the intensity response from the known high-reflective surface of retroreflectors. The test setup consists of a Lidar mounted at one end of a table within the lab, a measuring tape extending from one end of the table to the other end of the table, and marked incremental distances from the front of the Lidar for where each retroreflector will be moved to for intensity measurements.

#### Example Images of Retroreflectors detected by Velodyne HDL-32E Lidar:

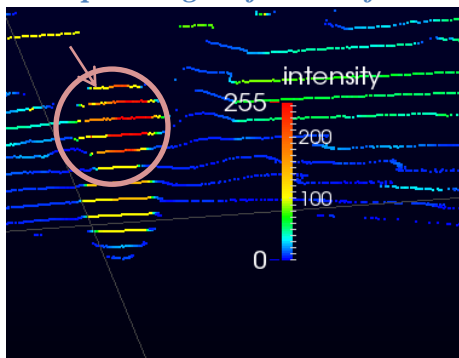


Figure 25 3 3/16" Red Reflector (Circled)

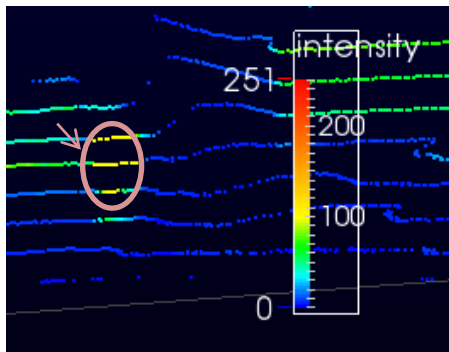


Figure 26 1.25" Green Reflector (Circled)

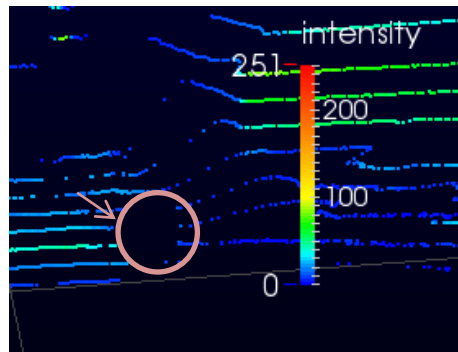


Figure 27 1.25" Green Reflector (Circled) at .4622 m, which is closer than Velodyne HDL-32E's .5 m detection

Table 16- Intensity Range Retroreflector Data Table:

Distances (m)	Reflector Intensities					
	3 3/16" Red Intensity	1.25" Green Intensity	1.25" Blue Intensity	1.25" White/Clear Intensity	1.25" Red Intensity	1.25" Orange Intensity
0.7416	6-255 (whole); 100-255 (Core 51 pts)	100	100-163	100-163	63-172	100-165
0.6146	5-255; 100-255 (51 pts.)	20-100	100-185	100-185	63-178	100-185
0.4622			3-30			

Distances (m)	Reflector Intensities					
	3 3/16" Red Intensity	1.25" Green Intensity	1.25" Blue Intensity	1.25" White/Clear Intensity	1.25" Red Intensity	1.25" Orange Intensity
0.894	4-251; 100-248 (35 pts)	24-100	97-100	100-155	45-185	100
1.1226	13-251; 100- 251 (22 pts)	73-100	100	100	100-166	100-162
1.4274	4-251; 100-251 (20 pts)	50-100	91-100	100	100	95-100

As shown within the Intensity Range Retroreflector Data Table, the returned intensity values read by the Lidar increase as the distance between the retroreflectors and the Lidar decrease. The large red retroreflector returns the highest intensity because of its greater surface area. Also, as a result of area of properties, the range of values the larger red retroreflector returns also most closely resemble those expected from reflector tape on a red buoy. The lower intensity return values by the green retroreflector with a max of 100 would more closely resemble green reflector tape for the green buoy. With a greater green reflector tape area, the percentage difference based on area between the small red retroreflector and the larger red retroreflector can be applied.

To gain a better grasp on the intensity properties for the base retroreflectors used for comparison, a series of graphs showing the intensity distribution for detected points of the object are presented. The intensity distribution graphs also show the varying distribution at different distances.

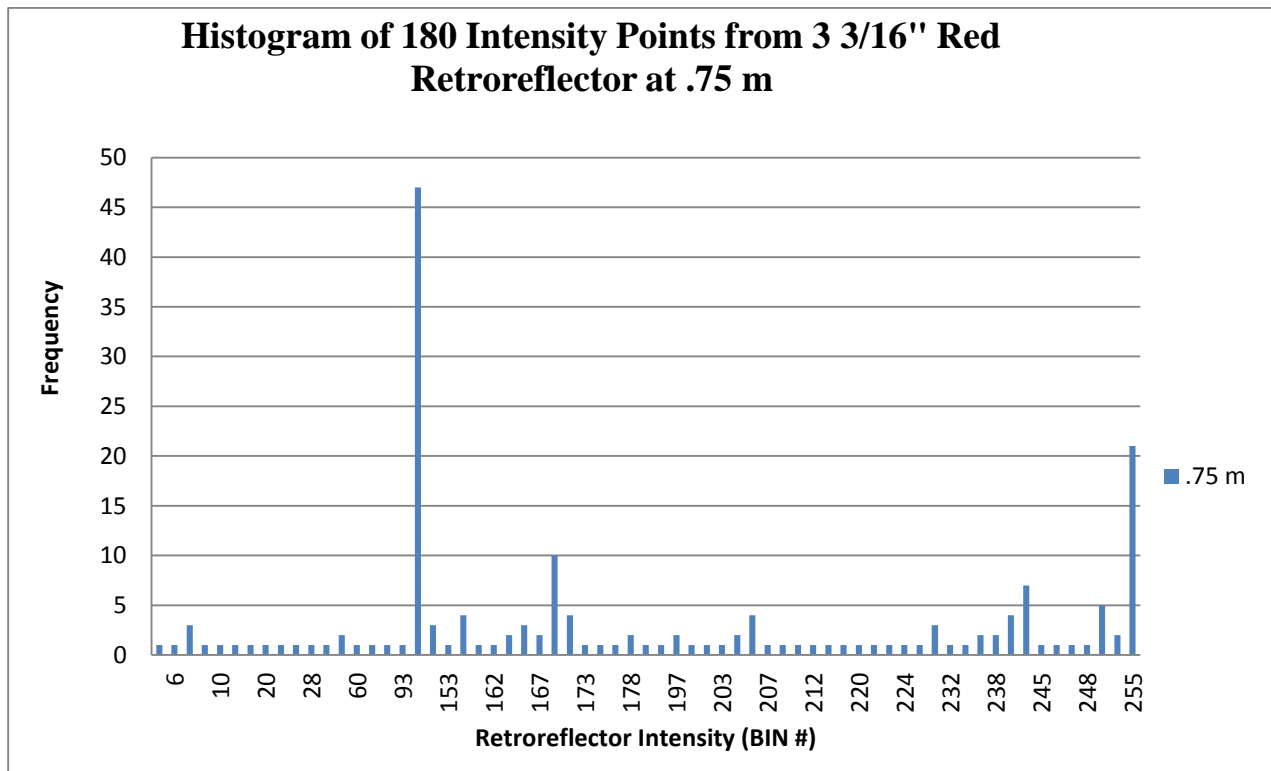


Figure 28 Measured Number of Occurrences Distribution for 180 Intensity Points on a scale of 0-255 returned from the Velodyne HDL-32E Lidar, which detects the Large Red Retroreflector at a distance of .75 m.



The intensity distribution in Figure 28 describes the distribution of 180 intensity points numbered 1-180 that make up the 3 3/16" Red Retroreflector positioned .75 m from the Velodyne HDL-32E Lidar. The Red Retroreflector's 180 points are read by the Velodyne and graphed to show that for a span of 180 points, the range of intensities decreased on a negative slope from 250 to 4 in value, with a small plateau at 250 with 21 points and another at 100 with 46 points (Figure 28). Figure 28 shows that the 3 3/16" Red Retroreflector will return 100 overall with noise around it. Part of the noise comes from minimum scattering that can occur from when light hits the cubes that cover the reflector surface to return parallel light, as shown in Figure 29.

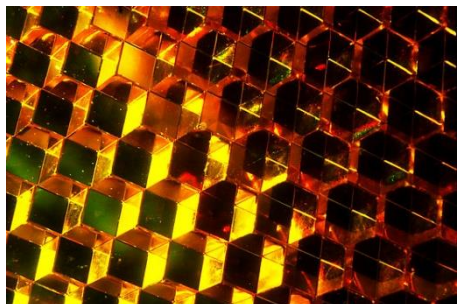


Figure 29 Surface of an Orange Retroreflector that shows small cubes used to return Parallel Light(Greenwald 2014)

Further analysis of the light distribution and minimum scattering from Figure 28 is shown in Figure 30, which displays the intensity deviation distribution from the standard deviation of intensity for the 3 3/16" Red Retroreflector.

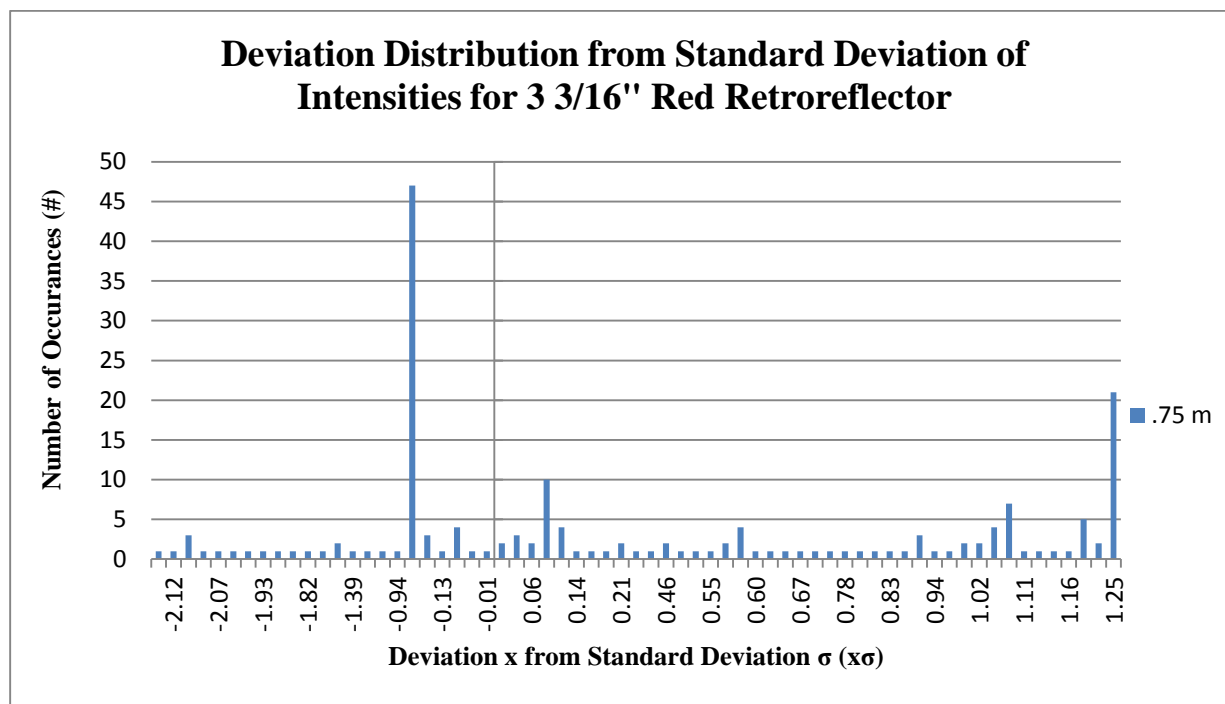


Figure 30 Deviation of Each Measured Intensity Value from the Calculated Standard Deviation from the Average Intensity for the 3 3/16" Red Retroreflector, where  $\sigma=74$ .

Figure 30 shows the range of deviations to be  $-.16\sigma$  to  $1.25\sigma$  from the average intensity 163. The standard deviation for the 3 3/16" Red Retroreflector intensities is  $\sigma=74$ , which is huge. As a

result, this shows the most prominent return value for intensity is 100 and the rest should be discarded as noise.

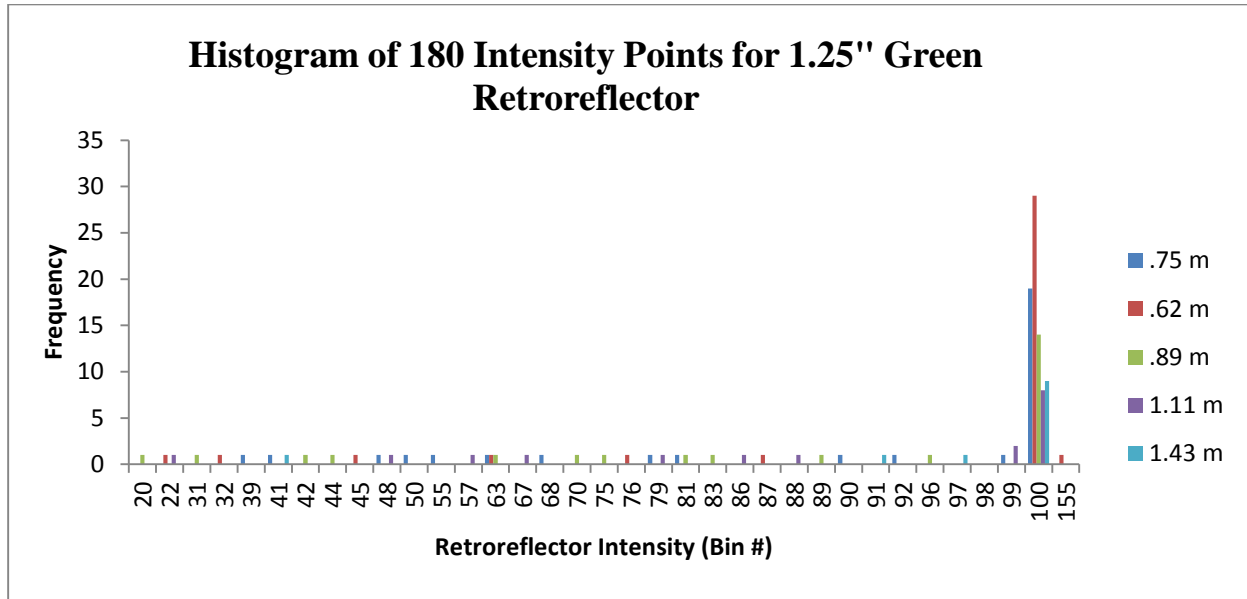


Figure 31 Measured Intensity Distribution over a series of points returned from the 1.25" Green Retroreflector that is detected by the Velodyne HDL-32E Lidar at a range of distances (.62 m – 1.43 m).

The intensity distribution in Figure 31 for the 1.25" diameter green retroreflector displays a consistent plateau at the intensity of 100 followed by a steady drop. The plateau length increases as the distance decreases, which mainly occurs because the retroreflector has more area and therefore more points to detect when the retroreflector's proximity to the Lidar increases. The actual intensity value can be concluded to be 100 for the little green retroreflector.

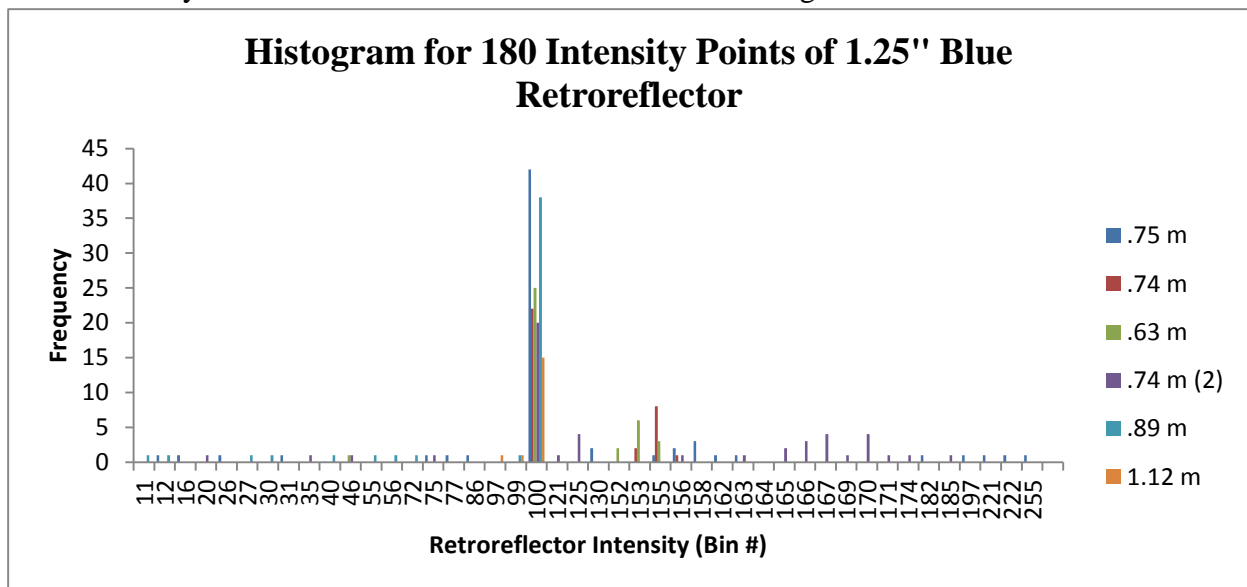


Figure 32 Comparison of Intensity Distributions for the 1.25" Blue Retroreflector read by the Velodyne HDL-32E Lidar when positioned at different distances ranging from .63 m to 1.12 m.

The 1.25" Blue Retroreflector in Figure 32 shows a consistent intensity return of 100 with minimal noise at the minimum and maximum boundaries of the range as the distance increases from .63 m to 1.12 m.

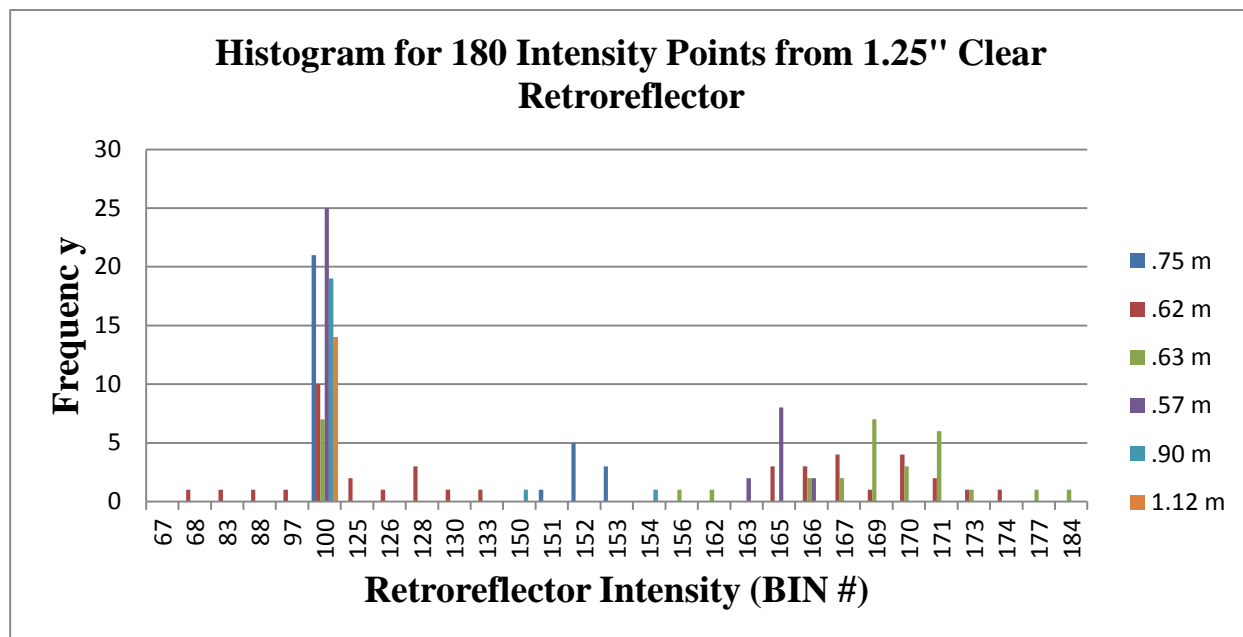


Figure 33 Comparison of Intensity Distributions for the 1.25" Clear/White Retroreflector read by the Velodyne HDL-32E Lidar when placed at different distances ranging from .62 m to 1.12 m.

In comparison, the 1.25" Clear Retroreflector in Figure 33 returns an intensity value of 100, as well as a prominent intensity return of 169 for distances less than .90 m. The Clear Retroreflector's higher intensity return of 169 is expected since clear/white reflects more wavelengths than a single color.

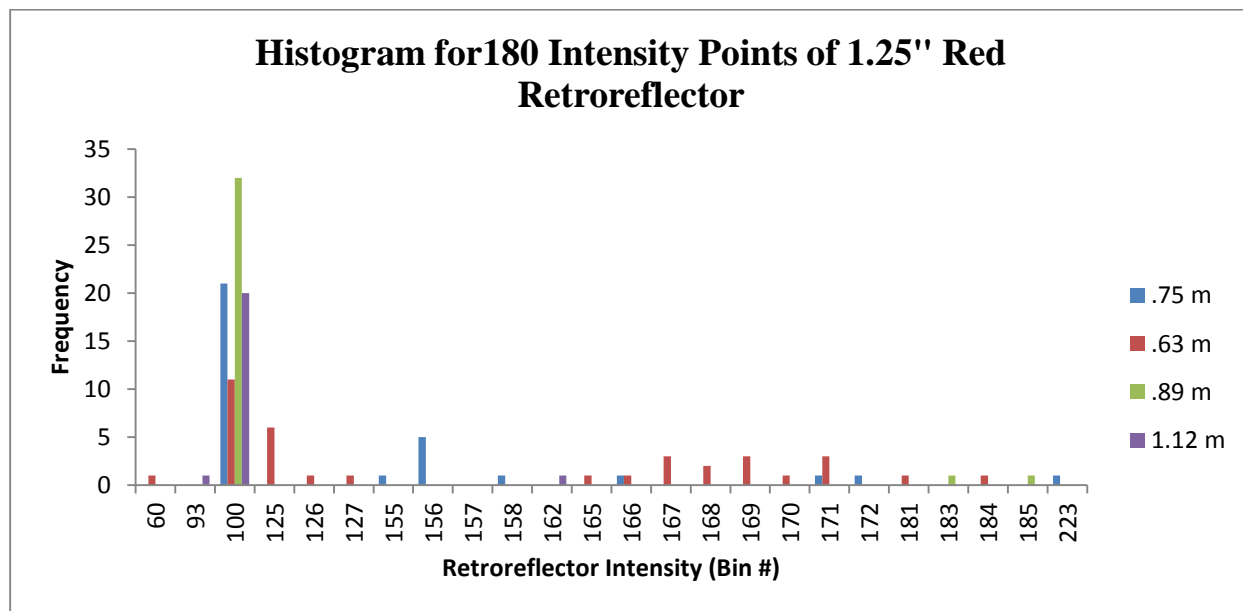


Figure 34 Comparison of Intensity Distributions for the 1.25" Red Retroreflector read by the Velodyne HDL-32E Lidar when placed at different distances ranging from .63 m to 1.12 m.

The 1.25" Red Retroreflector's intensity return of 100 remains consistent with the larger 3 3/16" Red Retroreflector's intensity of 100, but returns 167 and 125 for distances less than .63 m, as Figure 34 demonstrates.

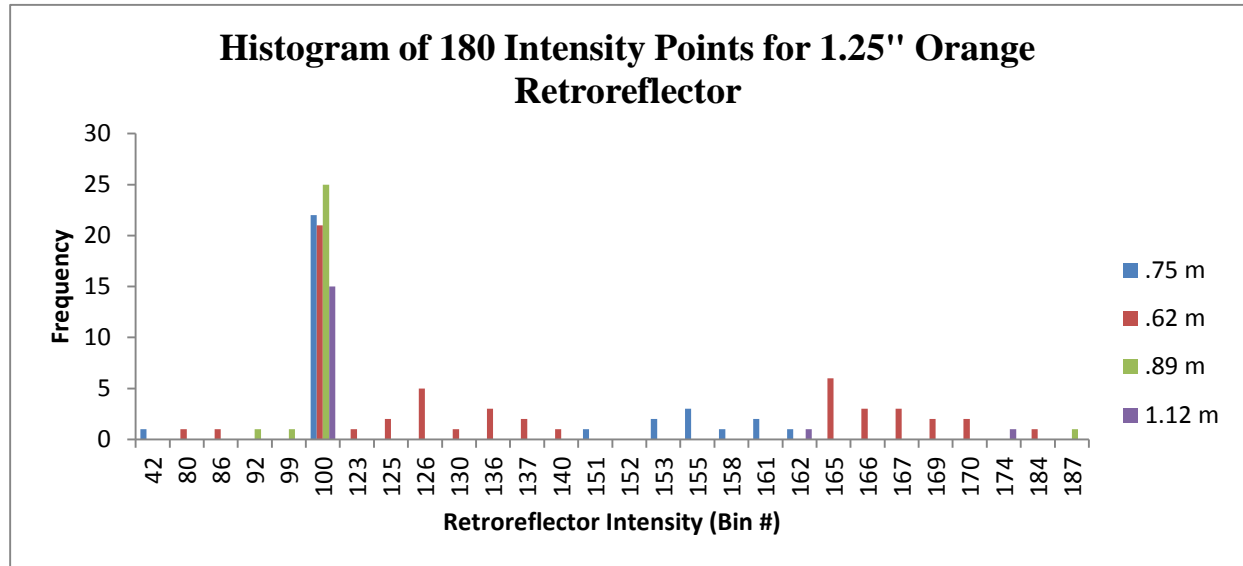


Figure 35 Comparison of Intensity Distributions for the 1.25" Orange Retroreflector read by the Velodyne HDL-32E Lidar when placed at different distances ranging from .62 m to 1.12 m.

The intensity return in Figure 35 for the 1.25" Orange Retroreflector over a range of .62 m to 1.12 m shows an average value of 100 after .75 m, but ranges from 100-166 at .62 m, which originates from the reflective surface noise the closer the Lidar is to the retroreflector.

### Profile Graph for Retroreflector Base:

The measured illumination and measured intensity for the retroreflectors are compared to understand the relationship between the object surface's reflective properties and the intensity value returned by the Velodyne HDL 32-E Lidar.

Table 17: Comparison of Measured Illumination and Measured Intensity for Different Reflectors

Reflectors	Measured Illumination	Measured Intensity
3 3/16" Red	35-42	100-255 (4-255, 180pts)
1.25" Green	63-65	20-100
1.25" Blue	45-48	100-185 (24-185, 255-12 (904))
1.25" White/Clear	29-36	100-185 (201-8)
1.25" Red	47-57	63-178
1.25" Orange	37-45	100-185

Then the values for the retroreflectors' illumination and measured intensity are graphed to develop quantitatively represent the relationship between the lower and upper limits of the ranges. The result is a boundary profile.

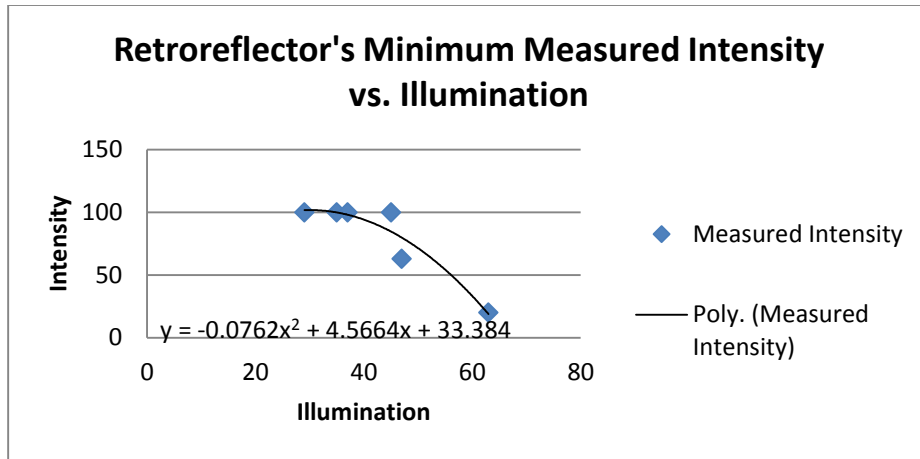


Figure 36 The Minimum Measured Intensity in relation to the Minimum Measured Illumination

The Minimum Measured Intensity vs. Illumination graph in Figure 36 shows the relationship between the minimum intensity value of a retroreflector material read from the Velodyne HDL-32E Lidar and the corresponding measured illumination from the reflectivity of the light on the retroreflector material surface. The minimum boundary intensity for the retroreflector shows a parabolic curve relationship indicating that the intensity values decrease as the illumination value increases, which for the VEX sensor means less light is reflecting off of the reflector surface.

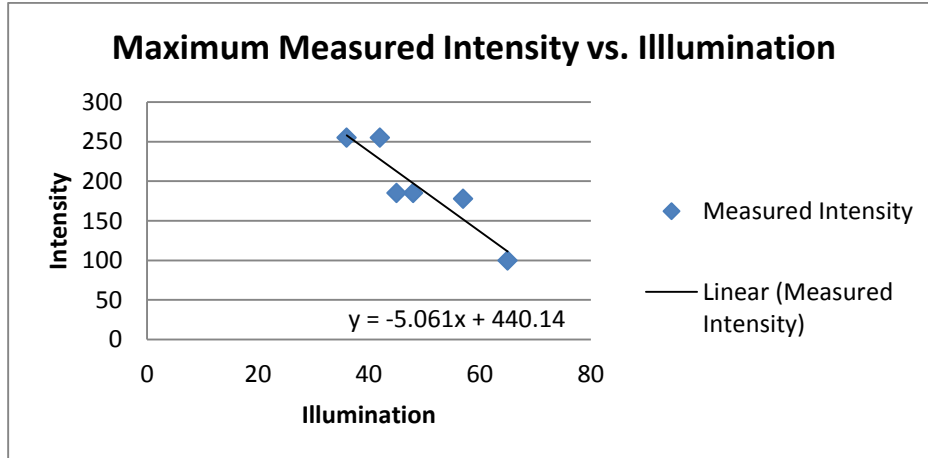


Figure 37 The Maximum Measured Intensity compared with the Maximum Measured Illumination

In Figure 37, the Maximum Measured Intensity vs. Illumination graph based on Table 17 indicates the relationship between the retroreflector's maximum intensity values read from the Velodyne HDL-32E Lidar and the related illumination from the reflectivity of the light on the material surface. The maximum value boundary for measured intensity of a retroreflector has a linear relationship with the corresponding illumination value detected by the light sensor. While the lower boundary of light detected by drop off sharply with a parabolic curve (Figure 36), the upper boundary decreases at a steady rate.

The measured illumination values are normalized from the 1-1000 (brightest to darkest) scale to the 0-255 (darkest to brightest) scale used by the Velodyne HDL-32E Lidar for a more relatable range comparison.

Table 18- Profile for Materials:

Material	Measured Illumination	Normalized Illumination	Intensity
Kiln Dried Pine	33	250	100
Yellow Buoy	58	241	86
PVC Pipe White	61	240	74
PVC Pipe Red	119	218	22
Aluminum	68	237	71
Polycarbonate	103	224	3
Light	20	255	255
Back light	589	39	0
Reflectors			
3 3/16" Red	35	249	100-255
1.25" Green	63	239	100
1.25" Blue	45	246	100-185
1.25" White/Clear	29	252	100-185
1.25" Red	47	245	63-178
1.25" Orange	37	249	100-185

As noticed in the normalized illumination values, the maximum difference between the materials is 12.8% and the minimum is .41%. When compared to the retroreflectors, the maximum difference is 13.5 % and the minimum difference is .42%. In analyzing the material illumination, the yellow buoy surface has a slightly higher normalized reflectivity value, indicating that on a range from 1-255, it reflects a high amount of light compared to PVC, aluminum, and polycarbonate. The Kiln Dried Pine, however, has a higher return value of light than the detected buoy and is on the order of the retroreflectors. The exact percent difference between the normalized illumination values for the materials can be referred to in Table 19.

Table-19 Percent Difference Table Between the Materials' Normalized Illumination Values

% Difference	Kiln Dried Pine	Yellow Buoy	PVC Pipe White	PVC Pipe Red	Aluminum	Polycarbonate	Light
Kiln Dried Pine	0.00	3.95	4.43	14.99	5.62	11.90	1.92
Yellow Buoy	3.80	0.00	0.46	10.62	1.60	7.65	5.65
PVC Pipe White	4.24	0.46	0.00	10.11	1.14	7.16	6.08
PVC Pipe Red	13.03	9.60	9.19	0.00	8.15	2.68	14.71
Aluminum	5.32	1.58	1.13	8.87	0.00	5.95	7.14
Polycarbonate	10.64	7.11	6.68	2.76	5.62	0.00	12.35
Light	1.96	5.99	6.47	17.24	7.69	14.09	0.00
Back light	84.29	83.67	83.59	81.93	83.40	82.42	84.59
Reflectors							
Giant Red	0.32	3.62	4.09	14.62	5.28	11.54	2.24
Little Green	4.56	0.79	0.33	9.75	0.80	6.80	6.39
Little Blue	1.84	2.04	2.51	12.87	3.67	9.84	3.73
Little White/Clear	0.60	4.57	5.05	15.68	6.25	12.57	1.33
Little Red	2.12	1.75	2.21	12.55	3.38	9.53	4.00
Little Orange	0.60	3.33	3.80	14.30	4.98	11.23	2.51

% Difference	Back light	3 3/16" Red	1.25" Green	1.25" Blue	1.25" Clear	1.25" Red	1.25" Orange
Kiln Dried Pine	536.39	0.32	4.78	1.87	0.60	2.17	0.60
Yellow Buoy	512.21	3.49	0.80	2.00	4.37	1.72	3.22
PVC Pipe White	509.41	3.93	0.34	2.44	4.81	2.17	3.66
PVC Pipe Red	453.44	12.76	8.88	11.41	13.55	11.15	12.51
Aluminum	502.54	5.01	0.80	3.54	5.88	3.27	4.75
Polycarbonate	468.70	10.35	6.37	8.96	11.17	8.70	10.10
Light	548.85	2.29	6.83	3.87	1.35	4.17	2.57
Back light	0.00	84.24	83.54	83.99	84.38	83.95	84.19
Reflectors							
Giant Red	534.35	0.00	4.44	1.55	0.91	1.84	0.28
Little Green	507.38	4.25	0.00	2.77	5.13	2.49	3.98
Little Blue	524.68	1.52	2.85	0.00	2.42	0.29	1.25
Little White/Clear	540.20	0.92	5.40	2.48	0.00	2.78	1.21
Little Red	522.90	1.81	2.56	0.29	2.70	0.00	1.53
Little Orange	532.57	0.28	4.15	1.26	1.19	1.55	0.00

For the marine environment, the wooden dock would return higher intensity values than the detected buoy in the water if both are at the same distance and same lighting condition. These circumstances will be discussed in further detail during analysis of the Taylor Buoys later on in the paper. Now the range and distribution of values in each object intensity profile need to be observed for a better understanding of the intensity properties for the materials.

## Intensity Range Results:

The intensity range tests are conducted to determine each test material's set of intensity values returned from its surface to the Lidar as the material is moved along an increasing distance from the Lidar. From these material intensity values, a characteristic profile can be made relating the material properties and returned intensities based on distance. The materials tested were a yellow buoy, a green buoy, a red buoy, kiln dried wood, aluminum, steel, and a black plate to discern between colors and black. As seen in Figure 38, a yellow buoy intensity profile is generated by processing the data with VeloView. The scale indicates the maximum intensity value in the image is 110. As the buoy is moved closer to the Lidar, the points begin to disappear as in Figure 39 until the object is a gap in the point cloud as seen in Figure 40. The recorded Lidar map itself also begins to distort.

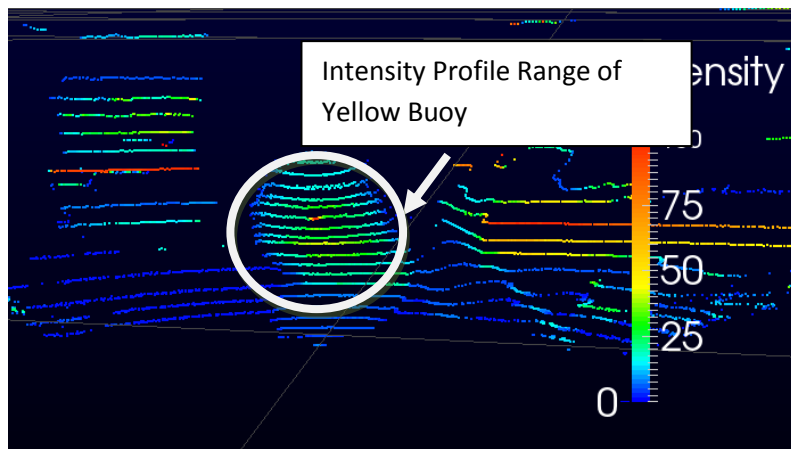


Figure 38 Yellow Buoy Intensity Distribution

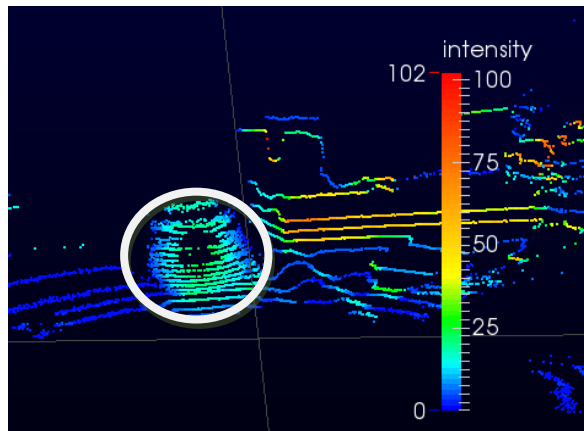


Figure 40 Buoy Placed Before Minimum Detection Threshold

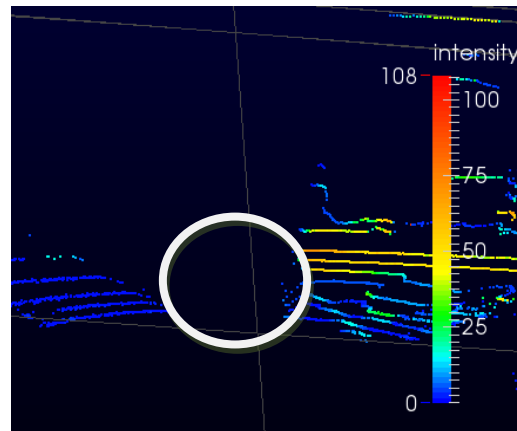


Figure 39 Yellow Buoy Approaching Closer than Lidar Range



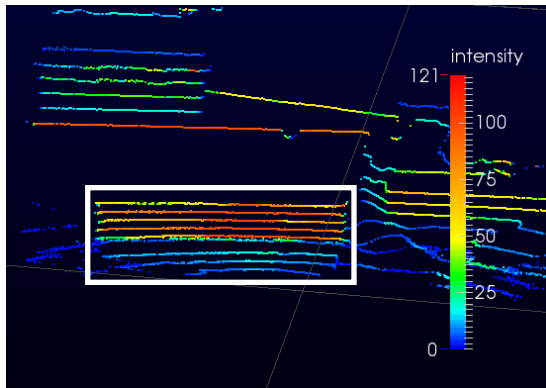


Figure 42 Kiln Dried Plank Intensity Profile

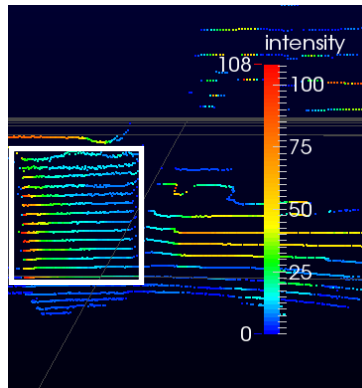


Figure 41 Aluminum Plate Intensity Profile

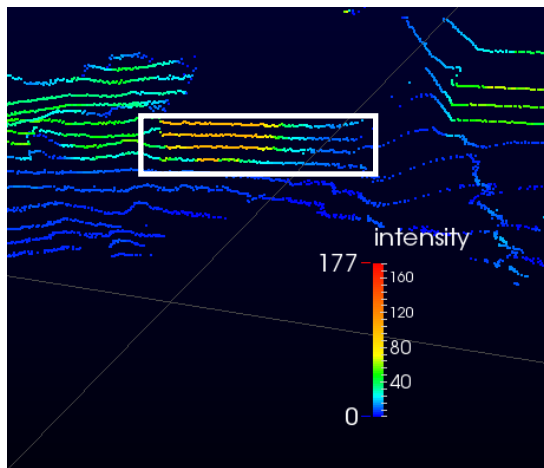


Figure 44 Steel Panel Intensity Profile

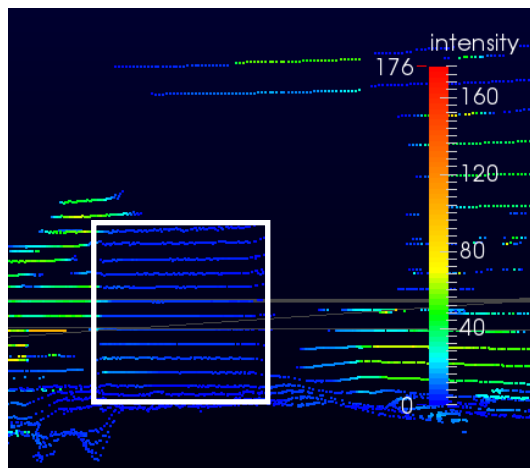


Figure 43 Black Plate Profile

Profiles for each material were made by recording the range of intensities returned off the material's surface at incremental distances. These recorded intensity ranges represent all of the data points selected within the boundary of the material's surface.

Table 20- Materials Data Table

	Distance (m.)						
	0.3352	0.4622	0.6146	0.7416	0.894	1.1226	1.4274
Material							
Yellow Buoy	0	0	1-26 (whole); 2-26 (901 pts)	1-100(whole); 11-100 (core 458 pts)	1-95 (whole); 16-95 (458 pts)	1-40 (whole); 8-40 (253 pts)	1-36 (whole); 16-36 (pt. 124)
Kiln Dried Plank	0	0	1-100 (whole); 55-100 (479 pts.)	1-100(whole); 63-100 (core 474 pts)	1-100 (whole); 57-100 (456 pts)	1-100 (whole); 21-100 (262 pts)	14-100 (whole); 20-100 (150 pts)
Aluminum	0	0	3-100; 9-71 (378 pts.)	1-100; 7-40 (421 pts)	1-100; 11- 90(456 pts)	1-100; 14-88 (245pts)	1-100 (whole); 28-100 (149 pts)
Steel Panel Sheet			5-130; 18- 139 (253 pts)	6-100;19-100 (263 pts)	1-100;41- 100; (241 pts)	24-100; 45-100 (141)	54-100; 100 (57)
Black plate	0	4	1-22; 1-8 (425 pts)	1-26 (whole); 2- 7 (459 pts)	2-16; 3-11 (458 pts)	2-14; 4-14 (269 pts)	2-38; 5-12 (158)

### Buoy Range Data Table

In comparing the Red Buoy and Green Buoy, each buoy was moved along an incremental distance from the Lidar to measure the variation in intensity values for the physical buoy body, the associated color reflector on the buoy body, and the edge of the buoy. These intensity ranges can then be used to develop a detection profile for the simulated version of the buoys in V-REP Pro.

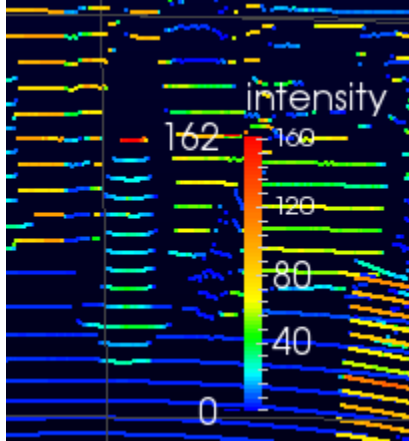


Figure 45 Red Buoy Intensity Analyzed at Varying Ranges

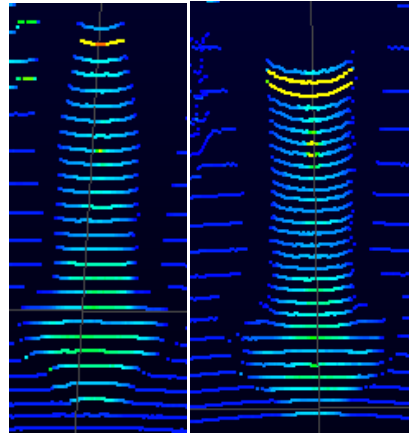


Figure 46 Comparison between Red Buoy Profile (Left) and Green Buoy Profile (Right)

Table 21- Buoy Range Data Table

Red Buoy	Head On			
Position	Distance	Profile	Reflector Value	Edge
1	198.25	9-100	15-17	22-55
2	127+1/8	9-74	102-163	9-44
3	61	20-100	97-189	19-56
Green Buoy	Head On			
Position	Distance	Profile	Reflector Value	Edge
1	204+7/8"	9-100	8-85, 14-96	3-17
2	142.5	10-103	111-129, 142-156	7-14
3	48	14-100	100	18-70

The red buoy's profile (Figure 45, Figure 46 (Left)) for the body returned an intensity range that increases from the minimum to the maximum distance. As the distance increases, the lower range values decrease to lower intensity values returned while the upper intensity value of 100 decreases mid-way to 74 and then returns to 100. The maximum value of intensity returned for the red reflector on the red buoy decreases as the distance of the buoy from the Lidar increases. The range of return values for the red buoy's base edge maintained consistent for the closest and furthest distance, but decreased mid-way. The green buoy's profile in Figure 46(Right) for the body returned an intensity range that slightly increases with distance. As the distance increases, the lower range values decrease in intensity by 1-4 increment values returned while the upper intensity value of 100 increases mid-way to 103 and then returns to 100. The intensity value

consistency of 100 confirms the initial testing of the little green retroreflector, which produced a similar intensity distribution over a range of distances (Figure 31). The values of intensity within the range returned for the green reflector on the green buoy increase mid-way as the distance of the buoy from the Lidar increases, and then decrease and widen in range further out near the further distance of 204 7/8". The range of return values for the green buoy's base edge decreased along with the minimum return intensity as the distance increased.

### Discerning Between Black and White

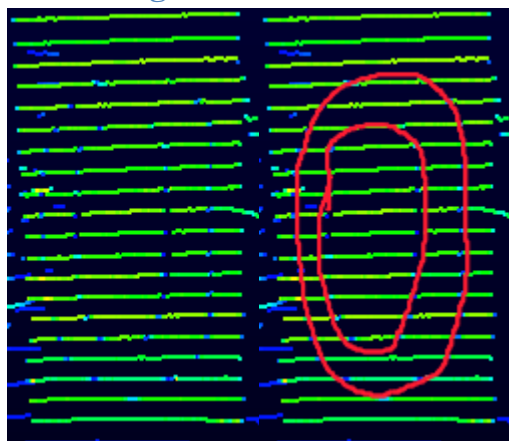


Figure 47 White Board with Black Pattern (Left) and Outlined Pattern on Board (Right)

Table 22- Black and White Data Table

Color	Intensity Range
Black Tape	2-12
White Board	65-86

The test in Figure 47 measures the Velodyne HDL-32E's ability to discern black from white in general without considering variation based on distance since the competition pattern and ratio of black to white is unknown. The setup consists of a white board with a black pattern placed perpendicular to the Lidar's laser beams. The returned intensity for the black values in Table 22 ranged from 2-12 whereas the white background ranged from 65-86. The variance between the end of the black range and the beginning of the white range is 53. The clear distinction between these ranges makes it easy to discern black and white colored obstacles on the field.

### Discerning Between Black, Red and Green

Table 23- Color Buoys Data Table

Color	Peak Intensity
Large Black Trash Container	45
Green Buoy	56
Red Buoy	63

Using the previous profile values in consideration, a test to discern three different obstacles positioned at the same distance of 4.8 m from the Lidar was conducted. The standard deviation for the intensity set in Table 23 is  $\sigma=7.41$ . While the ranges for the Green and Red buoy through previous testing show overlapping, the overall peak value for the Red buoy is greater by  $.94\sigma$  than the green buoy, and greater than the black trash container obstacle with similar surface traits to those of the buoys by  $1.48\sigma$ . While the Red and Green Buoys can be distinguished from the black trash container, the Buoys in motion may be difficult to discern from each other while in movement. The Red Buoy and Green Buoy can be discerned from each other when static.

## Point Return Results

Example Image:

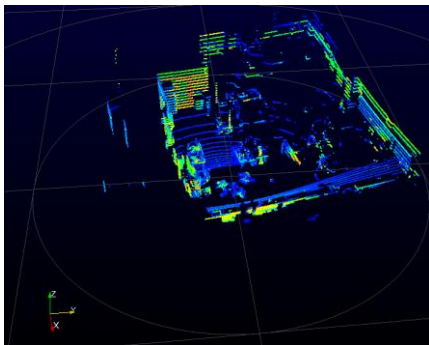


Figure 48 Point Return in Ground Lab

Table 24- Point Return Data Table:

Velodyne Run (Lab)	Max Point Return Per Frame
Angular Setup	46263
Field of View	47130
Trial3	36239
Material Reflectivity Test	23179
Retroreflector Reflectivity Test	25322
Buoy Range Testing	57569
Velodyne Run (Marine Environment)	
Run 1	3600
Run 2	4374

Another aspect to understanding the Velodyne HDL-32E Lidar is the number of points it generates within its point cloud, as demonstrated in Figure 48. Understanding the number of points within the cloud allows for programming an accurate simulation environment that reproduces a similar point cloud in the marine environment. The maximum number of points used in a point cloud as the Velodyne HDL-32E top rotates is a user specified variable. The other benefit for determining the number of generated points is to limit the amount of processing and RAM required for running the simulation. A computer running the simulation is limited by the amount of RAM it has, so any means of removing unnecessary data and reducing the amount of processing will aid in runtime and minimize a potential crash. The manual states that the

Velodyne HDL-32E Lidar shoots 694, 292 laser points per second. In analyzing point cloud data, however, the questions becomes how many cloud points per frame will be processed in the environment. Within the lab, the max point return during testing ranged from 25322 points per frame to 57569 points per frame. This is drastically more than the 3600-4374 points per frame that the Velodyne HDL-32E Lidar mounted on the WAM-V generated when testing on the Halifax River. Part of the reasoning for this reduced point cloud return is the minimal reflectivity of the laser beams off the water's surface because of its high absorption rate. Another reason is there are less objects to detect in the marine environment, which consists of water, a dock, and a couple obstacles, within its field of view between .5m and 70 m compared to the lab, which consists of multiple lab objects.

## Total Error Correction Equations

### Based on using Lidar Parameters, Adjusted Variables, and Provided Resources:

The process for modeling the Velodyne HDL-32E Lidar scanner and creating a 3D position by converting time of flight distance data generally operates as follows. First, the variables for the Lidar's packet characteristics (i.e. payload size, port, and length) and laser beam arrangements (i.e. blocks, firing angles, firing order) need to be defined.

Then the laser data point variable `vls_point` is defined by distance and intensity. A data set for firing a laser group is defined. After the variables for data points are defined, the CM value for the laser set time of flight distance reading `distLSB` and the five parameters used for Lidar correction previously mentioned, which are `vertCorrection`, `rotCorrection`, `distCorrection`, `horizOffset Correction`, `vertOffsetCorrection`, can be implemented. In considering the coordinate system for these computations, the positive y-axis is at zero degrees rotationally and the Lidar rotates clockwise about the z-axis. The vertical correction of the laser beams is split into a cosine vertical correction table and a sine vertical correction table. These calibration values based on each laser are set in a general calibration table for initial x, y, and z position. From there, the general distance correction pseudo code goes as follows:

$$d = DistLSB_i * d_{points(idx)} + DistCorrection_i$$

The values for the vertical angle correction (laser beam  $i$ 's oriented vertical angle) and the rotation correction value for laser beam  $i$  are retrieved from the calibration table matrix:

$$\cos(\varphi_i) = CosVertCorrection(cal_i)$$

$$\sin(\varphi_i) = SinVertCorrection(cal_i)$$

$$\cos(\theta_{correction}) = CosRotCorrection(cal_i)$$

$$\sin(\theta_{correction}) = SinRotCorrection(cal_i)$$

Based on the properties:

$$\cos(a - b) = \cos(a) * \cos(b) + \sin(a) * \sin(b)$$

$$\sin(a - b) = \sin(a) * \cos(b) - \cos(a) * \sin(b)$$

The cosine and sine rotation angle equations for the Lidar position correction equations become:

$$\theta = \theta_{position} - \theta_{correction}$$

$$\cos(\theta) = rotCosTable_{position} * \cos(\theta_{correction}) + rotSinTable_{position} * \sin(\theta_{correction})$$

$$\sin(\theta) = rotSinTable_{position} * \cos(\theta_{correction}) - rotCosTable_{position} * \sin(\theta_{correction})$$

The horizontal and vertical offset corrections are applied to planes orthogonal to the rotation corrected laser beams.

$$d \neq VLS_{DIM_{SCALE}}$$

$$h_{OSC} = \frac{H_{OSC}(cal)}{VLS_{DIM_{SCALE}}}$$

$$v_{OSC} = \frac{V_{OSC}(cal)}{VLS_{DIM_{SCALE}}}$$

The distance  $dx$  is computed as the distance in the  $xy$  plane without accounting for rotation:

$$distance = d_i = \text{laser } i \text{ distance correction equation}$$

$$\varphi = \varphi_i \pm \text{angular accuracy}_i$$

$$d_1 = 3E^{-05}x^3 - 0.0003x^2 + 0.977x + 0.0006$$

$$dx = distance * \cos(\varphi) - v_{OSC} * \sin(\varphi)$$

The position is used to define the scanner position. The rotation angle and horizontal offset are also factored into the equations.

$$x = d_x \sin(\theta) - h_{OSC} \cos(\theta) + \frac{posx_{scanner}}{VLS_{DIM_{Scale}}}$$

$$y = d_x \cos(\theta) + h_{OSC} \sin(\theta) + \frac{pos_{scanner}}{VLS_{DIM_{Scale}}}$$

$$z = dssin(\varphi) + v_{OSC} \cos(\varphi) + \frac{pos_{scanner}}{VLS_{DIM_{Scale}}}$$

## Real-World Data Comparison

After establishment of the total error correction equations to be used in the simulation environment, data from the WAM-V in the marine environment must be considered. Embry-Riddle's RobotX team took the autonomous marine vehicle (Figure 49) out onto the Halifax River for a series of tests, which included recording data from the Velodyne HDL-32E Lidar. The dock along the river bank consists of wooden bridges and concrete poles on a concrete platform, as shown in Figure 50.



Figure 49 ERAU WAM-V operating on the Halifax River



Figure 50 The Dock on the Halifax River

The data gathered by the Velodyne HDL-32E Lidar during these vehicle runs can be reviewed for environment intensities, distances, and dynamic behaviors.

### Marine Environment Run Image Example:

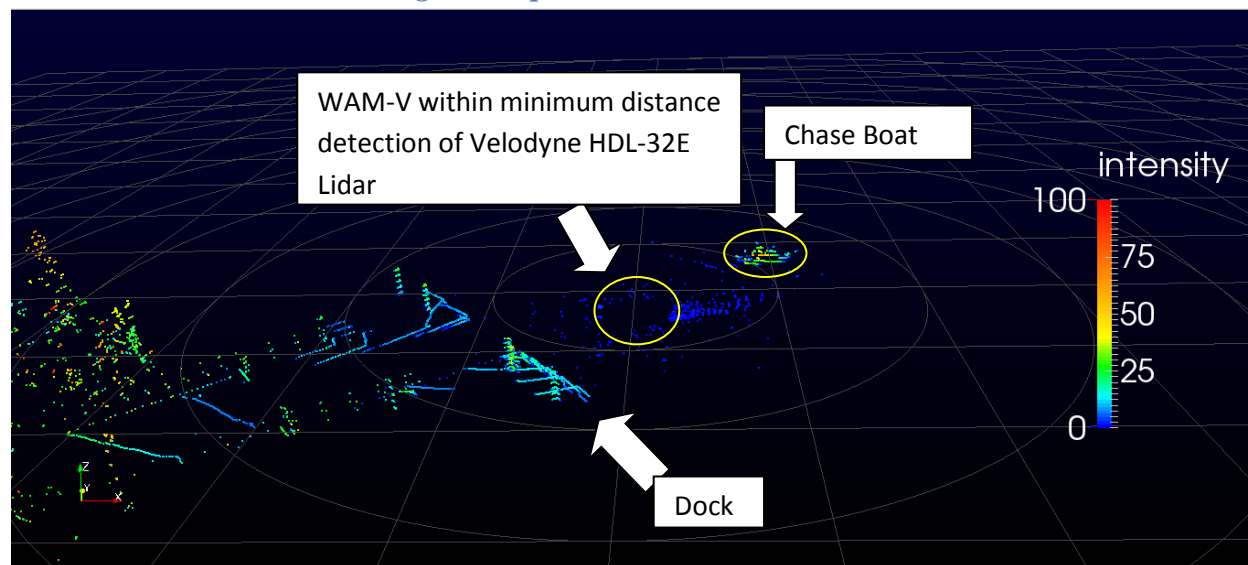


Figure 51 Velodyne HDL-32E mounted on WAM-V vehicle in Halifax River

Table 25- Marine Environment Data Sample Table:

Marine Environment	Distance (m)	Intensity
Concrete Posts on Dock	19.1	2-37; 1-49
Water in Halifax River	3.32-4.9	0-6
A-1 Buoy	10.4 m	19



## Marine Environment Data Analysis:

As can be seen within Figure 51, the water return values range from an intensity of 0 to 6. This intensity range matches theoretical claims that water's reflectivity is 5%, meaning if 100 watts of light was to fall on water it would reflect 5 watts and absorb 95 watts. This low reflectivity derives from the fact that the laser beams within the Velodyne HDL-32E are light of the near-infrared wavelength of 905 nm, which water highly absorbs. The concrete poles on the dock measure a reflectivity reading of 2-37. The A-1 buoys in the marine environment can return a value of 19 at 10.4 m.

## Simulation:

V-REP's default simulation environment consists of a generic floor platform, basic lighting, a dummy for setting a default reference coordinate system for camera views, and a camera for simultaneously looking at the scene from a different angle when a floating view is added. The simulator provides the option of using the Bullet, ODE, or Vortex physics engine. For this simulation, the Bullet engine is used because of its accuracy and real-time simulation efficiency. The time steps (dt) can be increased or decreased, but the default is 50 ms.

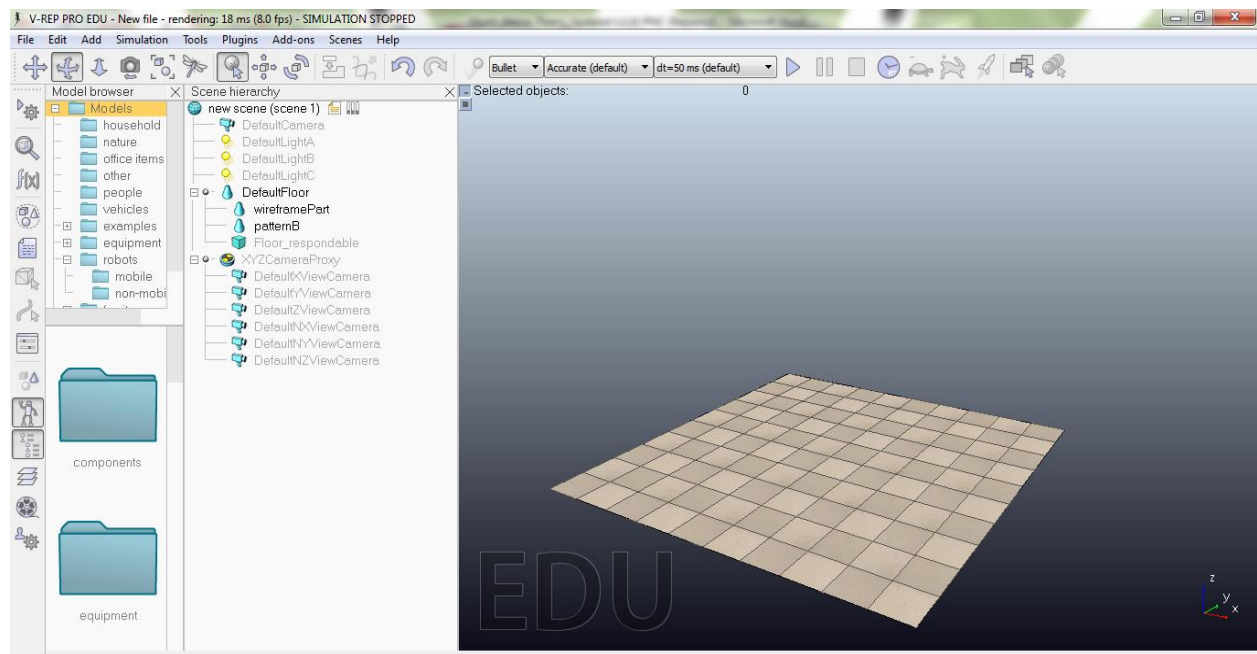


Figure 52 New Default Scene in V-REP PRO EDU

The simulation environment in Figure 52 requires obstacles to virtually test the Velodyne HDL-32E Lidar. The purpose of these tests is to match the simulation with results from the physical tests with the Lidar. The obstacles are made from scratch in Autodesk 3ds Max (Figure 53) and V-REP (Figure 54) and the surface properties are adjusted to represent intensities expected to be read by the Lidar (Tables 14-20).



### Simulation Models:

Initially, generic light buoys and A-1 buoys are modeled in 3DS Max for setting up Task 5 in the marine environment for testing, as shown in Figure 53.

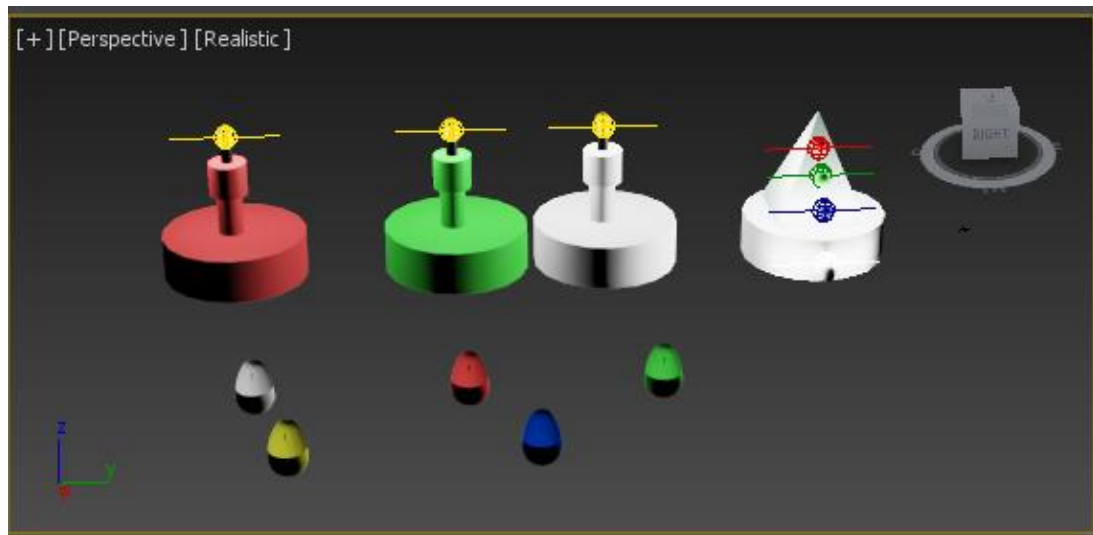


Figure 53 Buoys in 3DS Max developed with light sources and surface meshes integrated. Note: The light tower design is prior to Updated Maritime Rules 03/21/14. The buoys are generic.

The generic buoys are typically found for navigational purposes in the marine environment. With the decision to test with Taylor buoys in Spring of 2014, the generic buoys are replaced with red, green, and white Taylor buoy models.

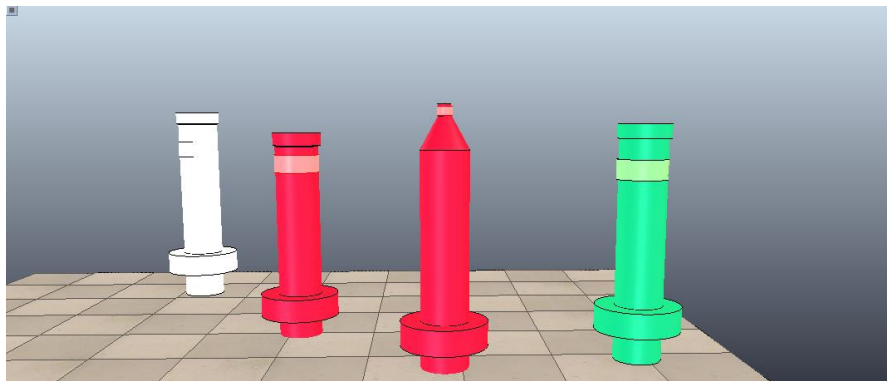


Figure 54 Taylor Buoys (White, Red, and Green)

The Taylor Buoys in Figure 54 are used to test the WAM-V in the marine environment under the basis that such buoys were used for the AUVSI RoboBoat competition.

A scripts editor (Figure 55) in V-REP allows the user to declare objects, build a hierarchy, and setup a sequence of events. The main script contains the default settings, initialization instructions, and declaration of objects, variables, functions, and libraries. Each child script consists of calling variables and functions, declaring used objects, algorithms for processing data such as distance correction, dynamic and surface properties, and information for generating a 3D point cloud. Data is sent and received via created tubes in each child script.

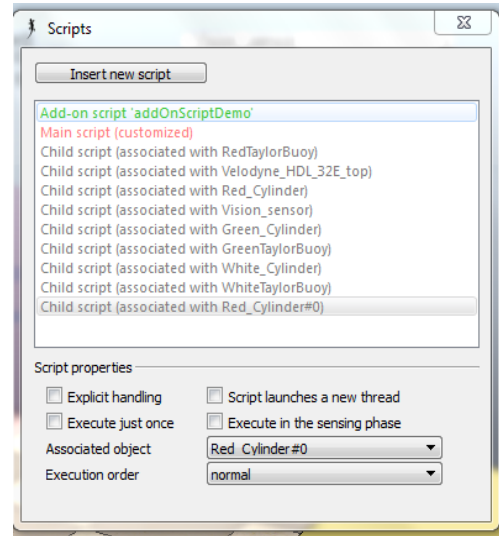


Figure 55 Script Editor for Simulation Environment

In running the simulation, a series of isolated tasks are setup to test the Velodyne HDL-32E Lidar's simulated performance. The first test checks the Lidar's detection of the obstacle. The setup consists of a Velodyne HDL-32E Lidar mounted on top of a dining table and a red Taylor Buoy (Figure 56).

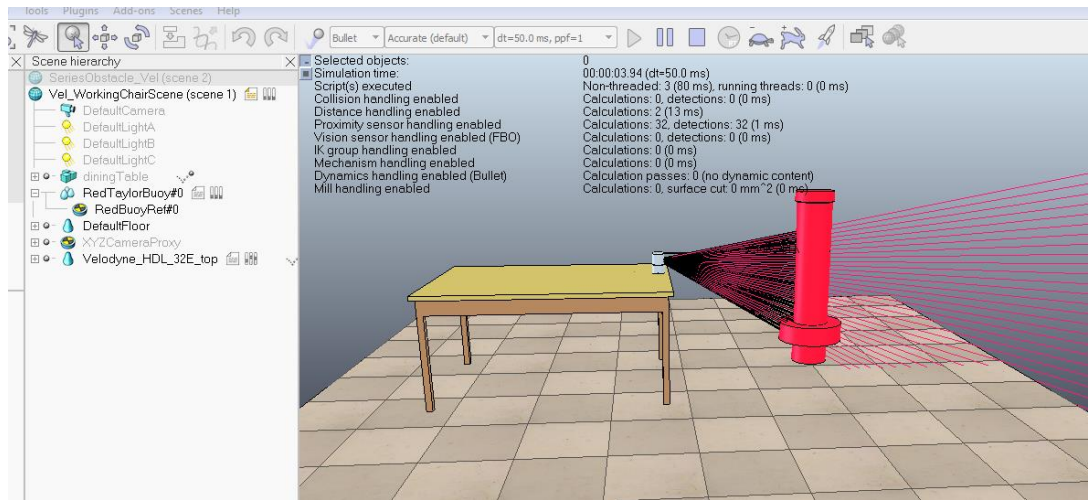


Figure 56 Setup of Velodyne HDL-32E Lidar detecting Red Taylor Buoy

When the Velodyne HDL\_32E Lidar detects an obstacle, the detection reads positive for the proximity sensor, and the lasers that detect the obstacle light up yellow to indicate the detection (Figure 57).

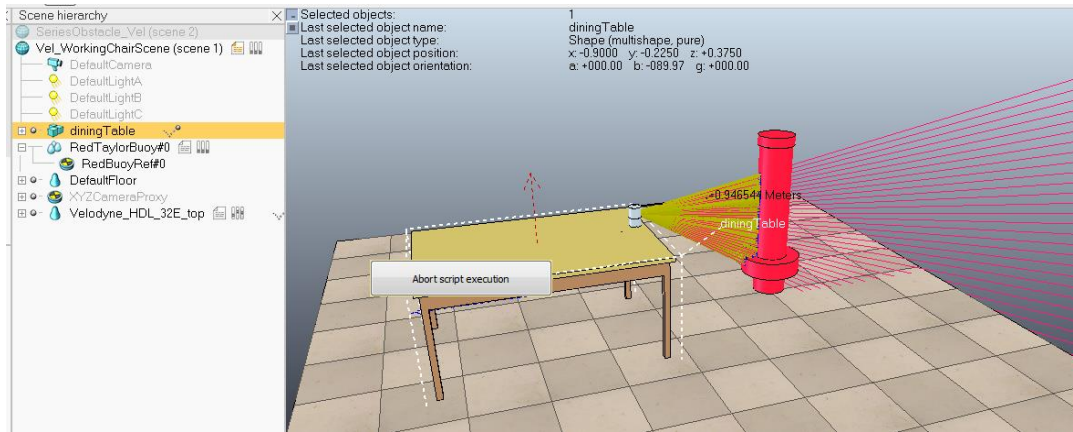


Figure 57 Velodyne HDL-32E Lidar Detects (Yellow Highlight) Red Taylor Buoy

The second test requires generating a 3D point cloud of the points detected by the Lidar with its 32 lasers, which are considered proximity sensors. Each point in the point cloud consists of an x, y, x coordinate represented a blue point and segment in the Boolean point cloud generation. The Velodyne HDL-32E Lidar is taking 20 frames per second, with 694, 292 measurements per second.

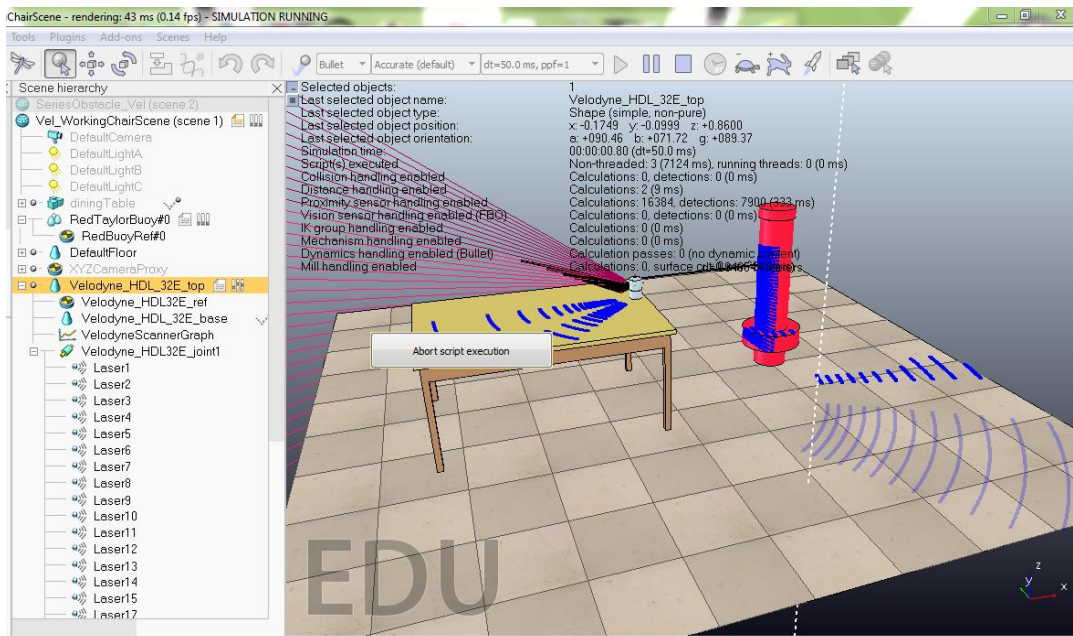


Figure 58 Velodyne HDL-32E generating 3D point cloud (with segment option off)

Once a 3D point cloud is generated (Figure 58), and clarifies the detection and location of points based on the surface and obstacles present in the environment, a printing console can be displayed for measurement data. Each matrix was sorted through, and the actual distance, error modeled distance, and the corrected distance were all printed to the main console (Figure 59).

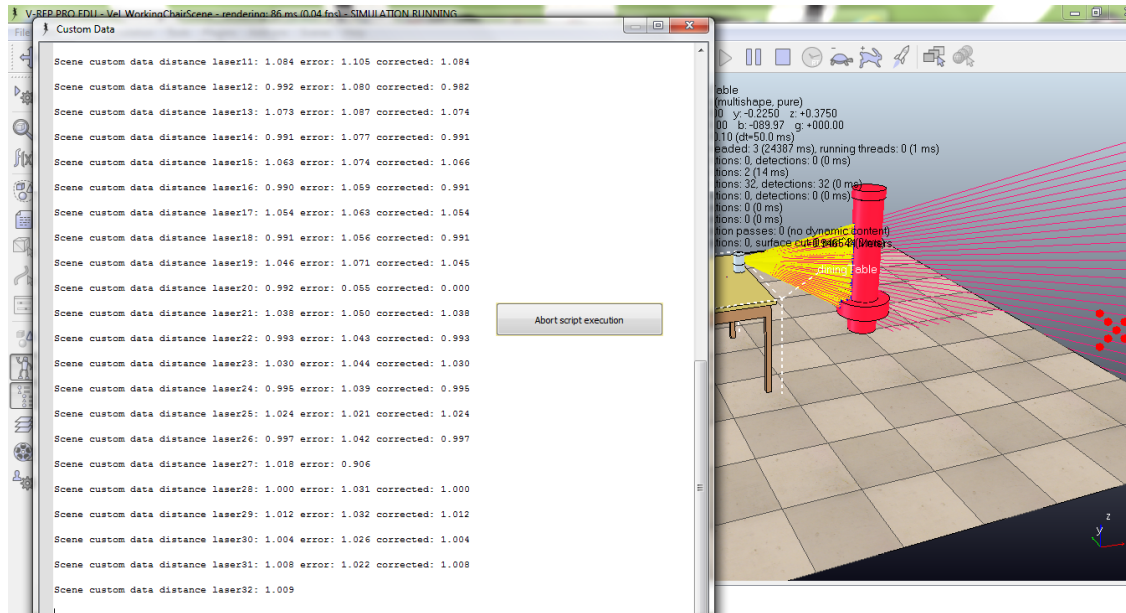


Figure 59 Lidar Detection of Buoy with Console Display of Actual Distance, Error Distance, and Corrected Distance in Meters

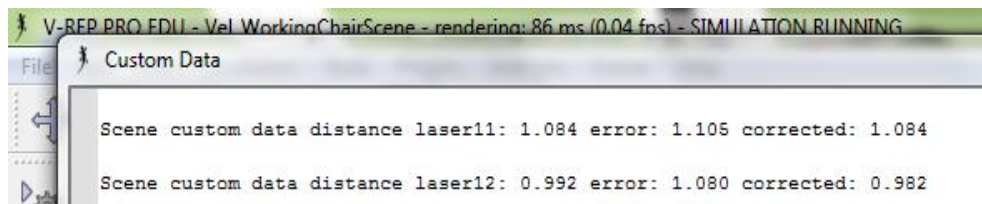


Figure 60 Output of Actual Measured Distance, Simulated Distance with Error, and Corrected Distance

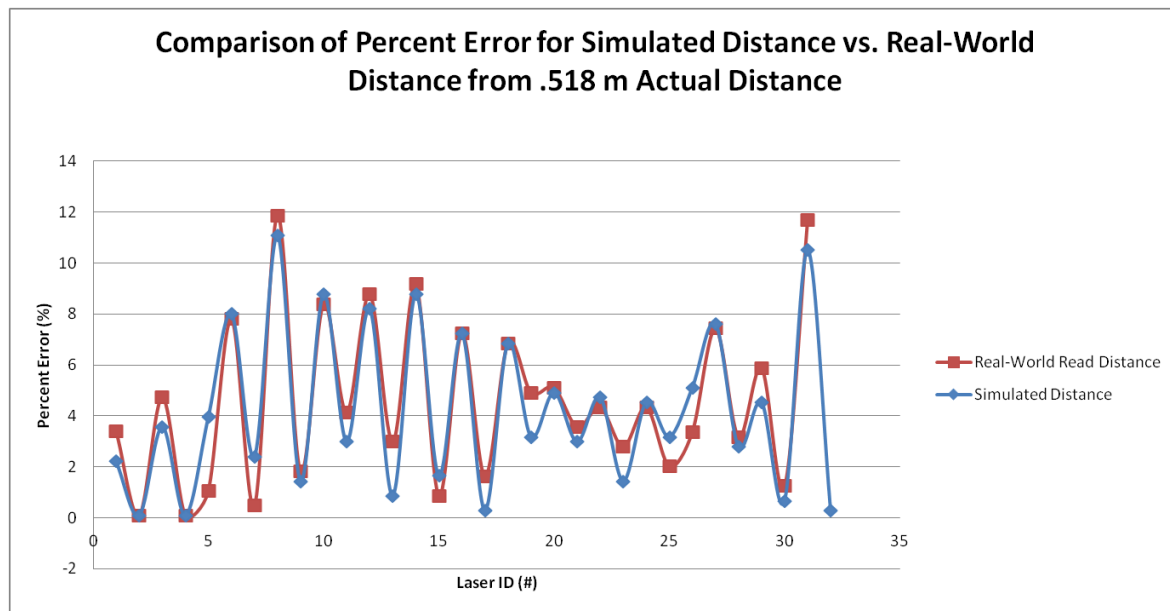


Figure 61 Comparing the Simulated and Real-World Values read from each laser of the Velodyne HDL-32E, which is .518 m from the Red Taylor Buoy

In Figure 61, the percent error between the uncorrected simulated distance and the actual distance the Red Taylor Buoy is from the Velodyne HDL-32E reveals to be between -2% and 11%. The percent error between the real-world distance read from the Velodyne HDL-32E Lidar and the actual distance of the Red Taylor Buoy ranges from -1% to 12%. When comparing the simulated percent error data with the real-world percent error data for each Lidar identified from #1 to #32, the trend patterns are the same, and the percent error differs from 0-2%. Originally, Lidar #27 did not produce the same pattern for simulation versus real-world because the error model equation did not acceptably follow distance values less than 1.13 m. The model for #27 was split into three step functions:

$$y = -0.1991x^2 + 1.1231x + 0.0281 \text{ for } x < 1.13 \text{ m}$$

$$y = 0.0001x^2 + 1.0148x - 0.0144 \text{ for } x < 5.8 \text{ m}$$

$$\text{and } y = 1.0157x - 0.0156 \text{ for } x > 5.8 \text{ m}$$

where x is the input value read by the Laser 27 and y is the modeled error distance value to be corrected. As a result, all 32 lasers in the simulation model maintain a percent error difference from the real-world values by a range of 0-2%.

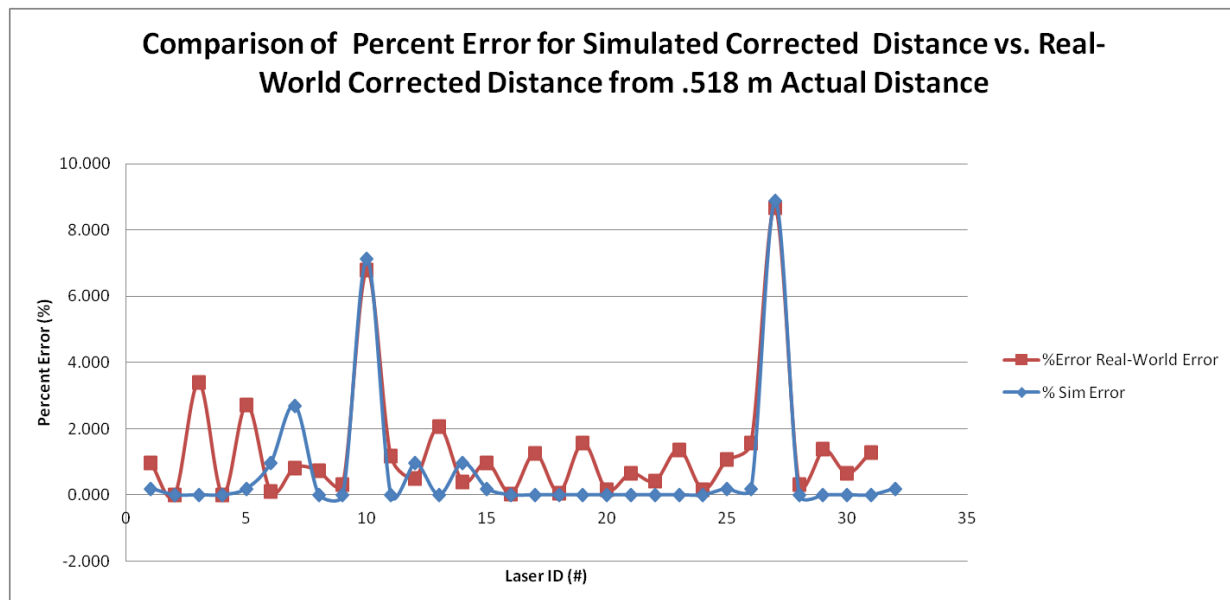


**Figure 62 Comparison of the Percent Error for the Corrected Simulated and Corrected Real-World Distance values read from each of the 32 lasers in the Velodyne HDL-32E, which is .518 m from a Red Taylor Buoy**

The comparison in Figure 62 shows the percent error for the corrected simulated values in relation to the actual Red Taylor Buoy's distance of .518 m, as well as the percent error for the corrected real-world distance relative to the Red Taylor Buoy's .518 m distance from the Velodyne HDL-32E Lidar. The corrected values for the corrected simulated percent error values and the corrected real-world percent error values are corrected to be within a maximum 8.7% (Laser #10) error from the actual distance of .518 m, whereas the uncorrected data sets had a maximum percent error of 12% (Laser #8). The corrected simulated values for 17 of the 32 lasers



were corrected to about .518 m, whereas the remaining five varied from 1%-7%. The percent error for the real-world distances varied from -3.4% to 8.7% from .518 m. The slight difference in the uncorrected values generated the larger variation in output from the correction equations.

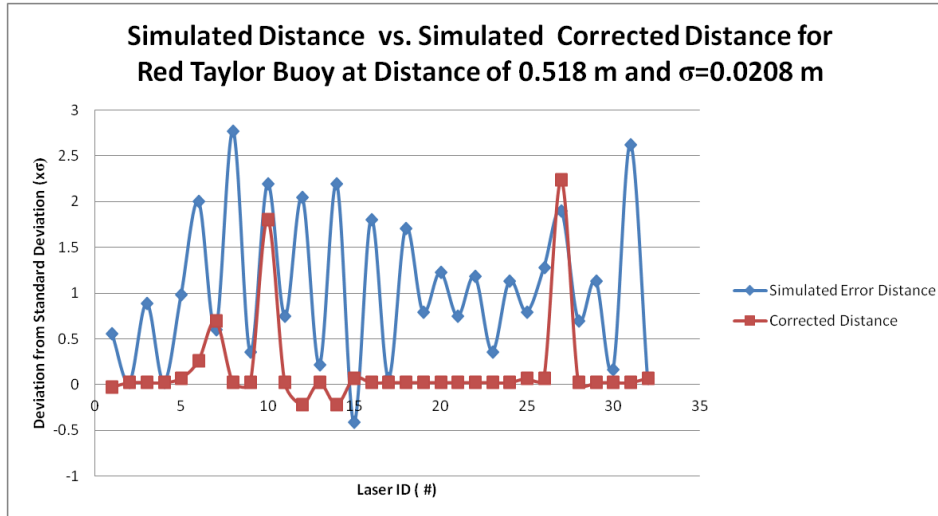


**Figure 63 Comparison of the Deviation from Standard Deviation of the Simulated Distances and Corrected Simulated Distances for the Red Taylor Buoy placed 0.518 m from the Velodyne HDL-32E Lidar. The standard deviation for this graph is 0.0193 m.**

In Figure 63, the simulated uncorrected distance and simulated corrected distance are compared to show the improvement of deviation from uncorrected to corrected distance. For each of the 32 lasers in the Velodyne HDL-32E Lidar detecting the Red Taylor Buoy at a .518 m distance, the simulated uncorrected distance readings have a deviation of  $-0.411\sigma$  ( $-0.00855$  m) to  $2.77\sigma$  ( $0.0576$  m) from the standard deviation of  $\sigma = 0.0208$  m. The value  $3\sigma$  is statistically a large deviation, which supports the need to correct the uncorrected distance readings in the simulation. In the Figure 63 comparison, the corrected distance readings deviate from  $-.218\sigma$  to  $2.24\sigma$ , showing a reduction in deviation from the standard deviation compared to the uncorrected distances. Then the real-world distance and real-world corrected distance are compared in Figure 64 for comparison to the discussed simulation distances.

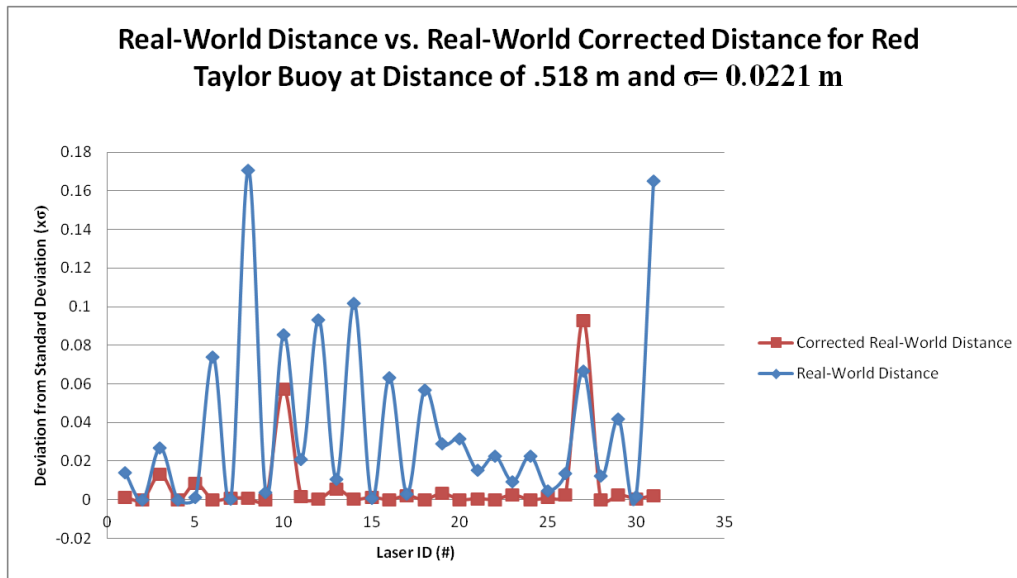


Figure 64 Comparison of the Deviation from Standard Deviation of the Real-World Distances and Corrected Real-World Distances for the Red Taylor Buoy placed 0.518 m from the Velodyne HDL-32E Lidar. The standard deviation for this graph is 0.0221 m.

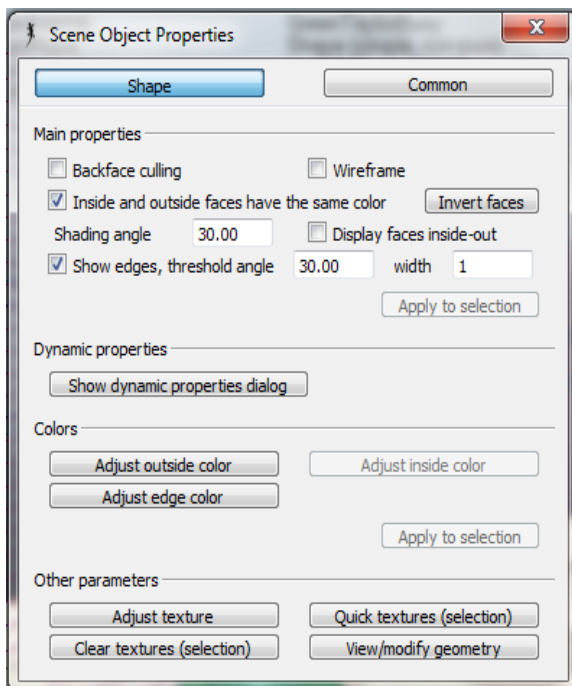


Figure 65 Scene Object Shape Properties User Interface associated with Green Taylor Buoy

Figure 64 graphs the deviations from the standard deviation of the real-world uncorrected and corrected data for each of the 32 lasers in the Velodyne HDL-32E Lidar detecting the Red Taylor Buoy at a .518 m distance. The real-world uncorrected distance readings have a deviation of  $-1.02\text{E-}05\sigma$  to  $.171\sigma$  from the standard deviation of  $\sigma = 0.0221$  m. The corrected distance readings deviate from  $1.43\text{E-}07\sigma$  to  $0.0931\sigma$ , showing a 45.6%-98.6% reduction in deviation from the standard deviation compared to the uncorrected distances.

The next test consists of simulating measured intensity values for the Red Taylor Buoy obstacle used in the marine environment. Each obstacle's outside color (ambient, diffuse, specular, emissive, shininess, and opacity), edge color, dynamic (static for test), and surface properties are adjusted accordingly.

In Figure 65, the Scene Object Properties panel allows users to access and adjust properties related to the shape's surface, structure, and dynamics. The dynamic properties dialog allows you to define the object's main properties, material properties, mass, principal moments of inertia/mass, and position/orientation of inertia frame with relation to the world or shape frame. The main properties include whether the object is static or non-static, conditional terms if it has a

parent, and sleep mode. The material properties include whether the body is responsible. If so, the user defines what layers the local and global responsible masks exist on and the material properties, which can be generic or user defined. The outside color can be adjusted based on ambient, diffuse, specular, and emissive components using RGB (Red, Green, and Blue)/HSL (Hue, Saturation, and Luminosity). The pulsation parameters, shininess and opacity can also be defined. Other parameters such as texture and geometry parameters (i.e. boundaries and ratios) can be modified.

The Common Scene Object Properties in Figure 66 allow the user to define general properties, visibility layers, object special properties, model definitions, scaling, assembling, and custom data. The General

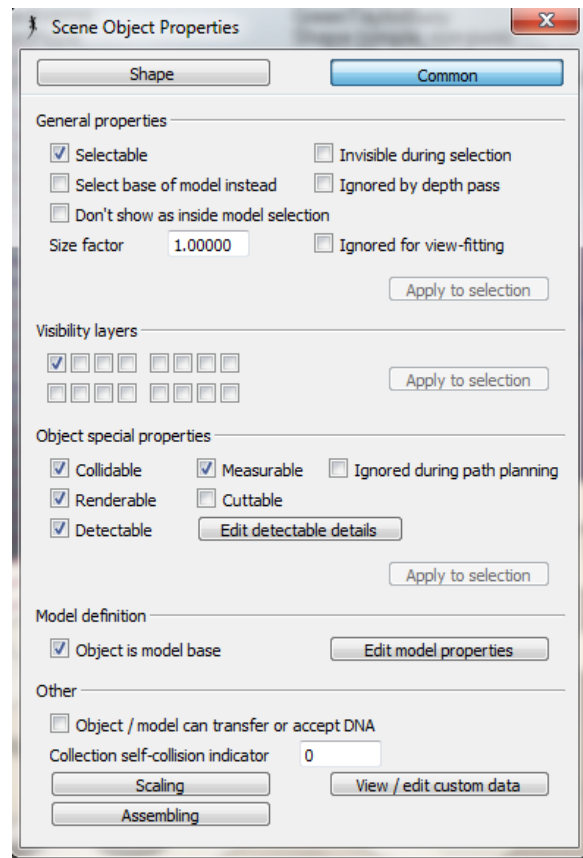


Figure 66 Scene Object Common Properties User Interface associated with Green Taylor Buoy

properties allow for defining selectable interaction between the user and the object while the simulation is running. Visibility layers define the hierarchy of visible object layering, particularly if two objects interact with each other. Object special properties allow you to turn on the collidable, measurable, renderable, cuttable, and detectable calculation modules that can be used to define and determine chosen object interactions. The detectable details allows you to define which types of sensors these parameters apply to.

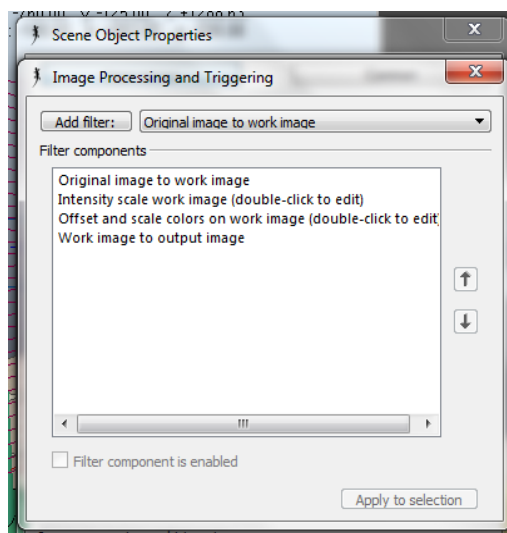
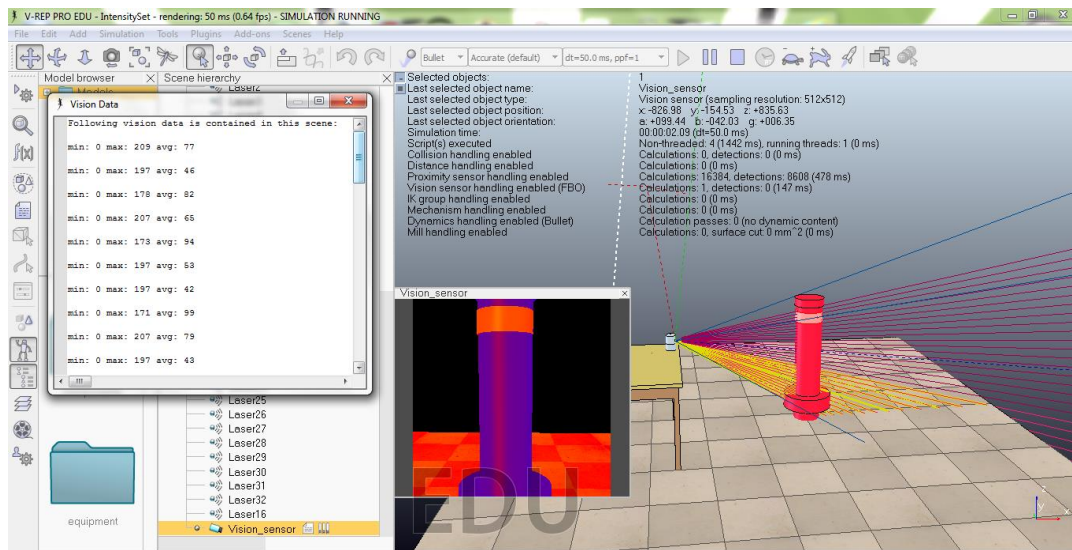


Figure 67 Image filtering layers to set scales and interpret reflective properties of objects so Velodyne HDL-32E Lidar can output intensity values

The rest of the customized features for each property are hardcoded into the child scripts for the Velodyne HDL-32E Lidar and each Buoy. These properties are declared in the main script. The intensity range values partially derived from the filter process in Figure 67 are communicated between the Lidar and the obstacle via communication tubes. A created “Vision Data” console reports minimum intensities, maximum intensities, and average intensities. A floating view in Figure 68 visually displays the detected obstacle’s intensities.





**Figure 68** Detection of Red Taylor Buoy's Intensity Values with Console displaying Minimum, Maximum, and Average Intensity Values

The same methodology applies to the other obstacles, such as the Green Taylor Buoy and White Taylor Buoy. The intensity value ranges and output intensity color scale differ depending on the buoy surface properties such as color. The real-world data shows the Red Taylor Buoy should return higher intensity values than the Green Taylor Buoy.

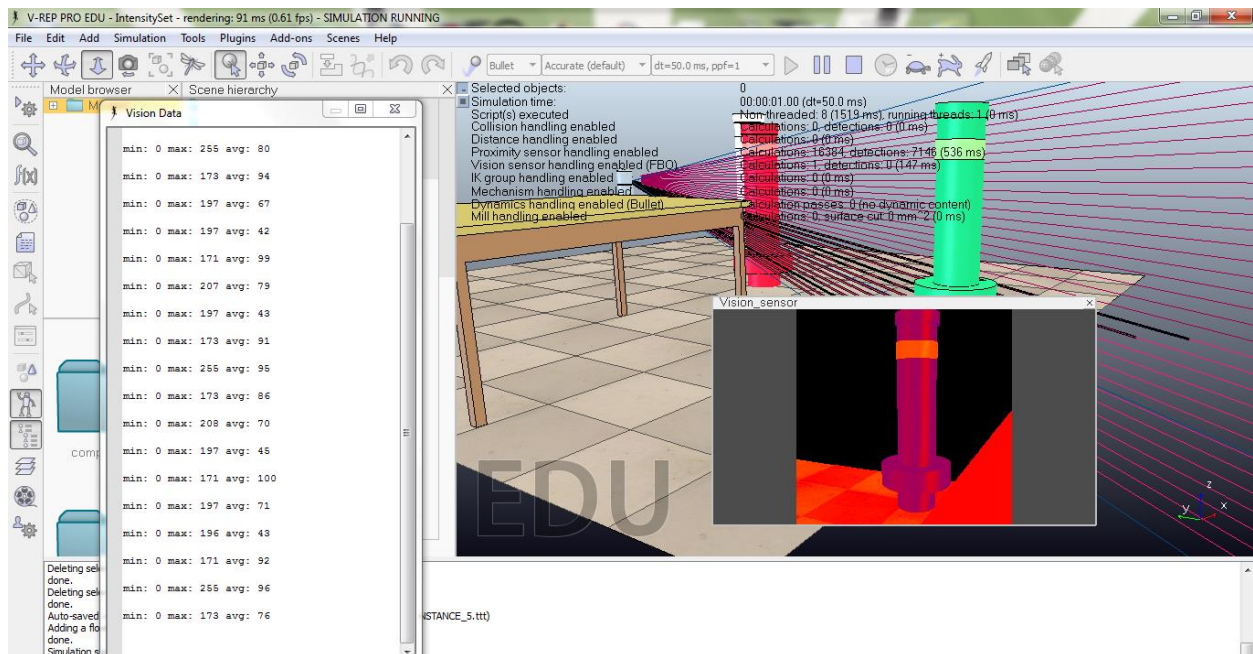


**Figure 69** Intensity Value Setup Applied to Green Taylor Buoy in Scene including White Taylor Buoy, Red Taylor Buoy, and Green Taylor Buoy

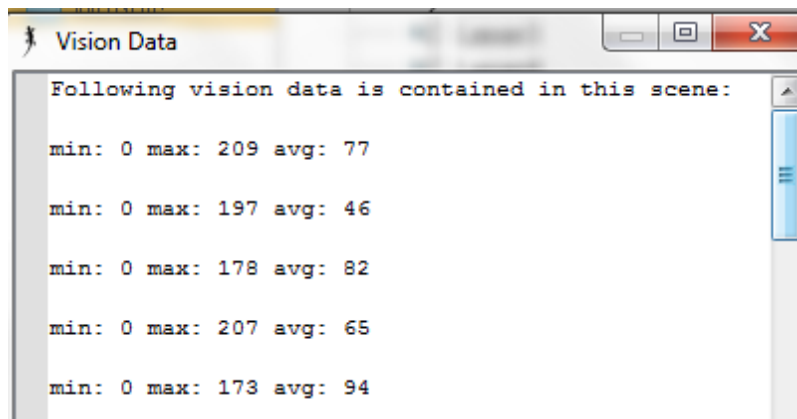


Figure 70 Intensity Values for Green Taylor Buoy Body and Reflector against Base Minimum Intensity of Zero

The range of intensity values for the Red Taylor Buoy body is 9-74 and the reflector value is around 163-198. The values for the Green Taylor Buoy body shown in Figure 70 read from the simulation have an average range of 46-94 and the reflector value has a max intensity of 209, which is higher than the Red Taylor Buoy. The textures are readjusted by reconfiguring reflective data values for light interacting with the buoy surface so the Red Taylor Buoy values are higher and closer in similiarity to the intensity and spectrum scales of the real-world Taylor Buoys.

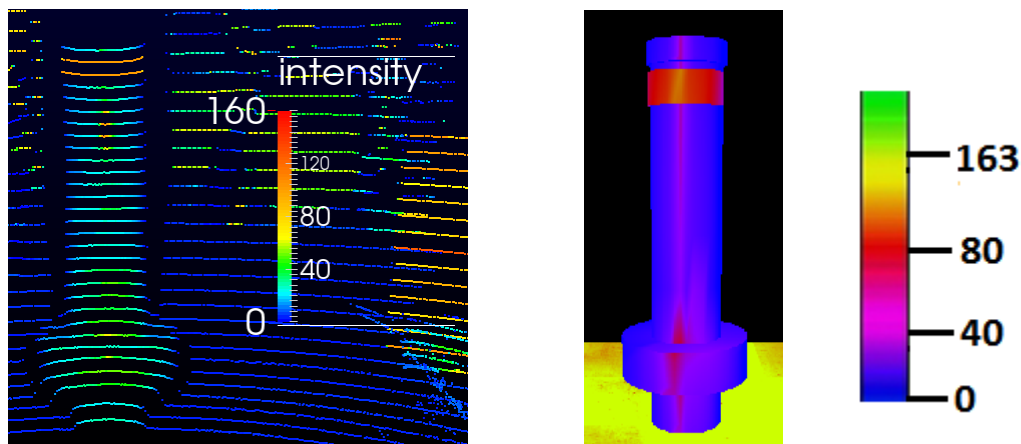


Figure 71 Intensity Data of the Green Taylor Buoy read from Velodyne HDL-32E Lidar, accompanied by the intensity spectrum scale using VeloView (Left). In comparison, the simulated Green Taylor Buoy (Right) shows the simulated intensity values accompanied by its intensity spectrum scale.

Table 26: Intensity Distribution for Green Taylor Buoy Sections

Green Buoy	Head On			
Environment	Distance	Profile	Reflector Value	Edge
Real-World	48"	14-100 (avg. 25.5); 774 pts.	100 (avg. 100); 97 pts.	18-70 (avg. 50); 114 pts.
Simulated	48"	13-102 (avg. 30)	88-130 (avg. 100)	37-83 (avg. 60)

When comparing the Green Taylor Buoy in the real-world environment to the simulated environment based on intensity range, the results in Table 26 show that the profile's minimum simulated value is 7.14% less than the real value, and the maximum simulated intensity value is 2% greater. The average real-world profile intensity value is 15% less than the average simulated intensity value. The reflector value range varies from 102-130 compared to the consistent 100. The average simulation intensity value compared to the average real-world intensity value has 0% error. The edge minimum value is 51% greater than the real-world edge intensity while the maximum value is 16% greater than the real-world maximum intensity. The average distribution of intensity values for the edge of the simulated image is 60, which is 20% greater than the real-world average intensity value 50.

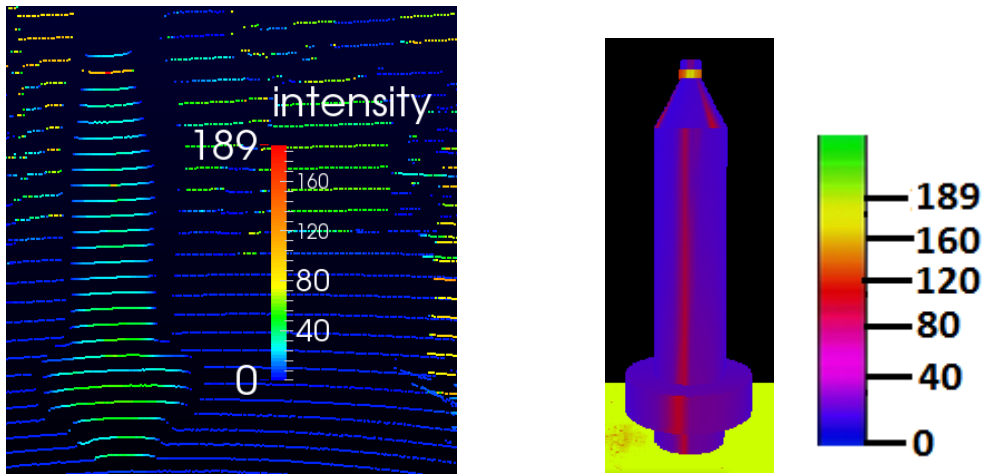


Figure 72 Intensity Data of the Red Taylor Buoy read from Velodyne HDL-32E Lidar, accompanied by the intensity spectrum scale using VeloView (Left). In comparison, the simulated Red Taylor Buoy (Right) shows the simulated intensity values accompanied by its intensity spectrum scale.

Table 27: Intensity Distribution for Red Taylor Buoy Sections

Red Buoy	Head On			
Environment	Distance	Profile	Reflector Value	Edge
Real-World	61"	20-100 (avg. 50); 434 pts.	97-189 (avg. 109); 22 pts.	15-37 (avg. 26); 57 pts.
Simulated	61"	20-100 (avg. 49)	99-123 (avg. 109)	19-57 (avg. 28)

The Red Taylor Buoy in the real-world environment compared to the simulated environment based on intensity range in Table 27 reveals that the profile's simulated range of 20-70 is within the real-world range of 20-100. The minimum real-world value has 0% difference from the simulated value, and the maximum simulated intensity value is 30% less than the real-world maximum intensity. The reflector value range varies from 99-123, which is within the range of 97-189. The simulated minimum value has 2.1% error compared to the reflector's real-world minimum intensity, and the maximum simulated value has 35% error from the maximum real-world intensity. The averages, however, are the same with an intensity value of 109 since the majority of the intensity points for the real-world environment were 100 in intensity value. The

edge's real-world minimum value is 21% less than the simulated edge intensity while the maximum value is 35% less than simulated maximum intensity. The real-world average edge intensity is 7.1% less than the simulated average edge intensity.

### WAM-V in Marine Environment Simulation:

The Velodyne HDL-32E Lidar and the buoy obstacles are transferred to the marine environment for testing of detection, distance values and intensities.

3D WAM-V Model (Kenney 2014) Converted and Modified to Environment in V-REP:

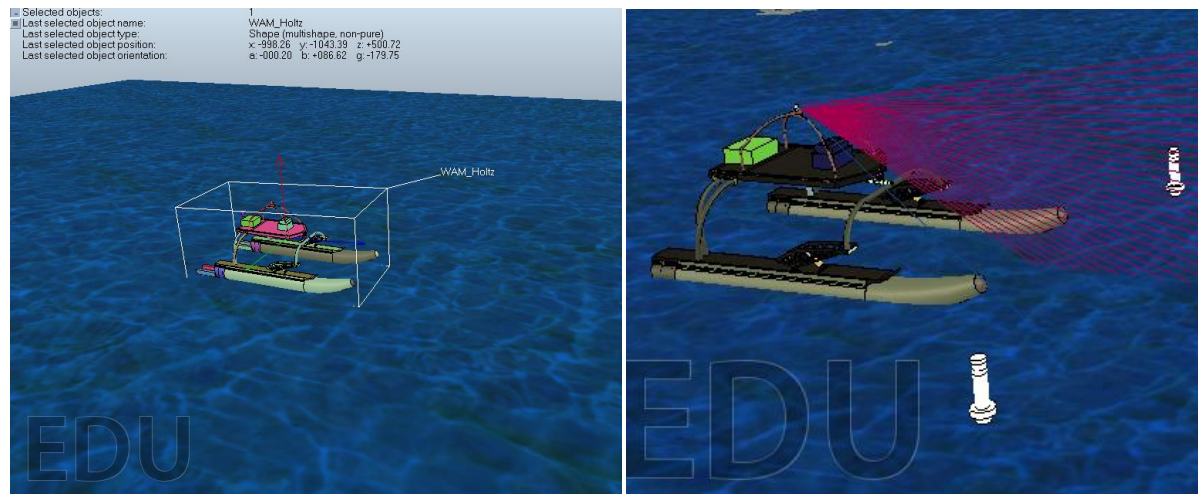


Figure 73 WAM-V vehicle integrated into V-REP environment with generated marine scene

The WAM-V CAD model is transferred into V-REP Pro as a series of parts to be modified with desired physical properties. These parts are grouped together, reconstructing the the entire vehicle into a single unit. As displayed in Figure 73, the transferred WAM-V model rests on the water consisting of three textures based on wave size, velocity, and amplitude. The Velodyne HDL-32E Lidar mounts on top of the payload tray.

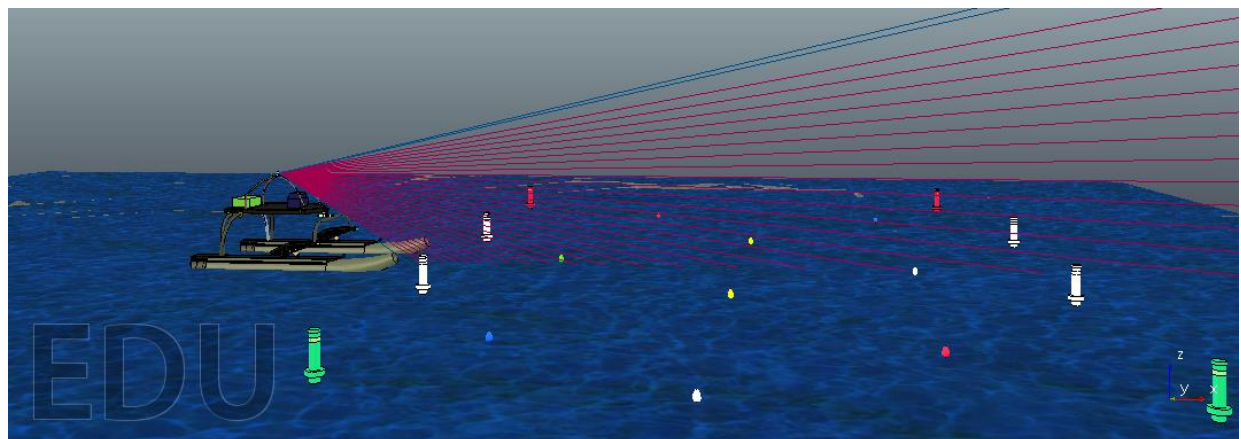


Figure 74 WAM-V marine vehicle in marine environment with obstacles



The WAM-V with the Velodyne HDL-32E Lidar in Figure 74 is positioned in front of an obstacle course setup similar to RobotX's Task 5 Obstacle Course. The purpose of the setup is to detect the distances and intensities for the buoys in the obstacle course.

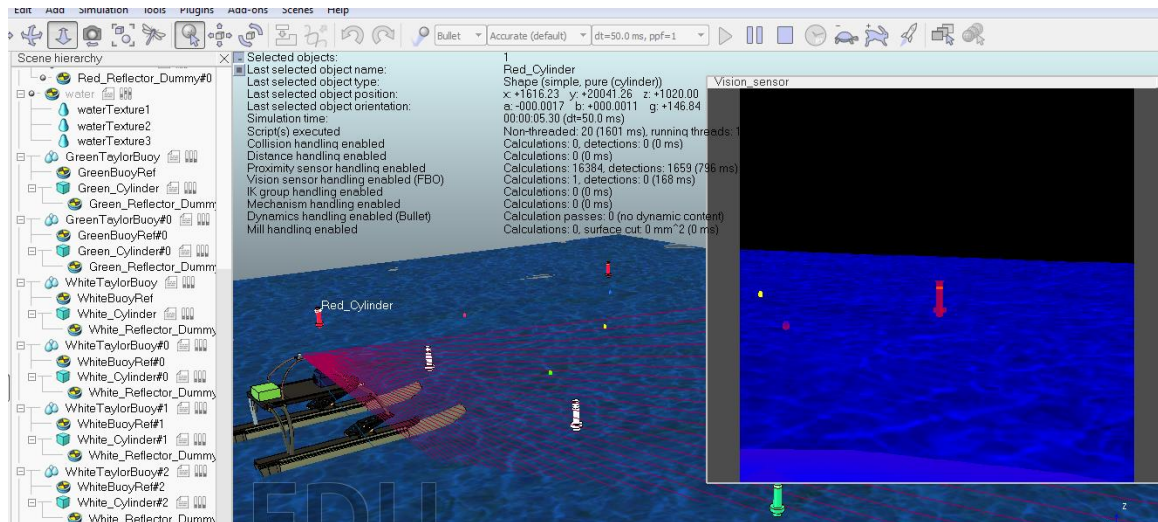


Figure 75 Velodyne HDL-32E Lidar mounted on WAM-V in Marine Environment detecting Obstacles and returning parameters, including Distance and Intensity (as demonstrated in Floating View)

The Velodyne Lidar detects the Green Taylor Buoy in Figure 75 and indicates the intensity range for the buoy the floating window. The water, however, shows return values in the intensity window. The intensity properties for the water are adjusted for zero return so the Lidar does not return intensity values for water, as shown from the real-world tests (Figure 51, Table 25).

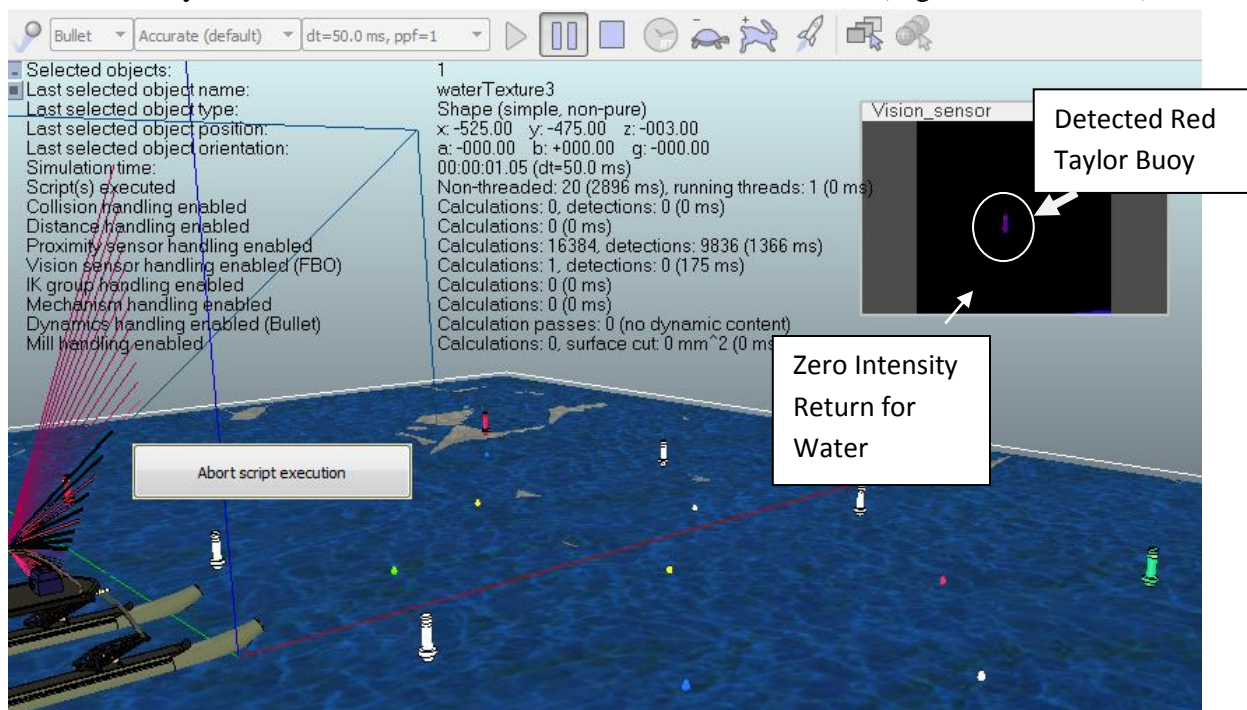


Figure 76 Velodyne HDL-32E Lidar mounted on WAM-V in Marine Environment while detecting obstacles but receiving minimal detection return from water because of Water Texture Properties



## Chapter 5: Conclusion

In conclusion, the characteristics of the Velodyne HDL-32E are tested and analyzed so that input parameters and error corrections could be implemented into the simulated model of the Velodyne HDL-32E integrated with the WAM-V vehicle. With these corrected parameters, the Velodyne HDL-32E scans for variable colored obstacles within a marine environment.

The distance parameter is analyzed for each of the lasers within the Velodyne HDL-32E Lidar. Referring to the data and based on the manual statement that up to 32 lasers are used, at least 29 lasers are actively used and corrected for within the Lidar during the testing periods. Third-degree polynomial correction equations are developed to take the input of the distance values read from the Lidar and output the corrected value closest to the actual distance of the detected objects within a range of .5m to 70m. To this extent, the data reveals that the Lidar cannot detect anything closer than .5m and objects closer than this limit to the lasers the lasers will appear as a gap within the point cloud.

The second parameter referred to as vertical correction is based on the vertical angular position of the each of the lasers distributed over the vertical field of view of the laser. Though the manual claims the lasers have a field of 40 degrees, the calculated field of view with a single sample spans about 41.5 degrees, but on average calculates to be 40 degrees. Part of this estimated 1.5 degree variation, however, may be due to error in the distance parameter as reported by the Velodyne HDL-32E and minimized using the distance correction. Still, in determining the overall position correction equations, the vertical correction of each one of the lasers does not need to be adjusted.

A final error correction equation for each laser is developed to successfully convert Lidar distance data into correct, real-world measurements and positions. The Velodyne HDL-32E Lidar within the simulation integrates these equations into the detection process of its child script coding and outputs the original distance, the error distance, and the corrected distance in an output window.

The deviations from the standard deviation  $\sigma = 0.0221$  m for the real-world uncorrected and corrected data are calculated for each of the 32 lasers in the Velodyne HDL-32E Lidar detecting the Red Taylor Buoy at a .518 m distance. The real-world uncorrected distance readings have a deviation of  $-1.02E-05 \sigma$  to  $.171\sigma$ . The corrected distance readings deviate from  $1.43E-07\sigma$  to  $0.0931\sigma$ , showing a 45.6%-98.6% reduction in deviation from the standard deviation compared to the uncorrected distances.

For the Red Taylor Buoy at a .518 m distance, the simulated uncorrected distance readings have a deviation of  $-0.411\sigma$  to  $2.77\sigma$  from the standard deviation of  $\sigma = 0.0208$  m. The corrected distance readings in simulation deviate from  $-.218\sigma$  to  $2.24\sigma$  and show a reduction in deviation from the standard deviation compared to the uncorrected distances.

In addition to the Velodyne HDL-32E parameter analysis and corrections, the obstacles for the course must be analyzed and tested to understand how the Lidar perceives the obstacles. Intensity profiles are produced via comparison of measured reflectivity and intensity. The Lidar produces intensity values based off the intensity values of the laser beams bouncing off the obstacles and returning to the sensor. Each intensity and associated reflectivity value reveals the dependency on material composition, surface area, geometry, distance, and lighting. As a result, these objects produce intensity and reflectivity ranges depending on the material.

While it is clear to discern reflector and edge parts of the buoy, discerning a red buoy from a green buoy solely based on intensity range rather than intensity and geometrical differences as detected by the buoy proves to be difficult. The Red Taylor Buoy's reflector returns a maximum consistent intensity value of 189 compared to the Green Taylor Buoy's intensity of 100. The area of the Red Taylor Buoy's reflector is also smaller than the Green Taylor Buoy's because of the red buoy's triangular top compared to the green buoy's rectangular top section. Therefore, for distances within 3m, the Red Taylor Buoy could be detected because of its higher intensity, color return on the spectrum scale, and smaller area when comparing it with the Green Taylor Buoy. For distances greater than 3m, the Green Taylor Buoy returns a wider and higher upper limit range of intensity values.

In a static position, the profiles are fairly constant and a slight variation in range can isolate the colors, but since the buoys will be in motion in the water, the ranges vary too much to be reliable. Lighting conditions also contribute to the intensity detection discernment. The range variation clearly indicates black can be properly isolated from white. Both black and white can be isolated from colored obstacles and for the light pattern tower when distinguishing the beginning of each light pattern sequence.

The Green Taylor Buoy in the real-world has a profile range of 14-100 whereas the simulated buoy has a range of 13-102. The reflector value of the real-world levels at 100, but the simulated version ranges from 88-130. The edge values for the real-world are within the range of 18-70, while the simulated environment returns 37-83, with the average of the points being 60, which is within the real-world range. The Red Taylor Buoy in the real-world environment returns an intensity range of 20-100 while the profile's simulated range of 20-70 is within the real-world range. The minimum real-world value is 0% less than the simulated value, and the maximum simulated intensity value is 30% less than the real-world maximum intensity. The real-world red reflector's minimum value is 2.1% greater than the reflector's simulated minimum intensity, and the maximum simulated value has 35% error from the maximum real-world intensity. The averages have the same intensity value of 109 because of point distribution. The buoy edge's real-world minimum value is 21% less than the simulated edge intensity while the maximum value is 35% less than simulated maximum intensity. While the simulated range does not span the entire real-world range, the real-world average edge intensity is 7.1% less than the simulated average edge intensity.



When comparing the collected data of the Lidar in the lab, the corrected data for simulation, and the real-world data on the Velodyne HDL-32E mounted on the WAM-V vehicle, the results look promising. The real-world data collected from the Lidar in the lab is within 2% error of the simulated distances. The corrected real-world data is within 8.7% error from the simulated distance, with the maximum error produced by Laser #27's distance outputs. By using step functions, Laser #27's simulated corrected distance reduces to 2.45% more than the real-world corrected distance. The real-world data of the Velodyne HDL-32E closely matches the profile range values developed for the buoys in the simulation obstacle course.

Given more time and budget, the simulation would have been developed to implement all of the sensors for the WAM-V vehicle, as well as the kinematics of the vehicle itself being compared with real-world data. The development of buoy profiles for identification would also have included other buoys made of the materials listed in the buoy material analysis section.

The orientation, angular resolution, and depth spreading of the lasers can also be analyzed in more depth with physical tests and correction procedures. While tests were conducted to measure angular resolution and accuracy for the Velodyne HDL-32E's analysis within this paper, more rigid procedures for measuring such values were deemed necessary.

With completion of the WAM-V vehicle sensor suite in the simulation environment, control optimization could be conducted by studying optimal path planning for obstacle detection and avoidance on the dynamic mobile marine vehicle. The sensor suite from there could use this paper's research and the control optimization to detect and identify isolated textural features of objects and select from a library of responses to avoid or approach obstacles.

For these considerations, the work in this thesis provides the base platform of understanding the Lidar theory, real-world error measurements, error correction, material reflectivity analysis, and a simulation platform for testing these aspects for obstacle detection. The theory discusses operation, sources of error, and error correction methods. The error corrections successfully improve the real-world measured distances and the simulated distances. The simulated Taylor Buoys portray a fairly close match to the real-world buoys when detecting distance and intensity based on material surface tests. All of these separate aspects allow for integrating the Velodyne HDL-32E Lidar onto the WAM-V vehicle for testing an obstacle course in a marine environment.

## References

- Atanacio-Jiménez, Gerardo, et al. "LIDAR Velodyne HDL-64E Calibration using Pattern Planes." *International Journal of Advanced Robotic Systems* 8.5 (2011). Web.
- a. T. M. Hans E. Jorgensen, et al., "Lidar calibration experiments.," *Applied Physics B Lasers and Optics.*, vol. 64, pp. 355-361, 1997.
- Berkoff, Timothy A., et al. "- Analytically Derived Thermal Correction to Reduce Overlap Bias Errors in Micro-Pulse Lidar Data." - 5984.- (- 2005): - 59840R. Web. Burba, George. *Eddy Covariance Method for Scientific, Industrial, Agricultural and Regulatory Applications: A Field Book on Measuring Ecosystem Gas Exchange and Areal Emission Rates.* : LI-COR Biosciences, 2013. Print.
- Canadian Coast Guard. "The Canadian Aids to Navigation System 2011: Floating Aids to Navigation (Buoys)." Government of Canada (2011). Web. November 2013.
- Cuerva, Alvaro and Angel Sanz-Andrés. "On Sonic Anemometer Measurement Theory." *Journal of Wind Engineering and Industrial Aerodynamics* 88.1 (2000): 25-55. Web.
- "Dan Buoy." *Merriam-Webster.com*. Merriam-Webster, n.d. Web. November 2013.
- DiGiacomo, Ronald W. "Understanding Electromagnetic Flowmeters." *Chemical Engineering Progress* 106.5 (2010): 42-47. *ProQuest Central*. Web  
<<http://search.proquest.com.ezproxy.libproxy.db.erau.edu/docview/221531794?accountid=27203>>.

Dynalab Corp, Inc. "Plastic Properties of Acrylonitrile Butadiene Styrene (ABS)." 2013. Web. March 2014, 2014.

"Eddy Covariance.", April 2014. Web. September, 2014.

Elgar, Steve, Britt Raubenheimer and R. T. Guza. "Current Meter Performance in the Surf Zone." *Journal of Atmospheric and Oceanic Technology* 18.10 (2001): 1735-1746. *ProQuest Central*. Web  
<<http://search.proquest.com.ezproxy.libproxy.db.erau.edu/docview/222489324?accountid=27203>>.

Filmetrics, Inc. "Refractive Index of Polyethylene, PE, Polyethene.", 2014. Web. April 2014, 2014.

Gash, J. H. C. and A. J. Dolman. "Sonic Anemometer (Co)Sine Response and Flux Measurement: I. the Potential for (Co)Sine Error to Affect Sonic Anemometer-Based Flux Measurements." *Agricultural and Forest Meteorology* 119.3–4 (2003): 195-207. Web.

Glennie, Craig. "Rigorous 3D Error Analysis of Kinematic Scanning LIDAR Systems." *Journal of Applied Geodesy* 1.3 (2007): 147-157. Web.

"Rigorous 3D Error Analysis of Kinematic Scanning LIDAR Systems." *Journal of Applied Geodesy* 1.3 (2007): 147-157. Web.

Greenwald, Doug. "Retroreflectors." *Redbubble Pty. Ltd* (2014). Web. October 2014.

- Grelle, A. and A. Lindroth. "Flow Distortion by a Solent Sonic Anemometer: Wind Tunnel Calibration and its Assessment for Flux Measurements Over Forest and Field." *Journal of Atmospheric and Oceanic Technology* 11.6 (1994): 1529-1542. Web.
- Halterman, Ryan and Michael Bruch. "Velodyne HDL-64E Lidar for Unmanned Surface Vehicle Obstacle Detection." (2010): 76920D-76920D-8. Web.
- Kennedy, Christopher. "WAM-Holtz CAD." (2014).
- Kurniawati, Hanna, et al. "Infrastructure for 3D Model Reconstruction of Marine Structures." (2011). Web.
- Lee, Kwang Wee, et al. "Tracking Random Finite Objects using 3D-LIDAR in Marine Environments." (2010): 1282-1287. Web.
- Levinson, Jesse and Sebastian Thrun. "Unsupervised Calibration for Multi-Beam Lasers." (2014): 179-193. Web.
- M. a. F. Antone, Y., "Fully automated laser range calibration.," *British Machine Vision Conference(BMVC)*. Warwick, UK. , 2007.
- Microsoft. "LifeCam Cinema." Microsoft Hardware (2014). Web.
- Moh, Wung Hee and Pei Lin Su. "Marina Barrage – A Unique 3-in-1 Project in Singapore." *Structural Engineering International* Volume 19.Number 1 (2009). Print.
- Muhammad, Naveed and Simon Lacroix. "Calibration of a Rotating Multi-Beam Lidar." (2010): 5648-5653. Web.

- N. J. Chen Y.D., Wu S.M., "In Dynamic calibration and compensation of a 3D laser radar scanning system," *Robotics and Automatization*, vol. 3, pp. 652-658, 1993.
- Nakai, Taro and Kou Shimoyama. "Ultrasonic Anemometer Angle of Attack Errors Under Turbulent Conditions." *Agricultural and Forest Meteorology* 162–163.0 (2012): 14-26. Web.
- Nautical Know How, Inc. "Boating Basics Online Chapter 6: Operations: Aids to Navigation.", 2012. Web. February, 2014.
- Nakai, Taro, et al. "Correction of Sonic Anemometer Angle of Attack Errors." *Agricultural and Forest Meteorology* 136.1–2 (2006): 19-30. Web.
- National Geospatial-Intelligence Agency (NGA) Standardization Document: Light Detection and Ranging (LIDAR) Sensor Model Supporting Precise Geopositioning, Version 1.1, August 1, 2011.
- Odenwald, Dr Sten. "Space Math @ NASA: Identifying Materials by their Reflectivity.", 2014. Web. March, 2014.
- Pahlow, Markus and Marc B. Parlange. "3-D Sonic Anemometer Standard Operating Procedure (SOP) for the Baltimore PM Supersite." *Johns Hopkins University, Department of Geography and Environmental Engineering, Baltimore MD* (2001). Web.
- Pandey, Gaurav, et al. "Automatic Targetless Extrinsic Calibration of a 3D Lidar and Camera by Maximizing Mutual Information." (2012). Web.

"Part 3| Classes of Materials: 3.3 Polymers." Ed. Martienssen, Werner, Warlimont, Hans (Eds.).

*Springer Handbook of Condensed Matter and Materials Data.*: Springer, 2005. Print.

Paschotta, Dr Rüdiger. "Hermite–Gaussian Modes." 2014. Web. April, 2014.

P. B. a. T. M. a. R. M. Peter Stone, "DARPA Urban Challenge," *Austin Robot Technology*. June 2007.

J. Bohren, Foote, T. B., Keller, J., Kushleyev, A., Lee, D., Stewart, A. D., Vernaza, P., Derenick, J., Spletzer, J., and Satterfield, B., "Little ben: The ben franklin racing team's entry in the 2007 DARPA urban challenge.," *Journal of Field Robotic.*, vol. 25(9), pp.598-614, 2008.

Robotics Association at Embry-Riddle. "RAER Autonomous Systems: Vehicle Sensors." 2014. Web. October 2014.

RobotX. "Maritime RobotX Challenge Preliminary Rules and Task Descriptions." Web. April 11, 2014.

San Diego Plastics, Inc. "Polyethylene.", 2010. Web. April 2014, 2014.

Schmid, Keil, et al. "Lidar 101: An Introduction to Lidar Technology, Data, and Applications." *NOAA Coastal Services Center* (2008). Web.

Sealite Pty Ltd. "IALA Maritime Buoyage System- Sealite Pty Ltd." 2010. Web. November 2013.

Seattle Marine & Fishing Supply Co. "Polyform Fenders and Buoys: Polyform A Series Buoys.", 2014. Web. February, 2014.

- Sheehan, Mark, Alastair Harrison and Paul Newman. "Self-Calibration for a 3D Laser." *The International Journal of Robotics Research* 31.5 (2012): 675-687. Web.
- Sorrell, F. Y., T. B. Curtin and M. D. Feezor. "An Electromagnetic Current Meter-Based System for Application in Unsteady Flows." *Oceanic Engineering, IEEE Journal of* 15.4 (1990): 373-379. Web.
- Sparton. "PHOD-1 Hydrophone: Specifications." *Sparton Navigation and Exploration* (2014). Web.
- Svelto, Orazio, ed. *Principles of Lasers*. : Springer, 2010. Print.
- "Ultrasonic Anemometer Angle of Attack Errors Under Turbulent Conditions." *Agricultural and Forest Meteorology* 162–163.0 (2012): 14-26. Web.
- U.S. Consumer Product Safety Commission. "Final Bike Report for ECOSA: Bicycle Reflector Project Report.", 1996. Web. February, 2014.
- van der Molen, M. K., J. H. C. Gash and J. A. Elbers. "Sonic Anemometer (Co)Sine Response and Flux Measurement: II. the Effect of Introducing an Angle of Attack Dependent Calibration." *Agricultural and Forest Meteorology* 122.1–2 (2004): 95-109. Web.
- Velodyne Lidar. "User's Manual and Programming Guide: HDL-32E High Definition LiDAR Sensor.", Nov. 2012. Web. April, 2014.
- VEX Robotics. "Instruction Sheet- Light Sensor." Web. August 2014.
- Wang Yue-ming and Kong Ling-fu. "The Study on the Effect of Virtual Current Distribution in an Electromagnetic Flow Meter with Bubble." (2011): 885-887. Web.

Yan Yi, Wu Hongping and Wu Huifeng. "Exciting Frequency Optimization for Electromagnetic Flow Meter with Genetic Algorithm." (2007): 1-5. Web.

Zhang, Xiao-Zhang and Yantao Li. "Calculation of the Virtual Current in an Electromagnetic Flow Meter with One Bubble using 3D Model." *ISA transactions* 43.2 (2004): 189-194. Web.



## Appendix

### Velodyne Test Plan for Calibration Errors

These tests analyze the physical properties of the Velodyne HDL-32E Lidar and the obstacles to generate error models, error correction, and physical profiles for simulation to match real-world data. The primary test locations are the Robotics & Unmanned Systems Lab and the Halifax River. The tests were conducted using the Velodyne Lidar HDL-32E, a series of buoys, retroreflectors, kiln dried pine, a black trash can, aluminum, polycarbonate, PVC, and a 95 7/8" wooden plank.

#### Primary Items Under Test:

The Velodyne HDL-32E Lidar is a "small and ruggedly built" sensor with 5.9" high and 3.4" diameter for dimensions and weighs less than 2 kg. The sensor has 32 laser detector pairs that are Class 1 905nm lasers with a range of 1-80 m. The sensor has a 360 degree horizontal FOV with a +10.67 to -30.67 degree (total of 40 degree) vertical FOV. The operating temperature is -10 - +60 C and the storage temperature is -40-+105 C. The degree of accuracy is <2cm (one sigma at 25 m) along with a vertical angular accuracy of 1.33 degrees. The HDL-32E Lidar withstands a max shock of 500 m/s<sup>2</sup> amplitude for an 11 ms duration, and can handle 5Hz-2000Hz vibration for 3G rms. The sensor outputs a maximum of 700,000 points/sec. The output UDP (User Datagram Protocol) packets contain distances, calibrated reflectivities, and rotation angles. The Lidar uses internal MEMS accelerometers and gyros for six-axis motion correction to output orientation and also uses a GPS Receiver for GPS time-synchronization.

#### Primary Supporting Items

- Lidar Mount
- Camera
- Ground support equipment
- Roboboat
- Computer with Software (VeloView)
- Flat object surfaces:
  - Varying materials with known reflectivities
  - Varying colors
- Non-flat objects:
  - Varying geometries with known reflectivities
  - Varying colors

### Test Description:

Description: The purpose of this test is to discern the physical properties of the Lidar and the reliability of its data. This information will be used to model and correct the data accordingly.

The following system features will be quantitatively evaluated during test plan execution:

- Detection Range
  - (Valid Data Range- Claim 5 cm to 70m)
  - Minimum accurate range return (less than one sigma)
  - Maximum accurate range return (less than one sigma)
  - Returned values outside of these boundaries
  - Precision of range
- Field of view
  - 360 degree horizontal FOV with a +10.67 to -30.67 degree (total of 40 degree) vertical FOV
- Reflectivities
  - Accuracy of materials' known reflectivity number
    - Use light sensor or Color light sensor
    - Use known reflectivity materials
    - Normalize Data with Retroreflector
    - Create profiles from examples
    - Compare profile with measured data from lidar
  - Use test objects at each distance in range testing for variation of reflectivity
    - Create reflectivity profile for each material based on range
  - Response to variable lighting conditions (Intensity)
  - Response to variable material for obstacles (Intensity)
- Accuracy
  - Claim: angular precision is 1/100 of a degree and should repeat to this accuracy; Device isn't calibrated for angular accuracy.
  - Quantitative value of angular accuracy
  - Quantitative value of angular precision
  - Repeatability of accuracy when mounted
  - Repeatability of accuracy when removed and remounted
  - Dependency on material
  - Noise: Dependency on environment (static and dynamic)
- Angular resolution
  - Quantitative value of angular resolution
  - Dependency on material
  - Dependency on environment (static and dynamic)
- Depth Spread
  - Claim: Laser spots aligned to within 1/2" of true position at 100 feet.

- No calibration of deflection (horizontal) or rotational angle necessary. Both horizontal angle and rotational laser angles always zero.
  - Vertical angle needs calibration (refer to XML file)
- Spot shape: rectangular shaped spot 4" wide by 2" tall at 100'
- At source: 1/2" wide by 1/4" tall, causing angular divergence to be 2.79 milliradians
- Quantitative measurement of depth spread within detection range
- Level of lidar data dependency on error
- Points/sec in environment
  - Point return in ground environment
  - Point return in marine environment
- Orientation
  - Return values from six axes (x, y, z along rotational, horizontal, and vertical angles)
- GPS time synchronization
  - Garmin GPS-18LV GPS receiver with 5 meter cable
  - 4.5 m Ethernet cable
  - HSL-32E with 3 meter cable terminated at interface box
- Shock and Vibration: (500 m/sec<sup>2</sup> amplitude, 11 ms duration shock and 3 Grms 5 Hz to 2000 Hz vibration)
  - Not going to be tested
- Sources of Error (Delete before final draft-use as reference by this section):
  - Two-way electromagnetic interference
    - GPS receivers
    - Radar induced noise in data (horizontal and vertical spreads)
  - UDP broadcast flooding
  - Calibration accuracy: 5 parameters (check drifting data points)
    - Depth spreading
    - Relative offsets

Test Plan: (Move to beginning of sect

#### 11. Test Detection Range on Ground

- a. Mount Lidar on Stable Platform
- b. Testing Detection Range
- c. Testing Point Cloud
- d. Testing FOV
- e. Testing Angular Resolution
  - i. Angular Resolution Claim: (vertical) 1.33 degrees
- f. Testing Accuracy <2 cm( one sigma at 25 m)
- g. Testing Reflectivity
- h. Points/sec in environment
- i. Testing Orientation

- j. Testing GPS time synchronization
- k. Testing UDP broadcast flooding
- l. Testing Calibration accuracy (Drifting Data Points)
  - i. Parameter 1
  - ii. Parameter 2
  - iii. Parameter 3
  - iv. Parameter 4
  - v. Parameter 5

## 12. Test Detection Range in Marine Environment

- a. Mount Lidar on Stable Platform
- b. Testing Detection Range
- c. Testing Point Cloud
- d. Testing FOV
- e. Testing Accuracy
- f. Testing Reflectivity (Intensity on Velodyne 32E: 0-255)
- g. Points/sec in environment (Ground Indoors, Ground and Marine Outdoors: Sunshine, Fog, and Rain)
- h. Testing Orientation
  - i. Calibrate Yaw, Pitch, and Roll
    - 1. Laser #9 from top of stack, DSR #15, is at 0 vertical angle
    - 2. Can use as reference to calibrate pitch and yaw of sensor relative to boat
- i. Testing GPS time synchronization
- j. Testing UDP broadcast flooding
  - i. HDL-32E outputs two separate broadcast UDP packets
  - ii. Use Wireshark to capture and observe
  - iii. Packet Details:
    - 1. 1206 byte payload with twelve 100 byte records and a 6 byte data area with GPS time stamping.
    - 2. Zero degree position is 90 degrees to right of interface cable when looking at bottom
    - 3. Each 100 byte record contains first a start identifier, a 2 byte rotational value, and 32 of 3-byte combinations that report info on each laser fired
      - a. 2 bytes report distance to nearest .2 cm
      - b. the remaining byte reports intensity on a scale of 0-255
  - iv. Calibration Info: Each HDL-32E fixed with respect to vertical angle
    - 1. Vertical correction factors used for each sensor issued data point to determine point's location
    - 2. HDL Source Example file on CD: Shows calculations used for correction factors-> same code in DSR to determine 3D locations

3. Plotting data: HDL Plotting Example on CD\_> look up Open GL
4. Use a timestamp for reference
- v. GPS Time Stamping Info:
  1. 6 bytes at end of HL-32E data packet for GPS timing
  2. 4 bytes: 32 bit unsigned integer time stamp (microseconds from top of hour to first laser firing in packet)
  3. 2 bytes: blank
  4. Accuracy Rules:
    - a. GPS unconnected: HdL-32E runs on own clock starting at midnight Jan 1 2000.
      - i. A drift of 5 seconds per day
      - ii. Date and time reflected in H, M , S, D, N, and Y data values
      - iii. HDL-32E clock does not correct for leap years
    - b. GPS connected:
      - i. \$GPRMC NMEA record in second data packets (Appendix B)
      - ii. GPS time synching in one of two modes:
        1. GPS has internal clock running for several weeks used first
        2. GPS achieves lock, HDL-32E clock within +/-50 microseconds of correct time
        3. GPS disconnected: HDL-32E continues own clock, drift of approximately 5 seconds per day
- vi. Laser Timing:
  1. GPS time stamps used: useful to determine exact firing time for each laser, allows for properly time-aligning HDL-32E point cloud with other data sources.
  2. Laser Firing Sequence
    - a. Laser Pairs: 1-16 with 17-32; Sequence: {0,16,1,17,...15,31}
- k. Testing Calibration accuracy (Drifting Data Points): Depth Spreading, Relative Offsets
  - i. Parameter 1
  - ii. Parameter 2
  - iii. Parameter 3
  - iv. Parameter 4
  - v. Parameter 5
- l. Thermal Testing
  - i. Take test data prior to temperature variation
  - ii. Stick Lidar in a Refrigerator (M-Building)

iii. Take test data quickly as it warms up (get a range)

13. Calibration Stage:

- a. Establish HDL-32E communication
- b. Create calibration table with db.xml data file
- c. Phase packets for rotation, distance, and intensity
- d. Apply calibration factors
- e. Plot or store data

## UDP Packet and Timing: Packet Offset Table

Packet Offset (bytes decimal)	Layer (DSR #)																																
	0	1	2	3	4	5	6	7	8	9	10	11	12	13	14	15	16	17	18	19	20	21	22	23	24	25	26	27	28	29	30	31	
0	543	541	540	539	538	537	536	535	534	533	532	531	530	529	528	526	525	524	523	522	521	520	518	517	516	515	514	513	511	510	509	508	507
160	-497	-495	-494	-493	-492	-491	-490	-488	-487	-484	-485	-484	-483	-482	-480	-479	-478	-477	-476	-475	-473	-472	-471	-470	-469	-468	-467	-465	-464	-463	-462	-461	
280	-450	-449	-448	-447	-446	-445	-444	-442	-441	-440	-439	-438	-437	-436	-434	-433	-432	-431	-430	-429	-427	-426	-424	-423	-422	-420	-419	-418	-417	-416	-415		
380	-404	-403	-402	-401	-400	-399	-397	-396	-395	-394	-393	-392	-391	-389	-388	-387	-386	-385	-384	-382	-381	-380	-378	-377	-376	-374	-373	-372	-371	-370	-369		
440	-358	-357	-356	-355	-354	-353	-351	-350	-349	-348	-347	-346	-344	-343	-342	-341	-340	-339	-338	-336	-335	-334	-333	-332	-331	-329	-328	-327	-326	-325	-324	-323	
540	-312	-311	-310	-309	-308	-306	-305	-304	-303	-301	-300	-298	-297	-296	-295	-294	-293	-291	-290	-289	-288	-287	-286	-285	-283	-281	-280	-279	-278	-276			
640	-266	-265	-264	-263	-262	-260	-259	-258	-257	-254	-255	-253	-252	-251	-250	-249	-248	-247	-245	-244	-243	-242	-241	-240	-238	-237	-236	-235	-234	-233	-232	-230	
740	-220	-219	-218	-217	-215	-214	-213	-212	-211	-210	-209	-207	-206	-205	-204	-203	-202	-200	-199	-198	-197	-196	-195	-194	-192	-191	-190	-189	-188	-187	-185	-184	
840	-174	-173	-172	-170	-169	-168	-167	-166	-165	-164	-162	-161	-160	-159	-158	-157	-156	-154	-153	-152	-151	-150	-148	-147	-146	-145	-144	-143	-142	-141	-139	-138	
940	-128	-127	-126	-124	-123	-122	-121	-120	-119	-118	-116	-115	-114	-113	-112	-111	-109	-108	-107	-106	-105	-104	-102	-101	-100	-99	-98	-97	-96	-94	-93	-92	
1040	-82	-81	-79	-78	-77	-76	-75	-74	-73	-71	-70	-69	-68	-67	-66	-65	-63	-62	-61	-60	-59	-58	-56	-55	-54	-53	-52	-51	-50	-48	-47	-46	
1100	-36	-35	-33	-32	-31	-30	-29	-28	-26	-25	-24	-23	-22	-21	-20	-18	-17	-15	-14	-13	-12	-10	-9	-8	-7	-6	-5	-3	-2	-1	0		

Detection Range Trial 2 Data Table:

Distances (ft)	Distances (m)	Laser 1 min	Laser 1 max	L2 min	L2 max	L3 min	L3 max	L4 min	L4 Max	L5 min	L5 max
1	0.518	0.528	0.5424			0.538	0.546			0.518	0.528
2	0.822	0.836	0.842			0.838	0.846			0.822	0.934
3	1.127	1.132	1.152			1.146	1.15			1.13	1.138
4	1.432	1.466	1.472			1.468	1.474			1.458	1.462
5	1.737	1.780	1.784			1.780	1.786			1.768	1.772
6	2.042	2.089	2.092			2.088	2.093			2.072	2.080
7	2.346	2.402	2.404			2.400	2.404			2.373	2.394
8	2.651	2.715	2.715			2.711	2.714			2.675	2.707
9	2.956	3.029	3.026			3.022	3.025			2.976	3.021
10	3.261	3.342	3.338			3.334	3.336			3.278	3.334
11	3.566	3.656	3.649			3.645	3.647			3.580	3.648
12	3.870	3.969	3.960			3.957	3.958			3.881	3.962
13	4.175	4.272	4.282			4.268	4.268			4.183	4.275
14	4.480	4.583	4.596			4.579	4.579			4.484	4.589
15	4.785	4.909	4.894			4.891	4.890			4.786	4.902
16	5.090	5.206	5.223			5.202	5.201			5.088	5.216
17	5.394	5.517	5.536			5.512	5.514			5.389	5.530
18	5.699	5.828	5.849			5.822	5.825			5.691	5.843
19	6.004	6.140	6.163			6.133	6.136			5.992	6.157
20	6.309	6.451	6.476			6.444	6.448			6.294	6.470
21	6.614	6.762	6.790			6.755	6.759			6.596	6.784
22	6.918	7.074	7.103			7.066	7.071			6.897	7.098
23	7.223	7.385	7.416			7.376	7.382			7.199	7.411

Distances (ft)	Distances (m)	L6 min	L6 max	L7 min	L7 max	L8 min	L8 max	L9 min	L9 max	L10 min	L10 max
1	0.518	0.554	0.562	0.512	0.528	0.576	0.582	0.522	0.532	0.558	0.564
2	0.822	0.874	0.902	0.822	0.826	0.894	0.924	0.826	0.848	0.898	0.906
3	1.127	1.194	1.242	1.128	1.134	1.24	1.262	1.132	1.136	1.222	1.238
4	1.432	1.514	1.582	1.450	1.456	1.588	1.604	1.452	1.458	1.564	1.576
5	1.737	1.834	1.922	1.762	1.768	1.932	1.940	1.762	1.770	1.904	1.908
6	2.042	2.154	2.262	2.073	2.075	2.268	2.281	2.071	2.075	2.237	2.246
7	2.346	2.474	2.602	2.386	2.386	2.608	2.621	2.381	2.383	2.572	2.582
8	2.651	2.794	2.942	2.697	2.699	2.949	2.960	2.692	2.692	2.908	2.917
9	2.956	3.114	3.282	3.008	3.012	3.290	3.300	3.000	3.002	3.244	3.253
10	3.261	3.434	3.622	3.319	3.324	3.630	3.640	3.309	3.313	3.580	3.589
11	3.566	3.754	3.962	3.630	3.637	3.971	3.979	3.618	3.624	3.916	3.925
12	3.870	4.074	4.302	3.941	3.950	4.311	4.319	3.926	3.934	4.251	4.261
13	4.175	4.394	4.642	4.252	4.263	4.652	4.658	4.235	4.245	4.587	4.596
14	4.480	4.714	4.982	4.563	4.576	4.993	4.998	4.543	4.555	4.923	4.932
15	4.785	5.034	5.322	4.874	4.888	5.333	5.338	4.852	4.866	5.259	5.268
16	5.090	5.354	5.662	5.185	5.201	5.674	5.677	5.161	5.177	5.595	5.604
17	5.394	5.674	6.002	5.496	5.514	6.014	6.017	5.469	5.487	5.930	5.940
18	5.699	5.994	6.342	5.807	5.827	6.355	6.356	5.778	5.798	6.266	6.275
19	6.004	6.314	6.682	6.118	6.140	6.696	6.696	6.086	6.108	6.602	6.611
20	6.309	6.634	7.022	6.429	6.452	7.036	7.036	6.395	6.419	6.938	6.947
21	6.614	6.954	7.362	6.740	6.765	7.377	7.375	6.704	6.730	7.274	7.283
22	6.918	7.274	7.702	7.051	7.078	7.717	7.715	7.012	7.040	7.609	7.619
23	7.223	7.594	8.042	7.362	7.391	8.058	8.054	7.321	7.351	7.945	7.954



Distances (ft)	Distances (m)	L11 min	L11 max	L12 min	L12 max	L13 min	L13 max	L14 min	L14 max	L15 min	L15 max
1	0.518	0.55	0.528	0.56	0.566	0.53	0.536	0.554	0.576	0.504	0.522
2	0.822	0.832	0.842	0.89	0.898	0.816	0.828	0.878	0.9	0.81	0.828
3	1.127	1.134	1.138	1.218	1.224	1.126	1.132	1.222	1.226	1.11	1.118
4	1.432	1.458	1.464	1.566	1.570	1.452	1.456	1.560	1.564	1.436	1.542
5	1.737	1.764	1.770	1.892	1.910	1.758	1.776	1.882	1.890	1.748	1.754
6	2.042	2.064	2.080	2.227	2.242	2.064	2.078	2.219	2.221	2.056	2.106
7	2.346	2.369	2.391	2.561	2.578	2.373	2.389	2.548	2.554	2.367	2.424
8	2.651	2.675	2.701	2.895	2.914	2.682	2.700	2.877	2.888	2.679	2.742
9	2.956	2.980	3.012	3.229	3.250	2.992	3.010	3.206	3.222	2.990	3.060
10	3.261	3.285	3.323	3.563	3.586	3.301	3.321	3.536	3.556	3.301	3.377
11	3.566	3.591	3.633	3.897	3.922	3.610	3.632	3.865	3.890	3.613	3.695
12	3.870	3.896	3.944	4.231	4.258	3.919	3.943	4.194	4.223	3.924	4.013
13	4.175	4.202	4.254	4.565	4.594	4.228	4.254	4.523	4.557	4.236	4.331
14	4.480	4.507	4.565	4.899	4.930	4.538	4.564	4.852	4.891	4.547	4.649
15	4.785	4.812	4.876	5.233	5.266	4.847	4.875	5.182	5.225	4.858	4.966
16	5.090	5.118	5.186	5.567	5.602	5.156	5.186	5.511	5.559	5.170	5.284
17	5.394	5.423	5.497	5.901	5.938	5.465	5.497	5.840	5.892	5.481	5.602
18	5.699	5.729	5.807	6.235	6.274	5.774	5.808	6.169	6.226	5.793	5.920
19	6.004	6.034	6.118	6.569	6.610	6.084	6.118	6.498	6.560	6.104	6.238
20	6.309	6.339	6.429	6.903	6.946	6.393	6.429	6.828	6.894	6.415	6.555
21	6.614	6.645	6.739	7.237	7.282	6.702	6.740	7.157	7.228	6.727	6.873
22	6.918	6.950	7.050	7.571	7.618	7.011	7.051	7.486	7.561	7.038	7.191
23	7.223	7.256	7.360	7.905	7.954	7.320	7.362	7.815	7.895	7.350	7.509

Distances (ft)	Distances (m)	L16 min	L16 max	L17 min	L17 max	L18 min	L18 max	L19 min	L19 max	L20 min	L20 max
1	0.518	0.552	0.558	0.522	0.53	0.548	0.558	0.538	0.548	0.542	0.546
2	0.822	0.868	0.888	0.82	0.832	0.874	0.88	0.838	0.846	0.852	0.882
3	1.127	1.198	1.206	1.122	1.124	1.194	1.198	1.132	1.14	1.172	1.194
4	1.432	1.524	1.546	1.450	1.448	1.524	1.534	1.460	1.476	1.520	1.524
5	1.737	1.844	1.858	1.758	1.764	1.846	1.852	1.770	1.792	1.834	1.838
6	2.042	2.169	2.189	2.065	2.065	2.171	2.177	2.073	2.096	2.160	2.165
7	2.346	2.493	2.514	2.373	2.375	2.496	2.501	2.382	2.408	2.485	2.487
8	2.651	2.817	2.840	2.682	2.685	2.820	2.825	2.691	2.719	2.810	2.810
9	2.956	3.141	3.166	2.990	2.996	3.145	3.150	2.999	3.031	3.135	3.132
10	3.261	3.465	3.492	3.298	3.306	3.469	3.474	3.308	3.343	3.460	3.455
11	3.566	3.789	3.818	3.607	3.616	3.794	3.798	3.616	3.655	3.786	3.778
12	3.870	4.113	4.143	3.915	3.926	4.119	4.122	3.925	3.967	4.111	4.100
13	4.175	4.437	4.469	4.224	4.236	4.443	4.446	4.234	4.278	4.436	4.423
14	4.480	4.761	4.795	4.532	4.547	4.768	4.771	4.542	4.590	4.761	4.745
15	4.785	5.085	5.121	4.840	4.857	5.092	5.095	4.851	4.902	5.086	5.068
16	5.090	5.409	5.447	5.149	5.167	5.417	5.419	5.159	5.214	5.412	5.391
17	5.394	5.733	5.772	5.457	5.477	5.742	5.743	5.468	5.526	5.737	5.713
18	5.699	6.057	6.098	5.766	5.787	6.066	6.067	5.777	5.837	6.062	6.036
19	6.004	6.381	6.424	6.074	6.098	6.391	6.392	6.085	6.149	6.387	6.358
20	6.309	6.705	6.750	6.382	6.408	6.715	6.716	6.394	6.461	6.712	6.681
21	6.614	7.029	7.076	6.691	6.718	7.040	7.040	6.702	6.773	7.038	7.004
22	6.918	7.353	7.401	6.999	7.028	7.365	7.364	7.011	7.085	7.363	7.326
23	7.223	7.677	7.727	7.338	7.308	7.688	7.689	7.320	7.396	7.688	7.649

Average Distance for Each Laser Data Table:

Distances (ft)	Distances (m)	L1	L2	L3	L4	L5	L6	L7	L8	L9
1	0.518	0.535		0.542		0.523	0.558	0.520	0.579	0.527
2	0.822	0.839		0.842		0.878	0.888	0.824	0.909	0.837
3	1.127	1.142		1.148		1.134	1.218	1.131	1.251	1.134
4	1.432	1.469		1.471		1.460	1.548	1.453	1.596	1.455
5	1.737	1.782		1.783		1.770	1.878	1.765	1.936	1.766
6	2.042	2.091		2.091		2.076	2.208	2.074	2.275	2.073
7	2.346	2.403		2.402		2.383	2.538	2.386	2.615	2.382
8	2.651	2.715		2.713		2.691	2.868	2.698	2.955	2.692
9	2.956	3.028		3.024		2.999	3.198	3.010	3.295	3.001
10	3.261	3.340		3.335		3.306	3.528	3.322	3.635	3.311
11	3.566	3.652		3.646		3.614	3.858	3.634	3.975	3.621
12	3.870	3.965		3.957		3.921	4.188	3.946	4.315	3.930
13	4.175	4.277		4.268		4.229	4.518	4.258	4.655	4.240
14	4.480	4.589		4.579		4.537	4.848	4.570	4.995	4.549
15	4.785	4.902		4.890		4.844	5.178	4.881	5.335	4.859
16	5.090	5.214		5.202		5.152	5.508	5.193	5.676	5.169
17	5.394	5.526		5.513		5.459	5.838	5.505	6.016	5.478
18	5.699	5.839		5.824		5.767	6.168	5.817	6.356	5.788
19	6.004	6.151		6.135		6.075	6.498	6.129	6.696	6.097
20	6.309	6.464		6.446		6.382	6.828	6.441	7.036	6.407
21	6.614	6.776		6.757		6.690	7.158	6.753	7.376	6.717
22	6.918	7.088		7.068		6.997	7.488	7.065	7.716	7.026
23	7.223	7.401		7.379		7.305	7.818	7.377	8.056	7.336

Distances (ft)	Distances (m)	L10	L11	L12	L13	L14	L15	L16	L17	L18	L19
1	0.518	0.561	0.539	0.563	0.533	0.565	0.513	0.555	0.526	0.553	0.543
2	0.822	0.902	0.837	0.894	0.822	0.889	0.819	0.878	0.826	0.877	0.842
3	1.127	1.230	1.136	1.221	1.129	1.224	1.114	1.202	1.123	1.196	1.136
4	1.432	1.570	1.461	1.568	1.454	1.562	1.489	1.535	1.449	1.529	1.468
5	1.737	1.906	1.767	1.901	1.767	1.886	1.751	1.851	1.761	1.849	1.781
6	2.042	2.241	2.072	2.234	2.071	2.220	2.081	2.179	2.065	2.174	2.085
7	2.346	2.577	2.380	2.569	2.381	2.551	2.396	2.504	2.374	2.498	2.395
8	2.651	2.913	2.688	2.904	2.691	2.883	2.710	2.829	2.684	2.823	2.705
9	2.956	3.249	2.996	3.239	3.001	3.214	3.025	3.154	2.993	3.147	3.015
10	3.261	3.584	3.304	3.574	3.311	3.546	3.339	3.479	3.302	3.472	3.325
11	3.566	3.920	3.612	3.909	3.621	3.877	3.654	3.803	3.611	3.796	3.636
12	3.870	4.256	3.920	4.244	3.931	4.209	3.969	4.128	3.921	4.120	3.946
13	4.175	4.592	4.228	4.579	4.241	4.540	4.283	4.453	4.230	4.445	4.256
14	4.480	4.928	4.536	4.914	4.551	4.872	4.598	4.778	4.539	4.769	4.566
15	4.785	5.263	4.844	5.249	4.861	5.203	4.912	5.103	4.849	5.094	4.876
16	5.090	5.599	5.152	5.584	5.171	5.535	5.227	5.428	5.158	5.418	5.187
17	5.394	5.935	5.460	5.919	5.481	5.866	5.542	5.753	5.467	5.742	5.497
18	5.699	6.271	5.768	6.254	5.791	6.198	5.856	6.078	5.777	6.067	5.807
19	6.004	6.607	6.076	6.589	6.101	6.529	6.171	6.403	6.086	6.391	6.117
20	6.309	6.942	6.384	6.924	6.411	6.861	6.485	6.728	6.395	6.716	6.427
21	6.614	7.278	6.692	7.259	6.721	7.192	6.800	7.052	6.704	7.040	6.738
22	6.918	7.614	7.000	7.594	7.031	7.524	7.115	7.377	7.014	7.364	7.048
23	7.223	7.950	7.308	7.929	7.341	7.855	7.429	7.702	7.323	8.056	7.358

Distances (ft)	Distances (m)	L20	L21	L22	L23	L24	L25	L26	L27	L28	L29	L30	L31
1	0.518	0.544	0.536	0.540	0.532	0.540	0.528	0.535	0.556	0.534	0.548	0.524	0.578
2	0.822	0.867	0.832	0.870	0.826	0.861	0.828	0.877	0.817	0.848	0.828	0.833	0.838
3	1.127	1.183	1.127	1.176	1.132	1.173	1.134	1.167	1.041	1.153	1.154	1.146	1.138
4	1.432	1.522	1.462	1.512	1.460	1.501	1.404	1.499		1.486	1.449	1.486	1.411
5	1.737	1.836	1.737	1.827	1.760	1.813	1.707	1.809	1.793	1.793	1.752	1.784	1.691
6	2.042	2.162	2.048	2.150	2.069	2.133	2.000	2.128	2.058	2.110	2.055	2.107	1.971
7	2.346	2.486	2.352	2.471	2.378	2.452	2.294	2.445	2.367	2.425	2.358	2.424	2.251
8	2.651	2.810	2.655	2.793	2.687	2.771	2.587	2.762	2.677	2.741	2.661	2.741	2.531
9	2.956	3.134	2.958	3.115	2.996	3.089	2.881	3.079	2.987	3.056	2.964	3.058	2.811
10	3.261	3.458	3.261	3.436	3.305	3.408	3.174	3.396	3.296	3.372	3.267	3.376	3.091
11	3.566	3.782	3.564	3.758	3.614	3.726	3.467	3.713	3.606	3.688	3.570	3.693	3.371
12	3.870	4.106	3.868	4.079	3.923	4.045	3.761	4.030	3.915	4.003	3.873	4.010	3.651
13	4.175	4.429	4.171	4.401	4.232	4.364	4.054	4.347	4.225	4.319	4.176	4.328	3.931
14	4.480	4.753	4.474	4.723	4.541	4.682	4.348	4.664	4.534	4.634	4.479	4.645	4.211
15	4.785	5.077	4.777	5.044	4.850	5.001	4.641	4.981	4.844	4.950	4.782	4.962	4.491
16	5.090	5.401	5.080	5.366	5.159	5.319	4.934	5.298	5.154	5.266	5.085	5.280	4.771
17	5.394	5.725	5.384	5.687	5.468	5.638	5.228	5.615	5.463	5.581	5.388	5.597	5.051
18	5.699	6.049	5.687	6.009	5.777	5.957	5.521	5.932	5.773	5.897	5.691	5.914	5.331
19	6.004	6.373	5.990	6.331	6.086	6.275	5.815	6.249		6.212	5.994	6.231	5.611
20	6.309	6.697	6.293	6.652	6.395	6.594	6.108	6.566	6.392	6.528	6.297	6.549	5.891
21	6.614	7.021	6.596	6.974	6.704	6.912	6.401	6.883	6.701	6.844	6.600	6.866	6.171
22	6.918	7.345	6.900	7.295	7.013	7.231	6.695	7.200	7.011	7.159	6.903	7.183	6.451
23	7.223	7.668	7.203	7.617	7.322	7.550	6.988	7.517	7.321	7.475	7.206	7.501	6.731

Error for Each Laser Data Table:

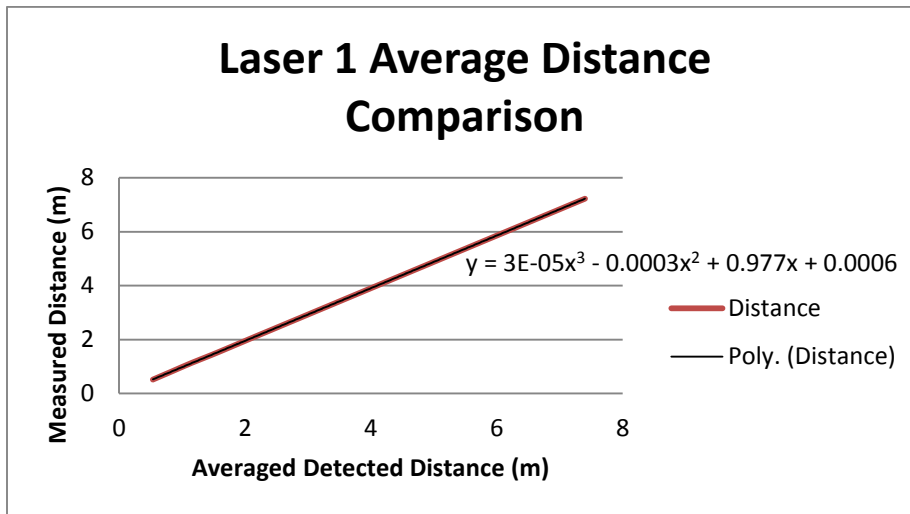
Distances (ft)	Distances (m)	L1	L2	L3	L4	L5	L6	L7	L8	L9	L10	L11
1	0.518	0.018		0.024		0.005	0.040	0.002	0.061	0.009	0.043	0.021
2	0.822	0.017		0.020		0.056	0.066	0.002	0.087	0.015	0.080	0.015
3	1.127	0.015		0.021		0.007	0.091	0.004	0.124	0.007	0.103	0.009
4	1.432	0.037		0.039		0.028	0.116	0.021	0.164	0.023	0.138	0.029
5	1.737	0.045		0.046		0.033	0.141	0.028	0.199	0.029	0.169	0.030
6	2.042	0.049		0.049		0.034	0.166	0.033	0.233	0.031	0.200	0.030
7	2.346	0.057		0.055		0.037	0.192	0.040	0.268	0.036	0.231	0.034
8	2.651	0.064		0.062		0.040	0.217	0.047	0.304	0.041	0.262	0.037
9	2.956	0.072		0.068		0.043	0.242	0.054	0.339	0.045	0.293	0.040
10	3.261	0.079		0.074		0.045	0.267	0.061	0.374	0.050	0.324	0.043
11	3.566	0.087		0.080		0.048	0.292	0.068	0.409	0.055	0.355	0.046
12	3.870	0.094		0.087		0.051	0.318	0.075	0.445	0.060	0.386	0.050
13	4.175	0.102		0.093		0.054	0.343	0.082	0.480	0.065	0.417	0.053
14	4.480	0.109		0.099		0.057	0.368	0.090	0.515	0.069	0.448	0.056
15	4.785	0.117		0.106		0.059	0.393	0.097	0.551	0.074	0.479	0.059
16	5.090	0.125		0.112		0.062	0.418	0.104	0.586	0.079	0.510	0.062
17	5.394	0.132		0.118		0.065	0.444	0.111	0.621	0.084	0.541	0.066
18	5.699	0.140		0.125		0.068	0.469	0.118	0.657	0.089	0.572	0.069
19	6.004	0.147		0.131		0.071	0.494	0.125	0.692	0.093	0.603	0.072
20	6.309	0.155		0.137		0.073	0.519	0.132	0.727	0.098	0.634	0.075
21	6.614	0.162		0.143		0.076	0.544	0.139	0.762	0.103	0.665	0.078
22	6.918	0.170		0.150		0.079	0.570	0.146	0.798	0.108	0.696	0.082
23	7.223	0.178		0.156		0.082	0.595	0.153	0.833	0.113	0.727	0.085

Distances (ft)	Distances (m)	L12	L13	L14	L15	L16	L17	L18	L19	L20	L21	L22
1	0.518	0.045	0.015	0.047	-0.005	0.037	0.008	0.035	0.025	0.026	0.018	0.022
2	0.822	0.072	0.000	0.067	-0.003	0.056	0.004	0.055	0.020	0.045	0.010	0.048
3	1.127	0.094	0.002	0.097	-0.013	0.075	-0.004	0.069	0.009	0.056	0.000	0.049
4	1.432	0.136	0.022	0.130	0.057	0.103	0.017	0.097	0.036	0.090	0.030	0.080
5	1.737	0.164	0.030	0.149	0.014	0.114	0.024	0.112	0.044	0.099	0.000	0.090
6	2.042	0.193	0.029	0.178	0.039	0.137	0.023	0.132	0.043	0.121	0.007	0.108
7	2.346	0.223	0.035	0.205	0.049	0.157	0.028	0.152	0.048	0.140	0.005	0.125
8	2.651	0.253	0.040	0.232	0.059	0.178	0.032	0.172	0.054	0.159	0.004	0.142
9	2.956	0.283	0.045	0.258	0.069	0.198	0.037	0.191	0.059	0.178	0.002	0.159
10	3.261	0.314	0.050	0.285	0.079	0.218	0.041	0.211	0.065	0.197	0.000	0.175
11	3.566	0.344	0.055	0.312	0.088	0.238	0.046	0.230	0.070	0.216	-0.001	0.192
12	3.870	0.374	0.061	0.338	0.098	0.258	0.050	0.250	0.075	0.235	-0.003	0.209
13	4.175	0.404	0.066	0.365	0.108	0.278	0.055	0.270	0.081	0.254	-0.004	0.226
14	4.480	0.434	0.071	0.392	0.118	0.298	0.059	0.289	0.086	0.273	-0.006	0.243
15	4.785	0.465	0.076	0.418	0.128	0.318	0.064	0.309	0.092	0.292	-0.008	0.259
16	5.090	0.495	0.081	0.445	0.137	0.338	0.068	0.328	0.097	0.312	-0.009	0.276
17	5.394	0.525	0.087	0.472	0.147	0.358	0.073	0.348	0.102	0.331	-0.011	0.293
18	5.699	0.555	0.092	0.499	0.157	0.379	0.077	0.368	0.108	0.350	-0.012	0.310
19	6.004	0.585	0.097	0.525	0.167	0.399	0.082	0.387	0.113	0.369	-0.014	0.327
20	6.309	0.616	0.102	0.552	0.177	0.419	0.086	0.407	0.119	0.388	-0.016	0.343
21	6.614	0.646	0.107	0.579	0.186	0.439	0.091	0.426	0.124	0.407	-0.017	0.360
22	6.918	0.676	0.113	0.605	0.196	0.459	0.095	0.446	0.129	0.426	-0.019	0.377
23	7.223	0.706	0.118	0.632	0.206	0.479	0.100	#REF!	0.135	0.445	-0.020	0.394

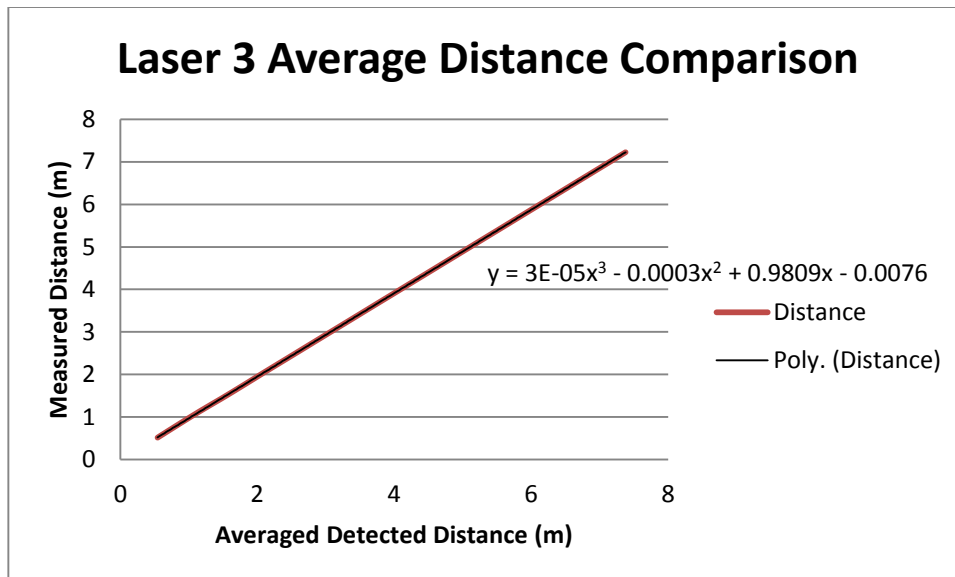
Distances (ft)	Distances (m)	L23	L24	L25	L26	L27	L28	L29	L30	L31
1	0.518	0.014	0.022	0.010	0.017	0.038	0.016	0.030	0.006	0.060
2	0.822	0.004	0.039	0.006	0.055	-0.005	0.026	0.006	0.011	0.016
3	1.127	0.005	0.046	0.007	0.040	-0.086	0.026	0.027	0.019	0.011
4	1.432	0.028	0.069	-0.028	0.067	-1.432	0.054	0.017	0.054	-0.021
5	1.737	0.023	0.076	-0.030	0.072	0.056	0.056	0.016	0.047	-0.045
6	2.042	0.027	0.092	-0.041	0.087	0.016	0.068	0.014	0.065	-0.070
7	2.346	0.032	0.106	-0.053	0.099	0.021	0.079	0.012	0.077	-0.095
8	2.651	0.036	0.119	-0.064	0.111	0.026	0.090	0.010	0.090	-0.120
9	2.956	0.040	0.133	-0.075	0.123	0.031	0.100	0.008	0.102	-0.145
10	3.261	0.044	0.147	-0.087	0.136	0.035	0.111	0.007	0.115	-0.169
11	3.566	0.048	0.161	-0.098	0.148	0.040	0.122	0.005	0.127	-0.194
12	3.870	0.053	0.175	-0.110	0.160	0.045	0.133	0.003	0.140	-0.219
13	4.175	0.057	0.188	-0.121	0.172	0.050	0.144	0.001	0.152	-0.244
14	4.480	0.061	0.202	-0.132	0.184	0.055	0.154	-0.001	0.165	-0.269
15	4.785	0.065	0.216	-0.144	0.197	0.059	0.165	-0.002	0.177	-0.293
16	5.090	0.069	0.230	-0.155	0.209	0.064	0.176	-0.004	0.190	-0.318
17	5.394	0.074	0.244	-0.167	0.221	0.069	0.187	-0.006	0.202	-0.343
18	5.699	0.078	0.257	-0.178	0.233	0.074	0.198	-0.008	0.215	-0.368
19	6.004	0.082	0.271	-0.189	0.245	-6.004	0.208	-0.010	0.227	-0.393
20	6.309	0.086	0.285	-0.201	0.258	0.083	0.219	-0.011	0.240	-0.417
21	6.614	0.090	0.299	-0.212	0.270	0.088	0.230	-0.013	0.252	-0.442
22	6.918	0.095	0.313	-0.224	0.282	0.093	0.241	-0.015	0.265	-0.467
23	7.223	0.099	0.326	-0.235	0.294	0.097	0.252	-0.017	0.277	-0.492

Correction for Each Laser:

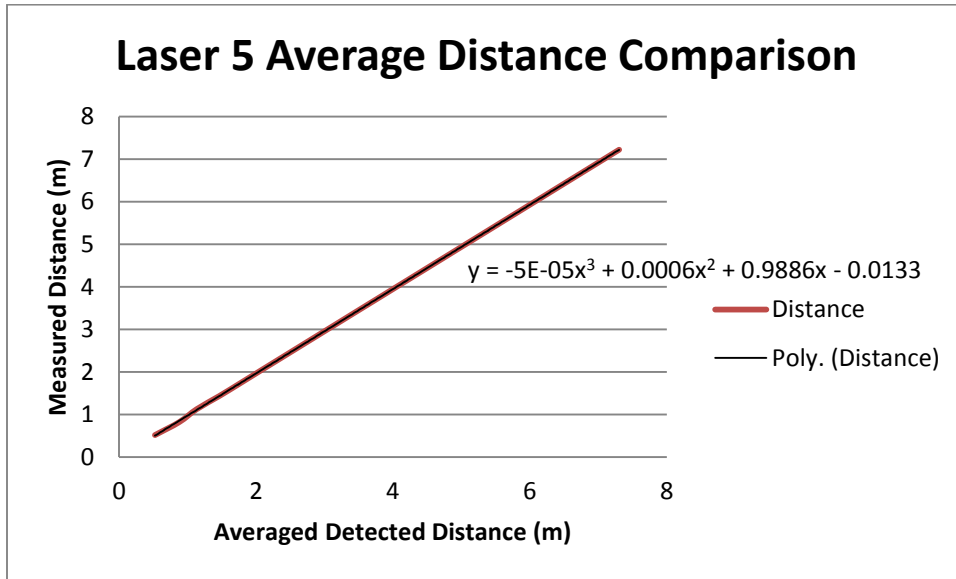
Laser 1:



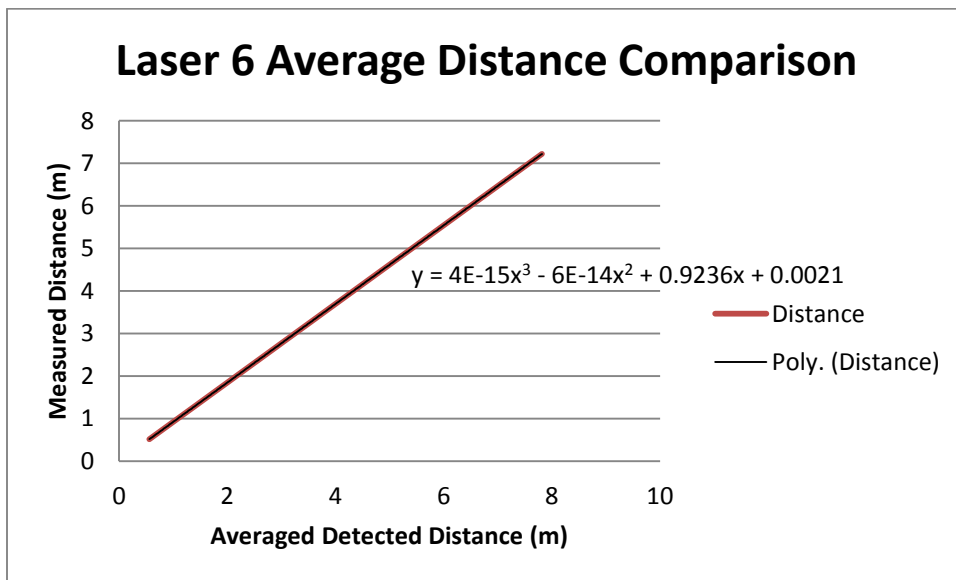
Laser 3:



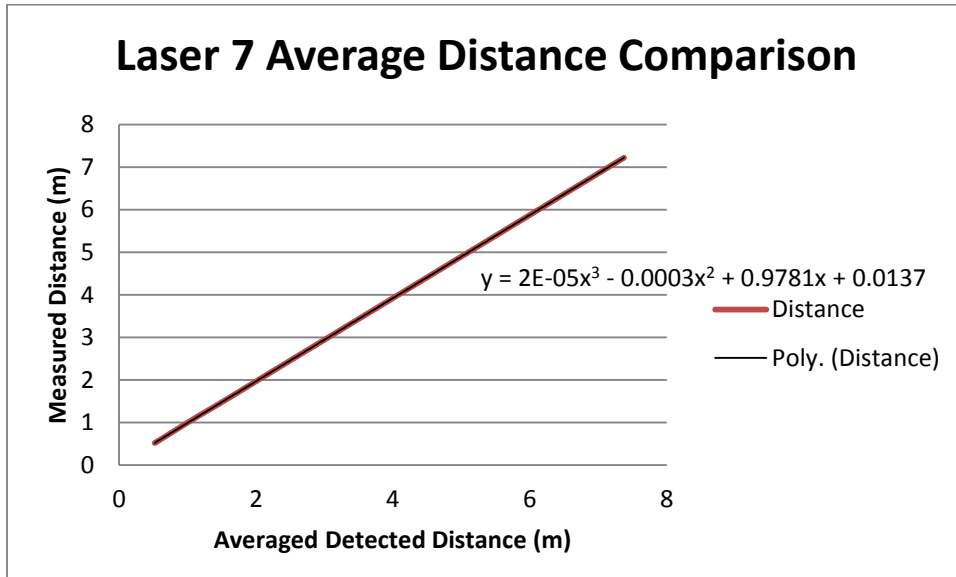
Laser 5:



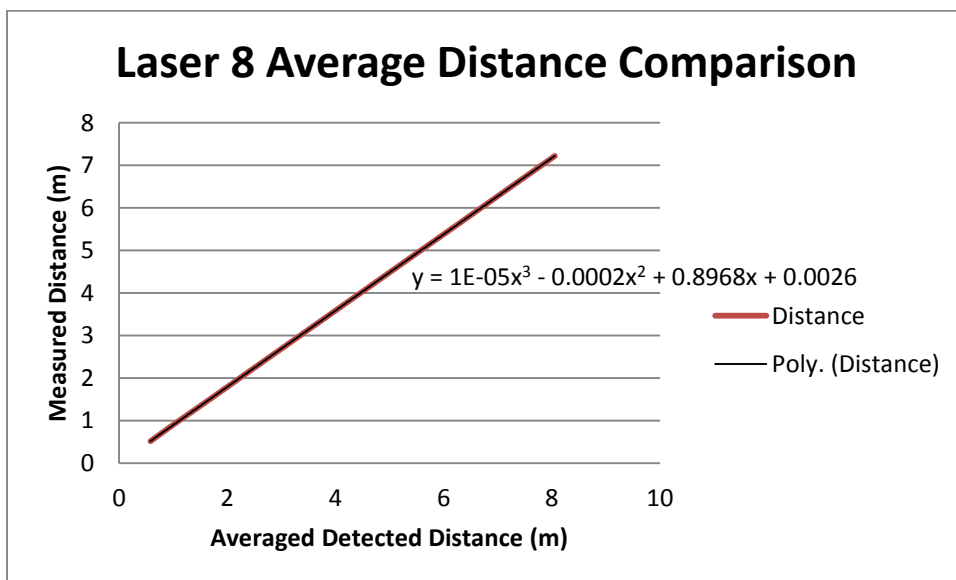
Laser 6:



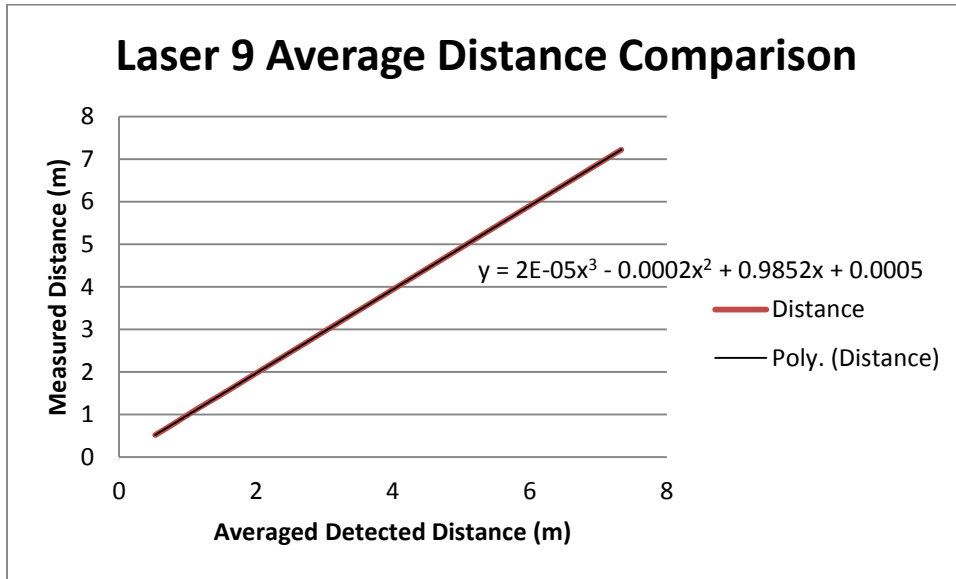
Laser 7:



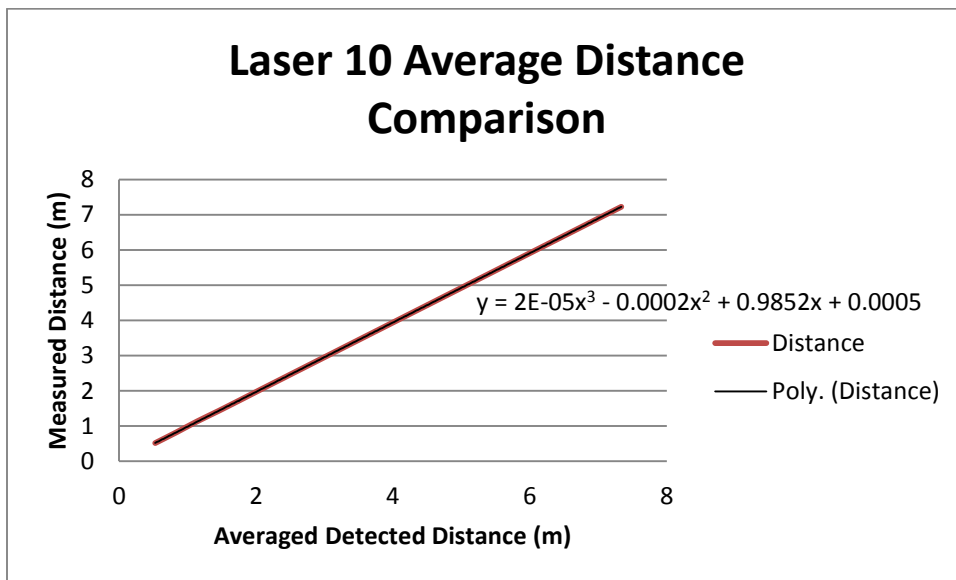
Laser 8:



Laser 9:

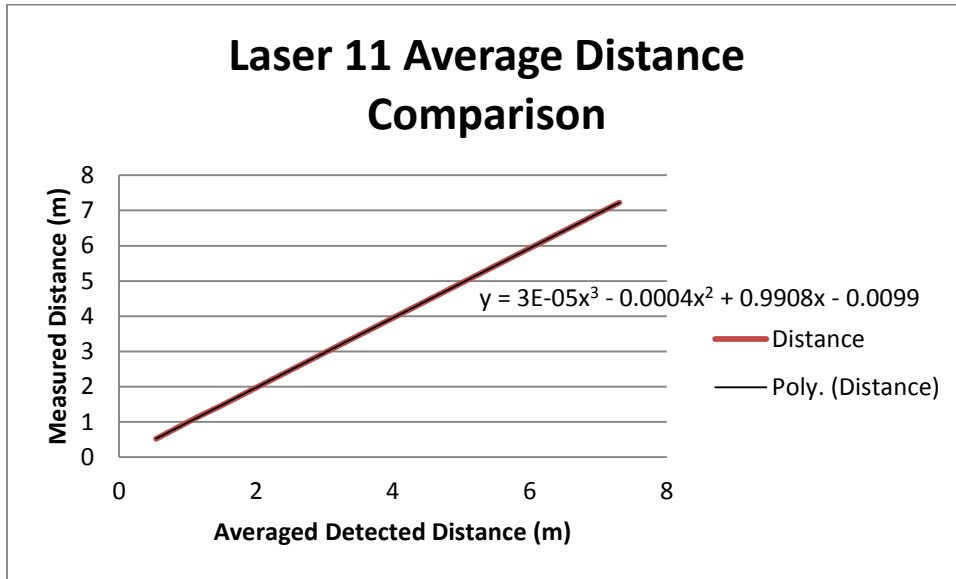


Laser 10:

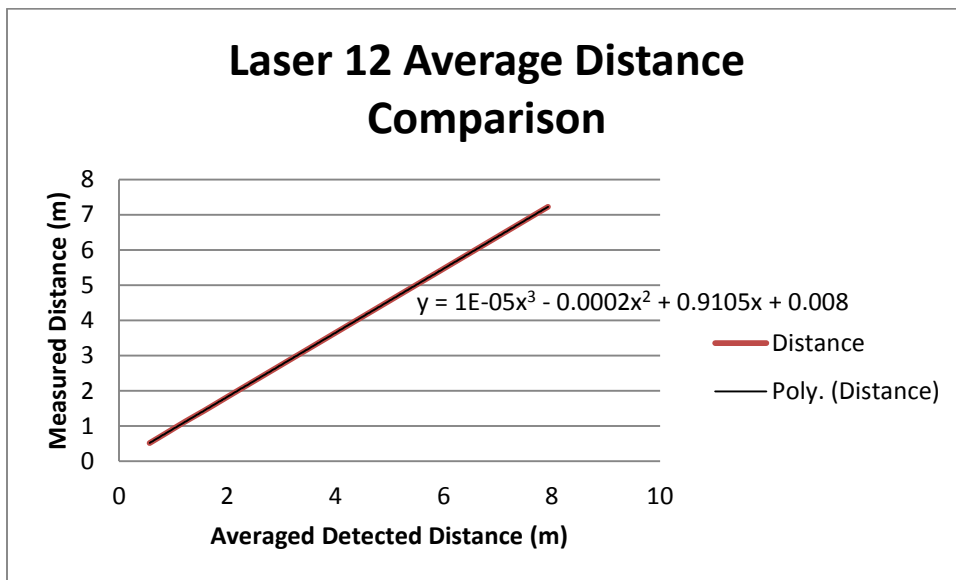




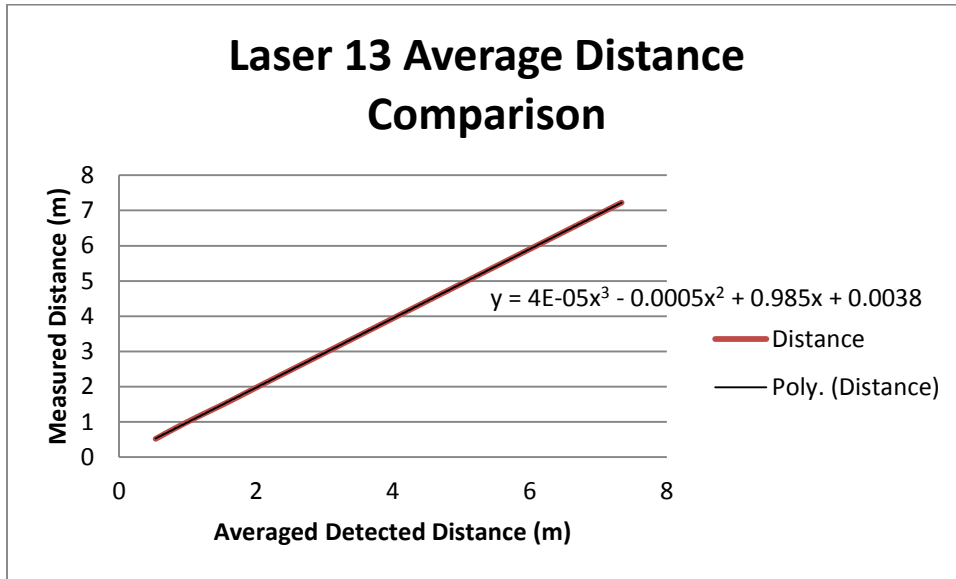
Laser 11:



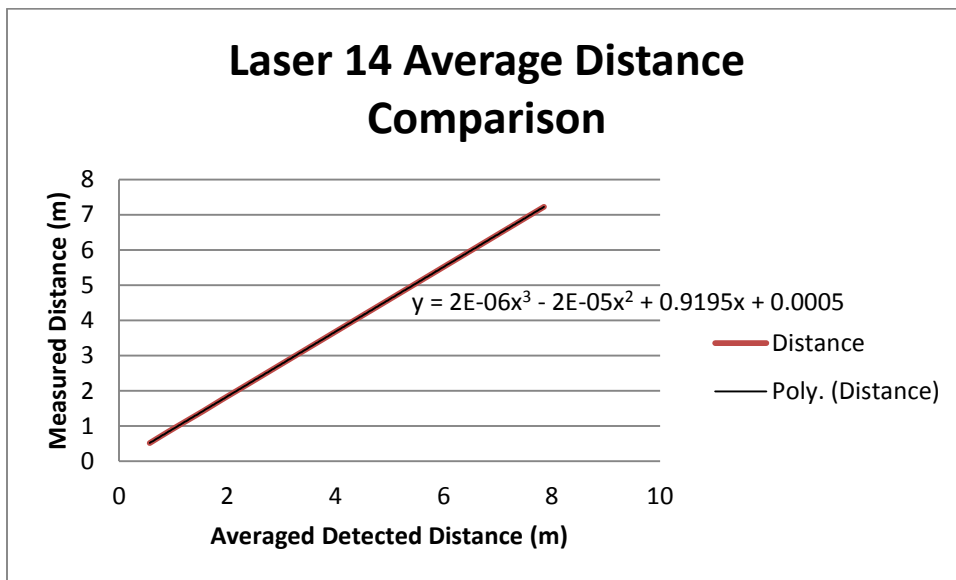
Laser 12:



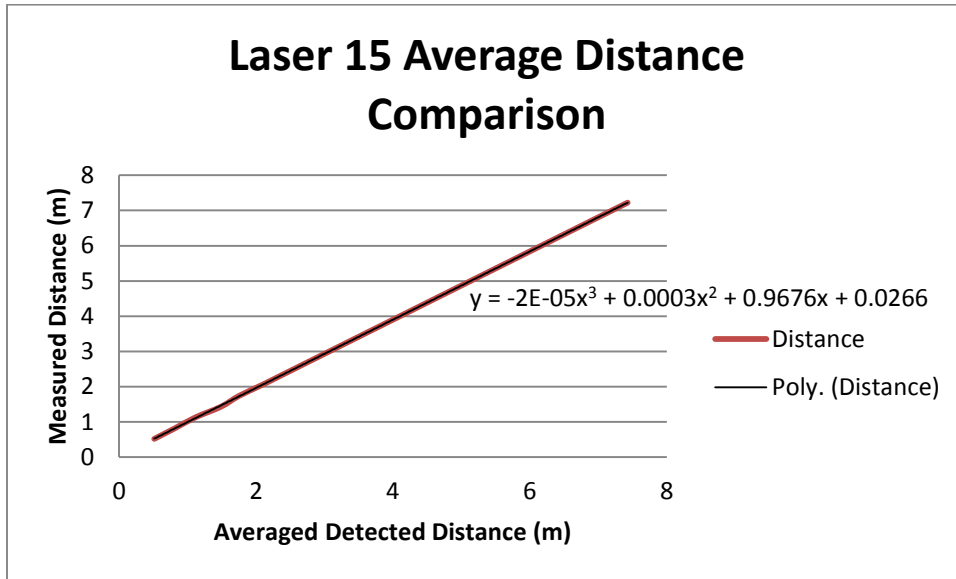
Laser 13:



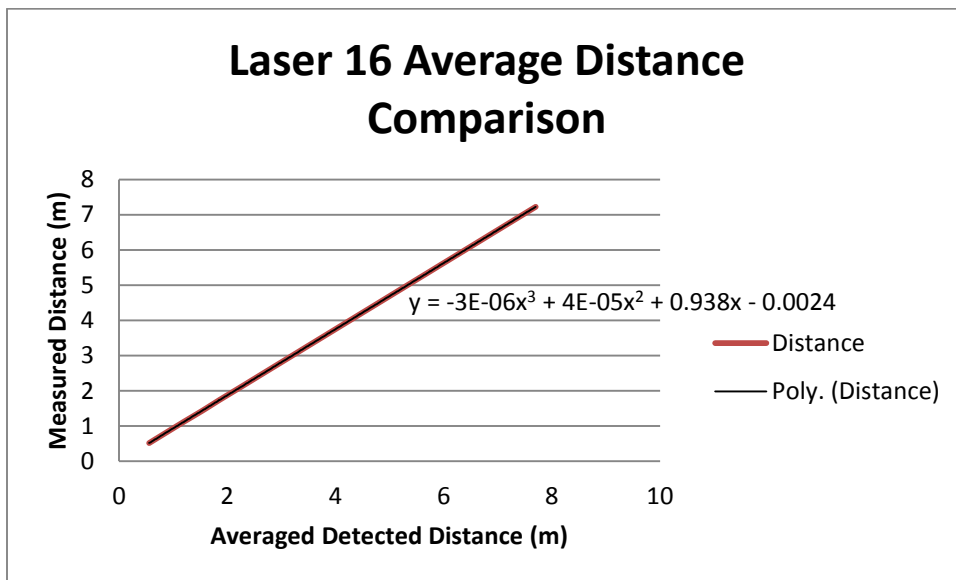
Laser 14:



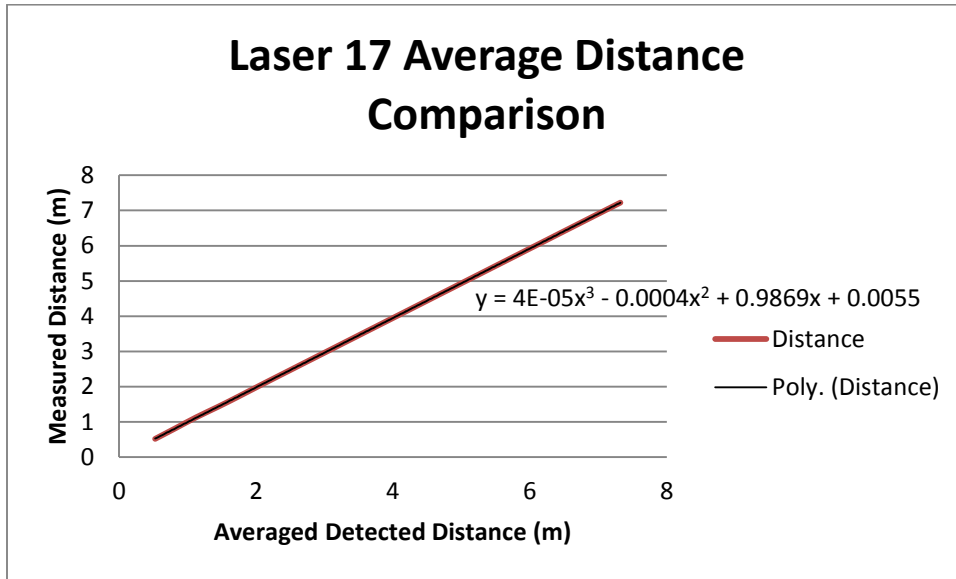
Laser 15:



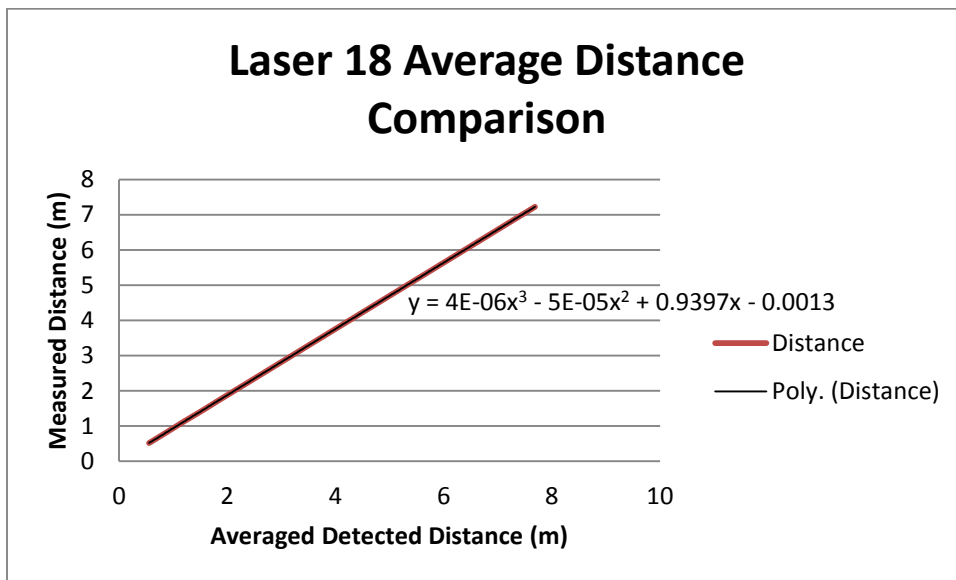
Laser 16:



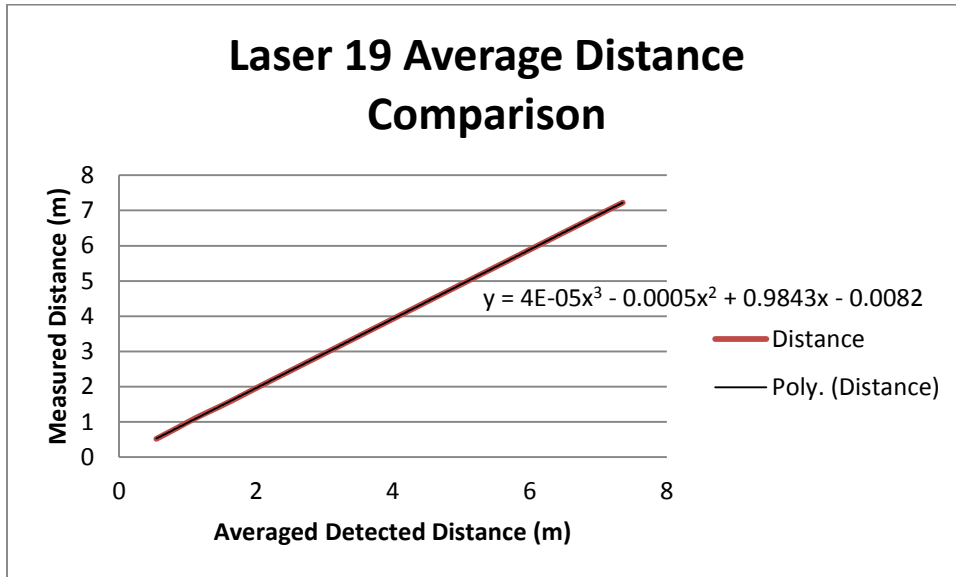
Laser 17:



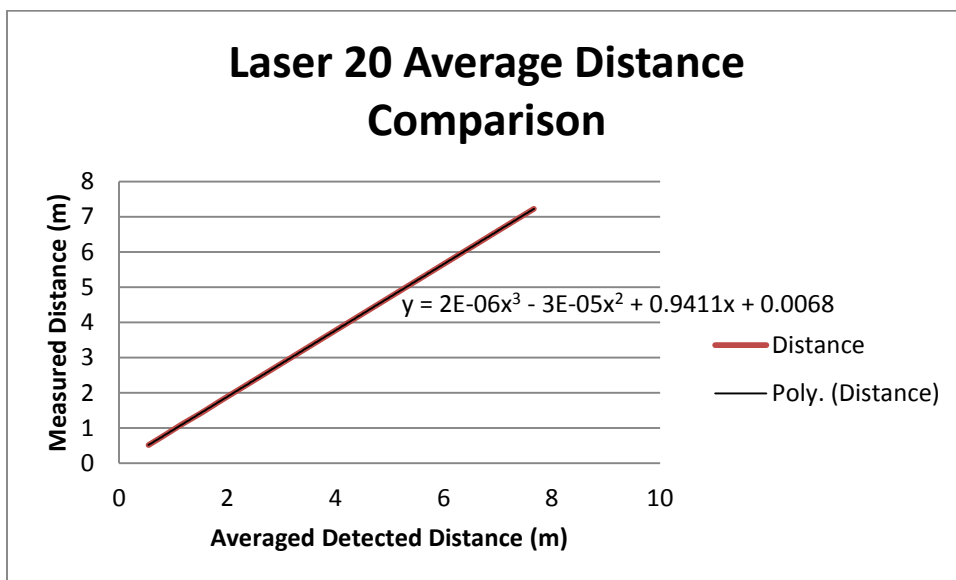
Laser 18:



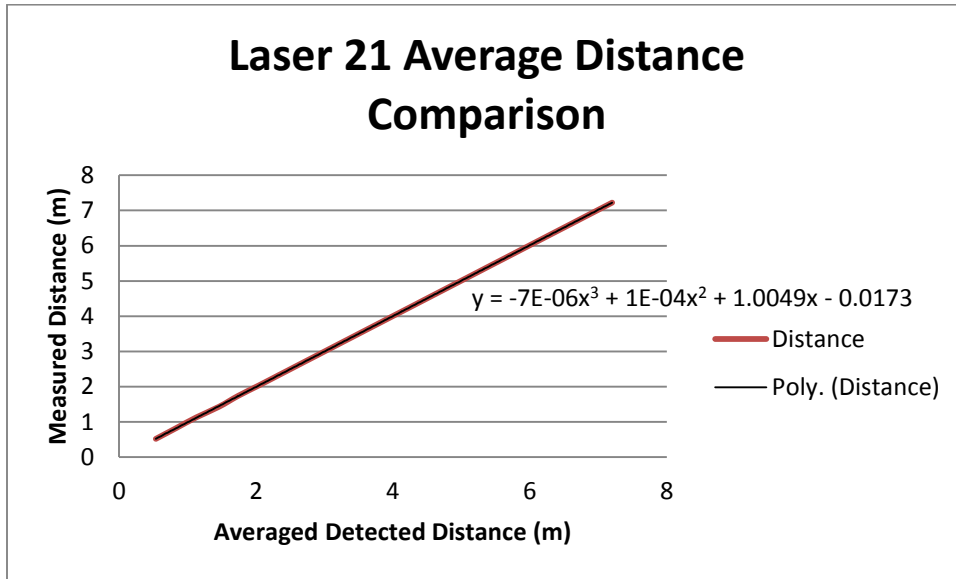
Laser 19:



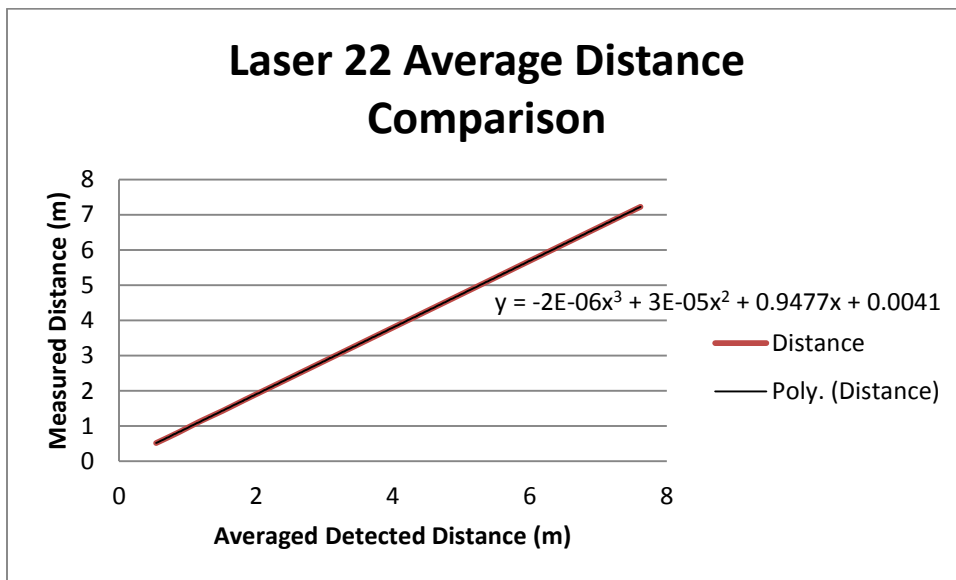
Laser 20:



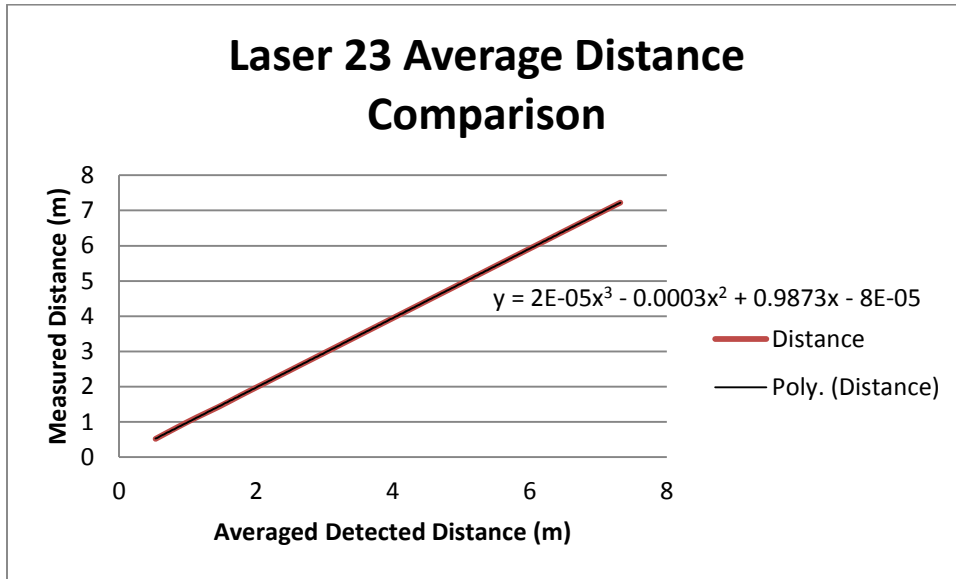
Laser 21:



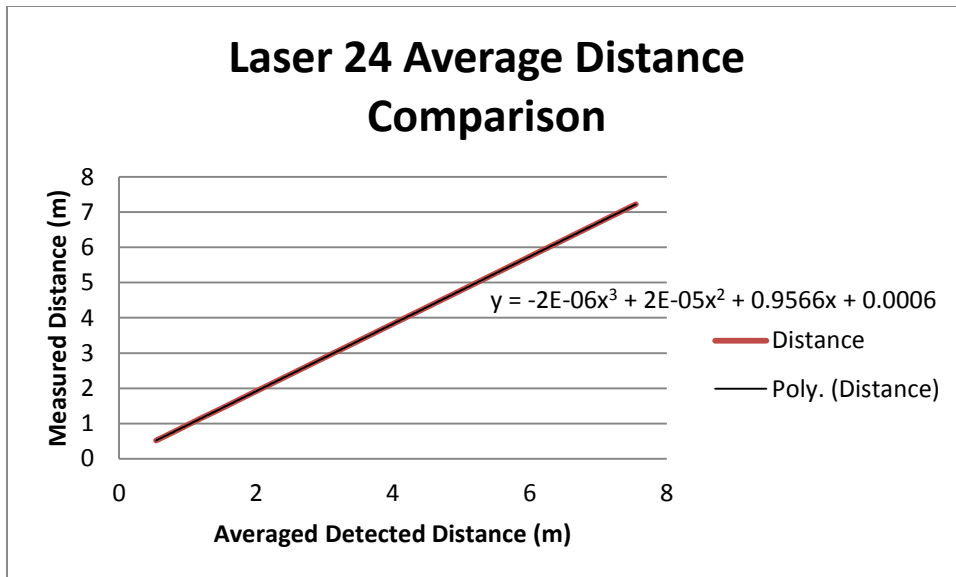
Laser 22:



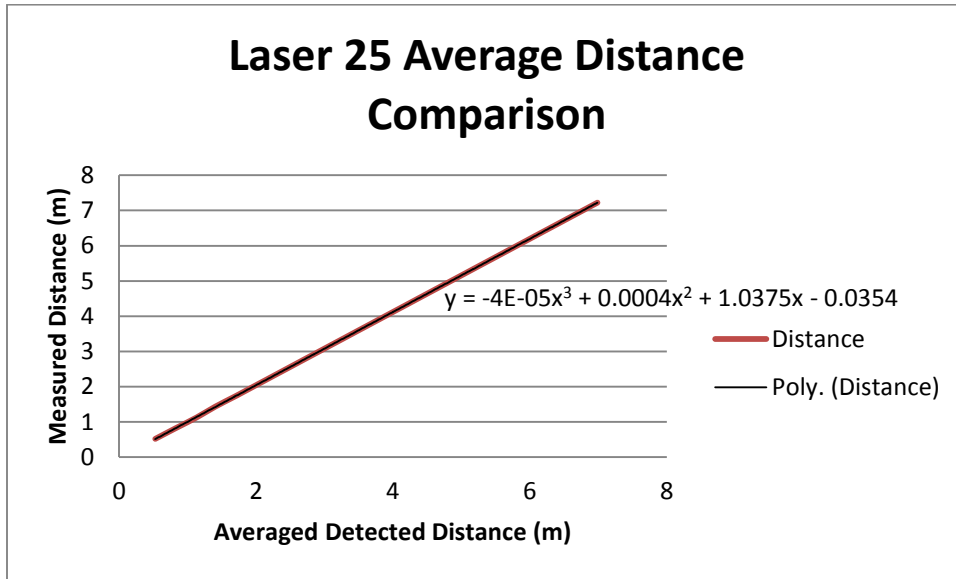
Laser 23:



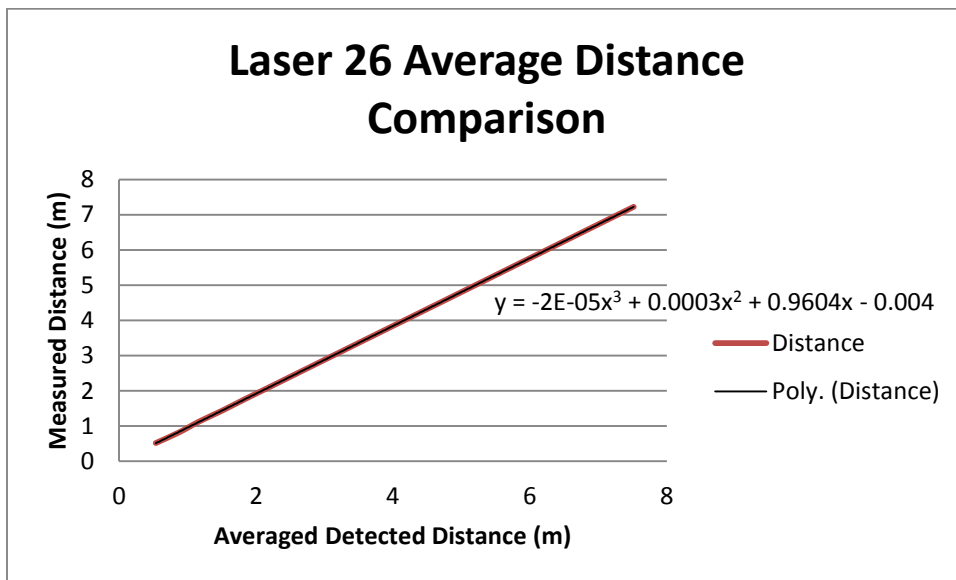
Laser 24:



Laser 25:

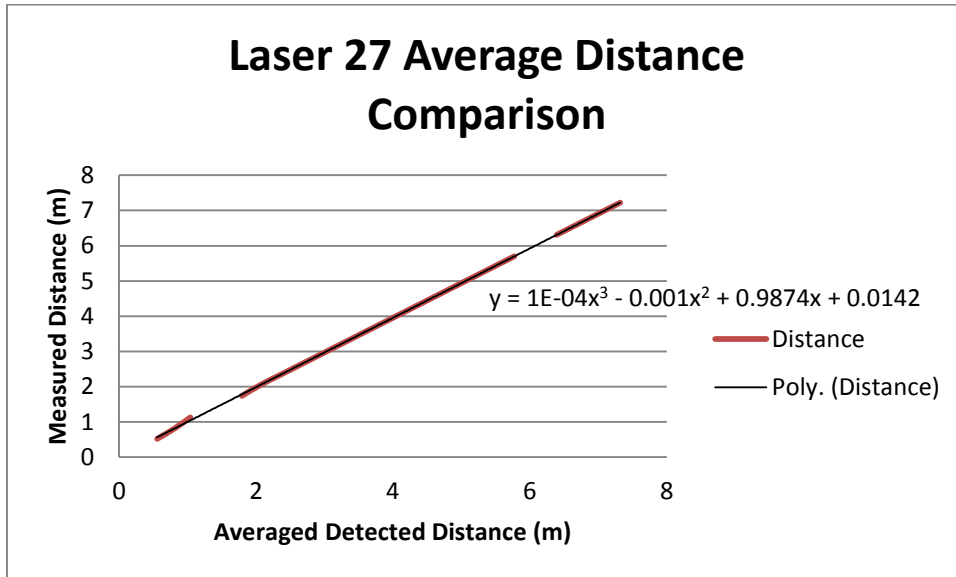


Laser 26:

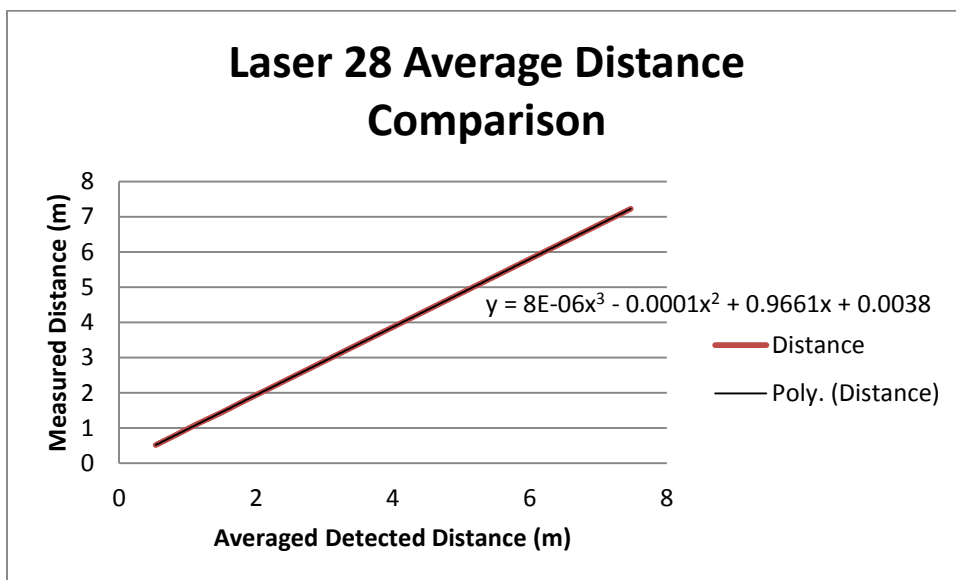




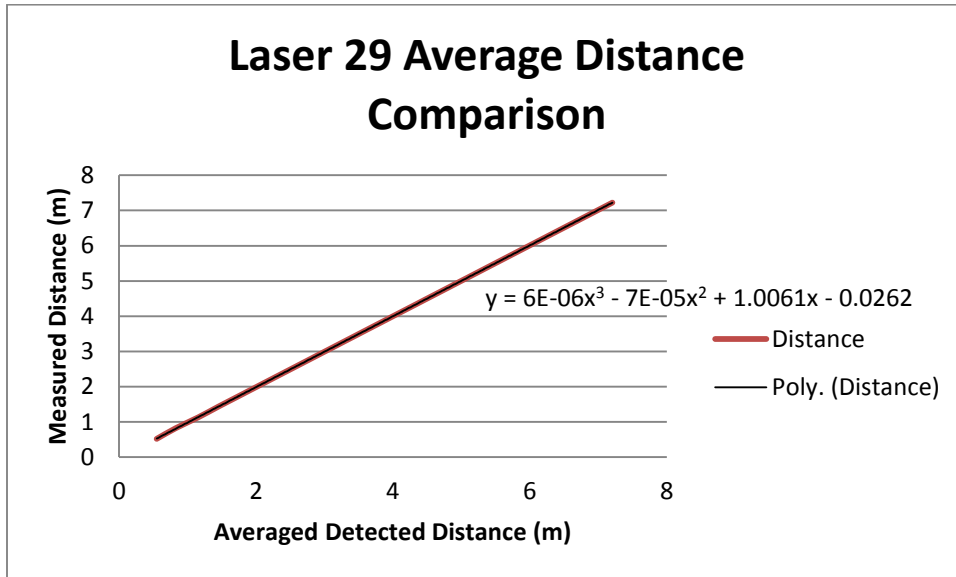
Laser 27:



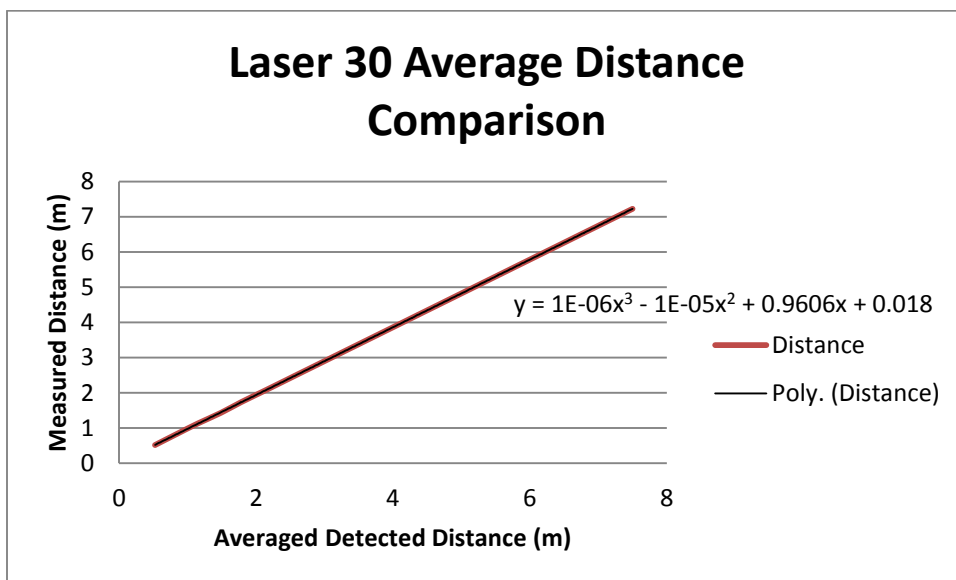
Laser 28:



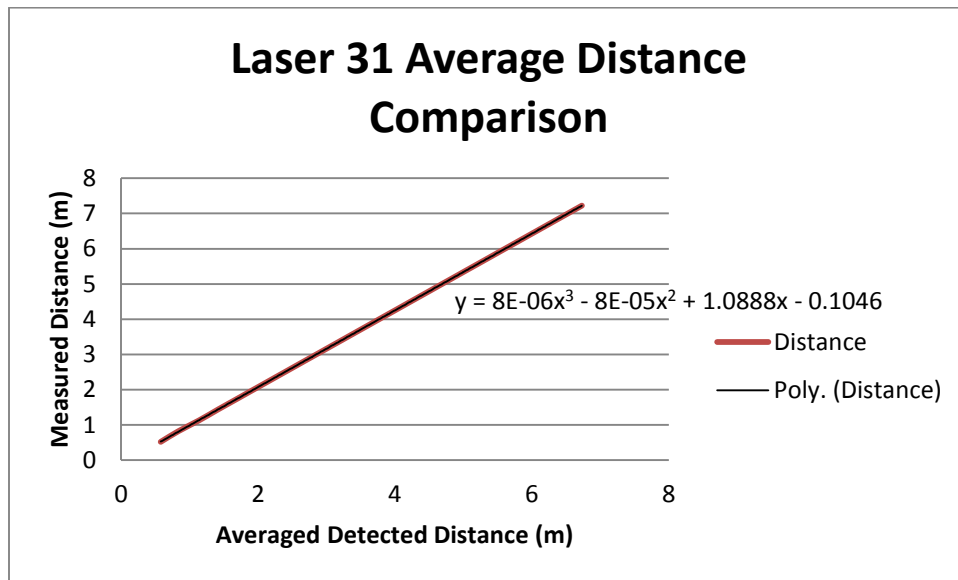
Laser 29:



Laser 30:



Laser 31:



## Anemometer

### Background

#### Anemometer Overview

Anemometers measure deterministic and stochastic characteristics of the wind speed vector at one point. An advantage for sonic anemometers is the absence of moving parts to be in dynamic equilibrium with flow. In Figure 78, two sonic path options are presented. The first consists of two pairs of receivers and transmitters and the second path has a single pair of sensors that both transmit and receive sonic signals. This removes the cup anemometer issue with over-speeding

(over estimation of wind speed in turbulent flow). Sonic anemometers also have a linear response in wide frequency range. They are considered absolute instruments with fixed calibration parameters once constructed.

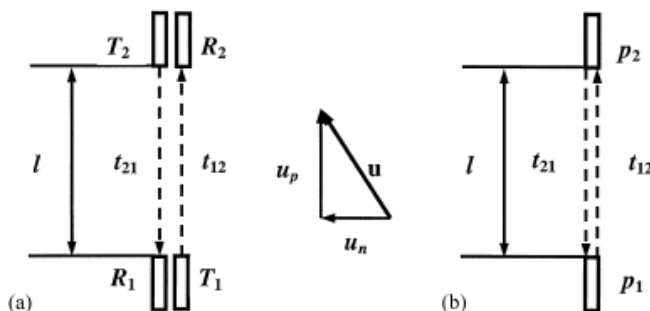


Fig. 1. Schematic of the two different sonic path designs.

Figure 78 "Schematic of two different sonic path designs"

Theoretically, anemometers are relatively independent of flow properties (spatial and time variations, density, temp., etc.). Issues make the sensor difficult to systemize/standardize their usage. The main deficiencies are effect of finite path, path separation, and transducer shadows.

## Sources of Error

Anemometers have sources of error that include measuring air-sea momentum transfer, mean wind speed/velocity, velocity deficit, incident wind direction, vertical wind components, attenuation, spectral density characteristics, and spectral resolution.

Analysis of anemometers in relation to mean wind speed/velocity showed that tilting an anemometer decreases mean wind speed recution influenced by anemometers geometry. Geometry of the sonic anemometer can increase the mean wind velocity because the head and probe supports create certain areas of flow convergence. Calibration testing of sonic anemometers determined mean wind speeds reduced over a degree range for incident wind angle relative to anemometer's head.

Another error with anemometers is the velocity deficit. Through a series of wind tunnel tests, Kaimal (1979) determined that flow attenuation is significant when the mean flow is in the direction of the measurement path of the transducers and decreased as the mean flow angle increased. This “shadow effect” or velocity deficit is caused by the free stream wind velocity being disrupted along the measurement path length by the first measurement transducer before reaching the second measurement transducer.

Incident wind direction relative to the anemometer also stirs up data errors. Three-component sonic array systems have greater incident wind direction limitations when compared to single component array systems because these systems contain three pairs of probe supports versus one pair for the single arrays. Grelle and Lindroth (1994) quantified the flow distortion caused by the anemometer head of a Solent Research/Gill sonic anemometer by varying wind speed and anemometer orientation in incident wind angle and tilt in a wind tunnel. Data sensitive to the orientation of the anemometer, and the instrument itself caused both attenuation and amplification by as much as 15% for certain angles. Amplification is caused by the formation of a jetlike structure that dominates the blocking effect of the anemometer probe, and the effect of flow distortion on flux measurements is by no means negligible (Grelle and Lindroth 1994). Wieser et al. (2001) found that the degree of flow distortion was dependent on the geometry of the instrument. Anemometers with obtrusive probe supports had a greater decrease in mean wind velocity and greater deviation from the incident wind direction.

Anemometer components could lead to a nonzero mean vertical wind vector, and this nonzero vertical component can significantly influence vertical momentum flux calculations (Dyer 1981). Kraan and Oost (1989) conducted wind tunnel calibration tests and found that 1° of tilt can account for a 7% difference between theoretical and measured time-averaged turbulent fluxes. The tilt causes underestimation of vertical velocity. Systematic wind tunnel tests conducted by van der Molen et al. (2004) found similar results and concluded that large angles of attack lead to an underestimation of the vertical velocity by about 15% at angles of  $\pm 60^\circ$  and this error increases with larger angles of attack. A distorted flow field measured by the sonic anemometer was found by Wyngaard (1981), who discussed the related implications, to cause “cross-talk” between the wind velocity components.

Attenuation for an anemometer is greatest when flow is along the axes of the transducers. The anemometer's attenuation increases with obtrusive head and probe supports and decreases with increasing incident wind angle referenced to the transducer axis.

An anemometer's spectral density characteristics are also important to consider. With relation to anemometers, the directional resolution varies for different wind directions. The spectra measured wind velocity components are compared to discern the spectral resolution.

A final error to consider would be the transducer shadowing effect. Static electrical charge from failure to properly ground the anemometer can build up and discharge through the transducers, leading to erroneous signals or transducer failure.

### Error Correction

For error correction of vertical wind components, the mean vertical wind component  $W$  is assumed to be zero over data collection period. Then the data are usually corrected with an axis rotation.

Error correction for directional resolution for different wind directions requires analyzing collected turbulent mean wind speed data to compare measured wind direction to incident wind direction.

An alternative method is proposed, however, since applying a conventional "tilt correction" to force the mean vertical wind speed to zero was found to only remove about half of the errors from the horizontal and vertical covariances caused by the distorted flow field. If the 4/3 ratio between the spectra of the lateral and longitudinal velocity components in the inertial sub-range is to be used as an indicator of local isotropy, then the anemometer needs to be calibrated to identify wind directions where the wind velocity components are attenuated by the anemometer itself. This entails using a three-component sonic array and a Wind Tunnel Calibration that is not standardized yet.

The angle of attack error comes from imperfect (co)sine response of anemometers. The measured wind differs from true value when instantaneous wind vector is non-horizontal and has angle of attack (Nakai et al. 2006).

In the case of an ultrasonic anemometer, the sources of error are self-sheltering by transducers and flow distortion induced by the anemometer's frame. The angle of attack is directly related/proportional to error. The standard deviation depends on surface roughness, measurement height and atmospheric stability. The angle of attack dependent error is probably equipment-related because of the energy balance closure problem. The error is removed by using nonlinear, angle of attack dependent calibration based on the anemometer's size and shape. Calibration derived by wind tunnel experiment as suggested by van der Molen et al. (2004). Experiments showed normalized vertical velocity against angles of attack considerably deviated from ideal sine response, especially at large attack angles. The measured error was 2% at zero angle, 15% at  $a = \pm 60$  degrees, and 60% at  $a = \pm 90$  degrees.

A normalized horizontal velocity against angles of attack underestimated for positive angles of attack  $\alpha$  (updraughts) and overestimated for negative  $\alpha$  (down-draughts) compared to ideal cosine response in wind direction  $0 \leq \gamma \leq 60$  degrees. The behavior dependent on the wind direction  $\gamma$  was largest at 30 degrees because the wind blows directly onto lower transducer.

Measured (co)sine responses were formatted as functions of the angle of attack  $\alpha$  and wind direction  $\gamma$  by fitting functions.

Van der Molen et al. (2004) proposed a method to calibrate vertical and horizontal wind components that introduced the angle of attack dependent calibration, showing a change in calculated fluxes between -5 and +15%, which is an improvement on the energy balance closure. Issues with Van der Molen et al. (2004)'s method included the inability to derive the 'true' angle of attack  $\alpha$  from the arctangent of observed horizontal wind speed  $U$  (m/s) and vertical wind speed  $w$  (m/s) since both values are subject to own angle of attack error. The 'True' angle of attack can be calculated by corrected horizontal and vertical wind speeds. An iterative procedure was used to remove the issue and calculate corrected wind speeds.

The iterative procedure is optimal with two iterations since the extra accuracy for more than that is smaller than the wind tunnel data's measurement accuracy.

The second issue with the method is that the corrected vertical wind speed  $w_c$  diverges at about  $\alpha = -0.54$  degrees because  $\sin(\alpha) + e_{\sin}$  approaches zero. As a result, the magnitude of  $\alpha$  is calculated to be a large value and the magnitude of the corrected vertical wind speed is overestimated while the magnitude of the corrected horizontal wind speed is underestimated in subsequent iterative calculation. This issue is solved by deriving the 'true' angle of attack  $\alpha$  and applying the method to actual field eddy covariance data for checking.

### *Eddy Covariances*

Eddy covariance, which is also referred to as eddy correlation or eddy flux in literature, is a method of analyzing high-frequency wind and scalar atmospheric data and determining vertical turbulent fluxes and their properties within atmospheric boundary layers. The statistical method is commonly used for meteorology, oceanography, global climate models, and agricultural sciences to determine exchange rates of trace gases over ecosystems and quantify gas emissions rates from land and water masses. The technique can be used to estimate energy balance, momentum, heat, water vapor, carbon dioxide, and methane fluxes. Anemometers are common instruments used to measure wind velocity and temperature variation data in correlation (Eddy 2014).

An eddy is a turbulent vortex of variable size with a horizontal component and a vertical component. Air flow is represented as a horizontal flow of a chaotic group of rotating eddies.



Figure 79 Wind flow with Rotating Eddies Measured by Anemometer

The vertical component of an eddy can be measured using an anemometer and the eddy covariance method.

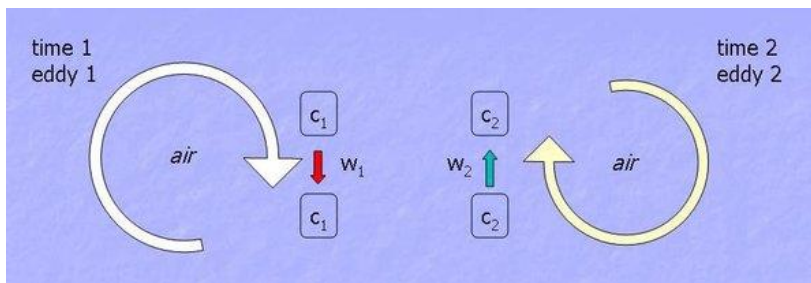


Figure 80 Diagram of the Eddy Covariance Method, with movement for parcel of air ( $c$ ) and associated speed ( $w$ )

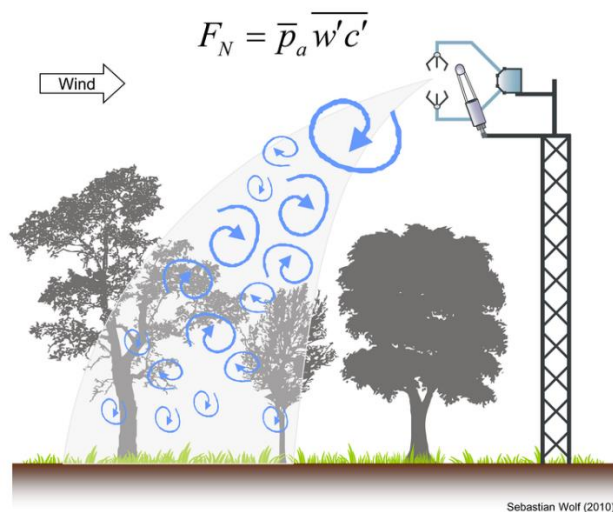


Figure 81 Eddy Flux Equation Application

(Burba 2013)

The correction methodology operates as follows (Nakai et al. 2006):

- Determine the nonlinear equation from fitted function  $f_{sr}(a)$  and  $f_{cr}(a,g)$
- Input 3-D wind components  $u,v,w$  and calculated horizontal wind speed using
$$U = \sqrt{(u^2 + v^2)}$$
- and wind direction  $\gamma$  from  $u$  and  $v$
- Solve the determined nonlinear equations using Steffensen method
- Derive ‘true’ angle of attack  $\alpha$
- Calculate corrected  $u$  and corrected  $v$ , and substitute for  $u$  and  $v$  in  $U$  equation
- Calculate corrected  $w$  where:
$$U_c = \sqrt{(u_c^2 + v_c^2)}$$
  - Apply the process to each individual raw measurement of  $u,v$ , and  $w$  before any other eddy flux calculations or corrections
    - To avoid discontinuity at  $\alpha=0$  degrees and  $f_{sr}(a)$  not fitting at angles of attack greater than 80 degrees when using the sine response function:
- Assume effect is independent of wind speed
- Average the more accurate higher wind speed conditions
- Use logistic regression
- $f_{sr}(a)=L(a)\sin(a)+a_{sr}(0)$ 
  - where  $L(a)$  is the logistic regression (step) function estimated by using Marquardt’s method (Conway et al, 1970)
  - $L(\alpha) = \frac{p_1}{1+p_2 \exp(-p_3(\alpha+90))} + p_4$
  - $(-90 \leq \alpha < 0)$
  - $L(\alpha) = -\frac{p_1}{1+p_2 \exp(-p_3\alpha)} + p_4$
  - $(0 \leq \alpha < 90)$
  - The function  $L(a)$  has a discontinuity at  $a=0$  degrees, but is continuous since  $\sin(a)=0$  at  $a=0$  degrees.

The van der Morlen et al. (2004) cosine response observed was regarded as the phase shifted cosine function. The corrected cosine response function proposed was:

$$f_{cr}(\alpha, \gamma) = \cos(f(\alpha, \gamma))$$

Where  $f(\alpha, \gamma)$ (degree) is the polynomial of  $\alpha$ :

$$f(\alpha, \gamma) = q_1\alpha^3 + q_2\alpha^2 + q_3\alpha + \delta(\gamma)$$

Where  $\delta(\gamma)$  is wind direction dependent offset function of  $\gamma$ . The coefficients were obtained by linear least square regression of  $f(\alpha, \gamma)$  versus arccosine of the actual cosine responses for a set



range. The phase shift of  $f_{cr}(\alpha, \gamma)$  is represented by offset function  $\delta(\gamma)$ . Since the phase shift from wind tunnel data potentially results from underestimation of  $a_{cr}(\alpha, \gamma)$  at positive angles of attack  $\alpha$  explained by transducer shadowing effect, the transducer's vertical position cannot be neglected. The paper proposed an alternative function  $\delta(\gamma)$ :

$$\delta(\gamma) = r \sin(3\gamma)$$

Where the constant  $r$  is obtained by least square regression (Cuerva 2000).

Based on R3-50's "certificate of calibration" in the manual, the strut frame has small effect on the horizontal wind speed. The result agrees with van der Molen et al. (2004)'s result from deriving the cosine response data via calibration of an R2 instrument. The effect of the frame on the cosine response function should be negligible if assuming the frame is almost homogenous along the vertical axis and does not affect the relationship between the horizontal wind component and the angle of attack  $\alpha$ . This conclusion derives from the manufacturer's on-line calibration correcting for horizontal wind speed, but neglects to account for angle of attack errors.

The second issue is the cubic function describing the distortion of the cosine response function is common for the angle of attack range from 0 to 60 degrees. The third issue is the phase shift effect resulting from underestimating the  $a_{cr}$  at positive angles of attack in instances of the wind attacking the lower transducer.

A developed nonlinear equation relating  $\alpha$  to  $\alpha'$  derived with equation substitution, resulted in (Nakai et al. 2006):

$$L(\alpha) \sin(\alpha) + a_{sr}(0) - \tan(\alpha') \cos(f(\alpha, \gamma)) = 0$$

The equation must be solved uniquely followed by estimating  $\alpha$  from  $\alpha'$  (or  $U, W$ ) analytically. Steffensen's method is used, with  $\alpha = g(\alpha')$

Rearrange as (Nakai et al. 2006):

$$\alpha = \arctan\left(\frac{(\tan(\alpha') \cos(f(\alpha, \gamma)) - a_{sr}(0))}{L(\alpha) \cos(\alpha)}\right)$$

The threshold limit of  $\varepsilon = 0.01^\circ$  is used.

In addressing the eddy covariance, the effect of (co)sine error correction on actual eddy fluxes of sensible heat ( $H$ ), latent heat ( $\lambda E$ ) and  $CO_2(F_C)$ , and on energy balance closure must be analyzed. This analysis requires using linear time averaging and a five step procedure to calculate eddy fluxes. The procedure consists of:

- 1) humidity correction of sonic temperature (Schotanus et al., 1983)
- 2) correction of angle of attack dependent error

- 3) coordinate rotation for  $\bar{v}$  equals 0 and  $\bar{w}$  equals 0 (McMillen, 1988, Kaimal and Finnigan, 1994);
- 4) frequency response corrections (Moore, 1986)
- 5) WPL correction (Webb et al., 1980)

For crosswind correction of sonic temperature (Schotanus et al., 1983; Kaimal and Gaynor, 1991), filter  $\lambda E$  and  $F_C$  using standard deviation of water vapor concentration  $q$  ( $\text{kg m}^{-3}$ ),  $\sigma_q$ , and  $\text{CO}_2$  concentration ( $\text{kg m}^{-3}$ ),  $\sigma_c$ . Linear regression through the origin can be used to find the effect of correcting the eddy fluxes because of the linear relationships between uncorrected and corrected fluxes. The increase increments for fluxes were found to be smaller for the method proposed in van der Molen et al. (2004) than in Nakai et al. (2006)'s method by about 2-3% depending on the area of collected data. Van der Molen et al. (2004)'s method slightly underestimates  $\alpha$  because of incomplete conversion, which could also result in underestimation of eddy flux corrections. Overall Nakai et al. (2006)'s method provides higher accuracy with less computational time, removal of large angles of attack deviations, and removal of the wrong conversion of  $\alpha$  near  $\alpha=0.64$  degrees. The method additionally considers transducers' vertical position effect on cosine response. The far more rigorous trait of Nakai et al. (2006)'s method owes to deriving the "true" angle of attack by solving the nonlinear equation with relation to observed  $U$  and  $w$  via the Steffensen method, which is robust and fast for practical eddy flux calculations.

## Current Meter

Valeport Model 803

#### FLOW, PITCH & ROLL CONVENTION

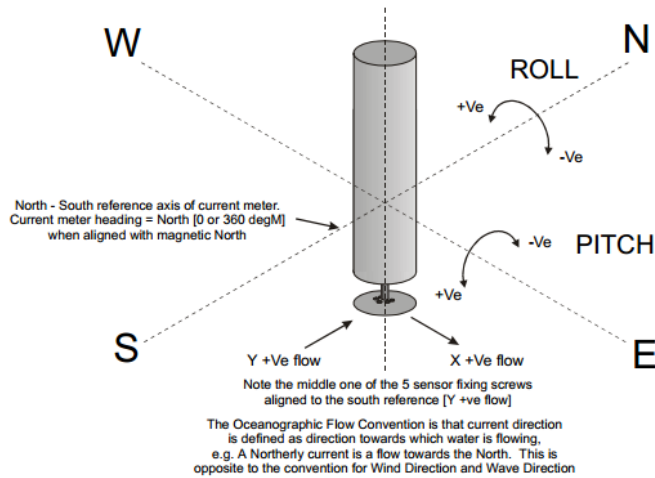


Figure 82 Flow, Pitch, and Roll Convention for a Current Meter

### Acoustic Vs. Electromagnetic Current Meter

Current meters measure current through a volume of water based on physical occurrence called electromagnetic induction. Electrically charged particles moving through a magnetic field generate an electric field perpendicular to the flow. In seawater, ions move with the currents perpendicular to Earth's magnetic field. Maxwell's third equation, known as Faraday's law of induction, states that measuring an induced electrical current enables determining the variability in the averaged horizontal flow. The vertical components of the electric field "short out" because sea water is conductive. A minor vertical weighting effect is, however, applied because conductivity changes are depth dependent (Meinen 2013).

### Sources of Error

Current meters are heavily dependent on the fluid dynamics through which they move. Sources of error can include surface-wave contamination, wave motion, wakes, transients, water entrainment, turbulence, broad-band excitation, and response length scales. The flows from surface-wave contamination, for example, make moored observations difficult.

### Error Model

A basic technique for modeling current meters is a method called direct moored inter-comparisons (Halpern et al. (1981), Beardsley et al. (1977)). Inter-comparison results, however, are limited by excitation range provided in situ, the inability to control the environment, and unavailable "standards" for comparisons.

Another model uses vertical planar motion mechanism (VPMM) to simulate wave induced dynamic motions that current meters experience. The generated model only allows study of a single constant frequency. In nature, however, a time dependent broad-band wave motion exists. (Woodward and Appell (1978))

A numeric model was used to predict mean flow response of current meters in large wave-like conditions (McCullough (1978), McCullough and Graeper (1979)). Comparison with test results using an early NBIS-ACM-1 model concluded more inclusive tests were needed to determine the model's usefulness.

The study, "Laboratory Verification of an Acoustic Current Meter Error Model (Mero et al. 1982) uses the NBIS-ACM-2, which is a "solid-state" acoustic travel time current meter, to study the numerical model proposed. The numeric model simulates the current meter's response in large wave conditions by implementing horizontal and vertical cosine response functions from stead-flow test data. There are 2 horizontal response functions, termed  $HCR_x$  and  $HCR_y$ , with each respective function representing an axis of the current meter along the measurement plane. The horizontal cosine response function is the ratio of the measured velocity to the actual velocity as a function of angle A of the flow relative to the measurement axis. For an ideal current meter, the horizontal cosine response functions are unity but this is difficult to obtain since the current meters cause flow distortions. The vertical cosine response function, which measures the current meter's ability to handle "tilted" flows at angle B out of measurement plane, is the ratio of the angles A and B and flow speed ( $V_f$ ) to the output of the current meter with no tilt ( $B=0$ ).

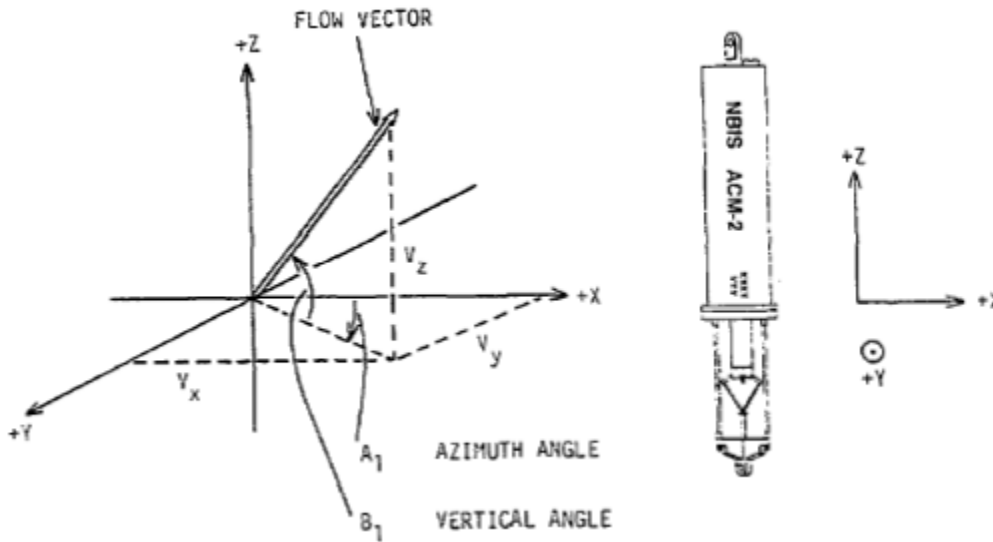


Figure 83 Diagram of Current Meter's Coordinate System based on the Horizontal and Vertical Cosine Response Functions and the corresponding angles A and B.

The output of the current meter with respect to the horizontal and vertical cosine response functions is:

$$V_{xm} = V_f \cos A \times HCR_x(A) \times VCR(B, A, V_f)$$

$$V_{ym} = V_f \cos A \times HCR_y(A) \times VCR(B, A, V_f)$$

These expressions form the basis of the numeric model, which assumes:

- 1) The steady-flow horizontal and vertical cosine response functions for the current meter represent in wave forms
- 2) The flow is composed of only steady mean flow and a single-frequency fixed-amplitude planar vertical circular-orbital flow
- 3) Time and space dependent flow effects are negligible (i.e. wake, transients, water entrainment, turbulence, broad-band excitation, response length scales, etc. not modeled)

Assumption 1) is inadequate for oscillations the size of or smaller than the current meter, but becomes more realistic for wave particle trajectories greater than the sensor. While closely modeling laboratory tests, assumption 2) inadequately represents typical broad-band ocean surface gravity wave flow, though it may apply for some types of mooring motion (i.e. at mid-depths). The final, dependent, assumption accounts for other significant effects not accounted for in the first model.

It should also be noted that the model is purely kinematic, meaning it calculates the geometric flow sums and does not treat effects that may not be negligible, such as length scales, secondary flows, broad-band forcing, etc. The results are first order engineering error estimates anticipated for current sensors with imperfect horizontal and vertical cosine response waves larger than the sensor.

In testing, the “signal-to-noise ratio” (SNR) was examined as the ratio of the mean current to the mean orbital velocity.

The study “Methods of Evaluating Uncertainty for Current Meters” (Hersch 2002), assesses two methods referred to as Type A and Type B. Combined uncertainty is represented by  $u$

- $u_{pi}$ - uncertainty in mean velocity  $v_i$  because of limited number of depths at which velocity measurements are made at vertical  $i$ 
  - For reference,  $n_i$  is the number of depths in the vertical at which velocity measurements are made
- $u_{ci}$ - uncertainty in point velocity at a particular depth in vertical  $i$  due to variable responsiveness of the current meter
- $u_{ei}$ - uncertainty in point velocity at a particular depth in vertical  $i$  due to velocity fluctuations (pulsations) in the stream

Analysis of uncertainties for flow measurement cites the International Standards Organization’s *Guide to the Expression of Uncertainty in Measurement*. The Guide as of 2002 states there is no inherent difference between uncertainties arising from a random effect versus an uncertainty component arising from a systematic effect correction. The components of uncertainty use standard deviation estimates termed “standard uncertainty”. The standard uncertainty, represented by  $u_i$  is equal to the positive square root of the estimated variance  $u_i^2$ . The resultant uncertainty is a combination of all uncertainty components and referred to as combined uncertainty.

- Type A evaluation of uncertainty consists of statistical analysis of replicate observations to obtain statistical estimates of the observations' standard deviation.
- Type B uncertainty evaluation calculates the standard deviation of an assumed probability distribution based on scientific judgment and inclusion of all information, which includes previous measurement and calibration data, experience, and general knowledge of the behavior and properties of relevant instruments.

By analyzing the system, it can be determined whether Type A or Type B method is appropriate for evaluating random or systematic uncertainty components.

Flow uncertainties are expressed as percentage standard uncertainties correlated with percentage coefficients of variation, which is the standard deviation divided by the mean. These defined expanded uncertainties are taken with a coverage factor 2 with an approximately 95% confidence level, meaning 95% of the observations on average are within the specified limits of two standard deviations from the mean. No uncertainty value, however, is ascribed to the 5% remainder.

A procedure for calculating current meter flow measurement uncertainty goes as follows. The method divides the channel cross-section into segments by  $m$  verticals. Then it measures the breadth, depth, and mean velocity, referred to as  $b_i$ ,  $d_i$ ,  $v_i$ , respectively. Point velocity measurements made at each of several depths on the vertical are used to calculate the mean velocity  $v_i$  at each vertical and the flow equation produced is:

$$Q = F \sum b_i d_i v_i$$

Where  $Q$  is the flow ( $m^3s^{-1}$ ) and  $F$  is an assumed factor at unity relating the discrete sum over the finite number of verticals to the integral of the continuous function over the observed cross-section. The flow equation must be optimized until sufficient verticals are used to make  $F$  unity, or else  $F$  may be greater than unity since discharges resulting from river sections with too few verticals are generally too low.

The relative combined standard uncertainty in the measurement as percentage can be defined as (Hersch 2002):

$$u(Q)^2 = u_m^2 + u_s^2 + \frac{\sum ((b_i d_i v_i)^2 (u_{b_i}^2 + u_{d_i}^2 + u_{v_i}^2))}{(\sum b_i d_i v_i)^2}$$

Where  $u(Q)$  is the percentage combined standard uncertainty in discharge,  $u_{b_i}$ ,  $u_{d_i}$ , and  $u_{v_i}$  are the relative percentage standard uncertainties as previously defined measured at vertical  $i$ ,  $m$  is the number of verticals, and  $u_m$  is the uncertainty from the limited number of verticals.

The value  $u_s$  is the uncertainty from calibration errors in current meter, breadth measurement instrument, and depth sounding instrument. The equation is defined by:

$$u_S = (u_{cm}^2 + u_{bm}^2 + u_{ds}^2)^{1/2}$$

A practical value for this expression can be estimated as 1%.

$$\text{Using } u(v_i)^2 = u_{pi}^2 + (1/n_i)(u_{ci}^2 + u_{ei}^2)$$

The combined equation becomes (Herschy 2002):

$$u(Q)^2 = u_m^2 + u_s^2 + \frac{\sum \left( (b_i d_i v_i)^2 (u_{bi}^2 + u_{di}^2 + u_{pi}^2 + (1/n_i)(u_{ci}^2 + u_{ei}^2)) \right)}{(\sum b_i d_i v_i)^2}$$

The equation can be simplified if the measurement verticals are placed to approximately equalize the segment discharges and the component uncertainties are equal (Herschy 2002):

$$u(Q) = \left[ u_m^2 + u_s^2 + \left( \frac{1}{m} \right) \left( u_b^2 + u_d^2 + u_p^2 + \left( \frac{1}{n} \right) (u_c^2 + u_e^2) \right) \right]^{1/2}$$

### Reasoning for Not Using Current Meter

Singapore's Marina Bay contains fresh water as a result of the Marina Barrage built in 2008 to create a freshwater reservoir limiting marine transportation access and regulating water quality (Moh 2009). Without the presence of charged particles moving with the current in the water, the current meter cannot operate on a marine vehicle and provide useful data.